



HAL
open science

Random vibration fatigue analysis with the use of isogeometric analysis method

Shubiao Wang

► **To cite this version:**

Shubiao Wang. Random vibration fatigue analysis with the use of isogeometric analysis method. Vibrations [physics.class-ph]. Normandie Université, 2022. English. NNT : 2022NORMIR04 . tel-03670652

HAL Id: tel-03670652

<https://theses.hal.science/tel-03670652>

Submitted on 17 May 2022

HAL is a multi-disciplinary open access archive for the deposit and dissemination of scientific research documents, whether they are published or not. The documents may come from teaching and research institutions in France or abroad, or from public or private research centers.

L'archive ouverte pluridisciplinaire **HAL**, est destinée au dépôt et à la diffusion de documents scientifiques de niveau recherche, publiés ou non, émanant des établissements d'enseignement et de recherche français ou étrangers, des laboratoires publics ou privés.



Normandie Université

THESE

Pour obtenir le diplôme de doctorat

Spécialité Génie Mécanique

Préparée au sein de l'Institut National des Sciences Appliquées de Rouen Normandie

Random vibration fatigue analysis with the use of isogeometric analysis method

Présentée et soutenue par
Shubiao WANG

Thèse soutenue publiquement le (23 Mars 2022)
devant le jury composé de

| | | |
|---------------------------|---|---------------------|
| M. Nacer HAMZAOU | Professeur, INSA de Lyon, France | Président du jury |
| M. Stéphane PANIER | Professeur, University de Picardie Jules Verne, France | Rapporteur |
| M. Roger SERRA | Maître de conférences HDR, INSA Centre Val de Loire, France | Rapporteur |
| M. Eduardo SOUZA DE CURSI | Professeur, INSA de Rouen Normandie, France | Examineur |
| Mme Leila KHALIJ | Maître de conférences HDR, INSA Rouen Normandie, France | Directrice de thèse |
| Mme Renata TROIAN | Maître de conférences, INSA Rouen Normandie, France | Encadrante |

Thèse dirigée par Mme Leila KHALIJ, Laboratoire de Mécanique de Normandie – LMN (EA 3828)



Abstract

Nowadays, mechanical systems are composed of numerous components, leading to specific requirements for numerical analysis methods in terms of accuracy and time computation. The finite element analysis (FEA) is essential in simulation technology, as it can help engineers predict results to avoid experimental cost testing. However, the conventional FEA has some mesh generation and geometric representation weaknesses. The time spent in the mesh generation process is often much longer than the analysis time. It is mandatory to communicate with the original geometry during each mesh refinement process, which takes time and can lead to complex problems. Furthermore, it is challenging to accurately represent complex geometric models based on the Lagrangian basis function in classical FEA. Thus, the approximate models would result in inaccurate analysis results.

Failures in mechanical structures are mostly due to fatigue. Fatigue life prediction is essential to know the actual life before a part is used in operation. These operating parts experience random fatigue loads and the most appropriate approach is to use a probabilistic method to develop the fatigue analysis. This analysis can be performed in the time or frequency domain for Gaussian random processes. However, the time domain analysis is time consuming compared to using power spectral density (PSD) in the frequency domain.

Thus, this study considered the random vibration fatigue analysis in the frequency domain using the isogeometric analysis (IGA) method. Geometric models can be described by non-uniform rational B-spline curves (NURBS), and the corresponding mesh generation and refinement processes are extremely fast compared to FEA.

The main content of the thesis is divided into four parts. In the first part, the IGA was developed on a simple plate model to be compared with FEA based on the analytical solution. In the second part, fatigue analyses by Dirlik method were performed on a plate model. FEA was used to check the results and experimental tests were used to give a relative conclusion on the methods. An L-shaped plate and a wind turbine tower model were also studied in random fatigue in the third part. The results obtained in terms of damage were validated by FEA and a Matlab program that we developed. In the fourth part, isogeometric optimization was developed on the tower model by combining Matlab programming and LS DYNA.

In conclusion, the IGA is suitable for numerical simulations of mechanical structures since the results obtained highlight:

- IGA is efficient in terms of mesh generation compared to FEA.
- IGA can provide similar results to FEA with an acceptable relative error given that for damage calculation, IGA requires fewer integration points and mesh elements.
- Optimization with design variables as control points can provide consistent models.

Keywords Isogeometric analysis; Finite element method; Random vibration; Numerical and experimental tests

Résumé

De nos jours, les systèmes mécaniques sont composés de nombreux éléments, ce qui entraîne des exigences spécifiques pour les méthodes d'analyse numérique en termes de précision et de temps de calcul. La méthode d'analyse par éléments finis (MEF) est essentielle dans la technologie de simulation, car elle peut aider les ingénieurs à prévoir les résultats afin d'éviter les essais expérimentaux coûteux. Cependant, la MEF classique présente certaines faiblesses en matière de génération de maillage et de représentation géométrique. Le temps consacré au processus de génération de maillage est souvent beaucoup plus long que le temps d'analyse. Il est nécessaire de communiquer avec la géométrie d'origine pendant chaque processus de raffinement du maillage, ce qui prend du temps et peut rendre le problème complexe. En outre, il est difficile de représenter avec précision des modèles géométriques complexes basés sur la fonction de base Lagrangienne dans la MEF classique. Ainsi, des modèles approximatifs donnent des résultats d'analyse inexacts.

Les défaillances des structures mécaniques sont principalement dues à la fatigue. La prédiction de la durée de vie en fatigue est essentielle pour connaître la durée de vie effective avant qu'une pièce ne soit utilisée en fonctionnement. Ces pièces subissent des charges de fatigue aléatoires, et l'approche la plus appropriée est d'utiliser une méthode probabiliste pour développer l'analyse de fatigue. L'analyse de la fatigue peut être effectuée dans le domaine temporel ou fréquentiel pour les processus aléatoires Gaussiens. Cependant, l'analyse dans le domaine temporel prend beaucoup de temps par rapport à l'utilisation de la densité spectrale de puissance (DSP) dans le domaine fréquentiel.

Ainsi, cette étude est basée sur l'analyse de la fatigue par vibration aléatoire dans le domaine fréquentiel en utilisant la méthode d'analyse isogéométrique (IGA). Les modèles géométriques peuvent être décrits par des courbes B-spline rationnelles non uniformes (NURBS) et les processus de génération et de raffinement du maillage correspondant sont extrêmement rapides par rapport à la MEF.

Le contenu principal de la thèse est divisé en quatre parties. Dans la première, l'IGA a été développée sur un modèle de plaque simple afin d'être comparée aux résultats de la MEF en se basant sur la solution analytique. Dans la deuxième partie, des analyses de fatigue par la méthode de Dirlik ont été réalisées sur un modèle de plaque. La MEF a été utilisée pour vérifier les résultats obtenus par fatigue et des tests expérimentaux ont été utilisés pour donner une relative conclusion sur les méthodes. Dans la troisième partie, une plaque en forme de L et un modèle de tour d'éolienne ont également été étudiés en fatigue aléatoire dans la troisième partie. Les résultats obtenus en termes de dommages ont été validés par la MEF et un programme Matlab que nous avons développé. Dans la quatrième partie, une optimisation isogéométrique a été développées sur le modèle de tour en combinant la programmation Matlab et LS DYNA.

Pour conclure, l'IGA est adaptée aux simulations numériques de structures mécaniques étant donné que les résultats obtenus mettent en évidence :

- l'IGA est efficace en termes de génération de maillage par rapport à la MEF.
- l'IGA peut fournir des résultats similaires à la MEF avec une erreur relative acceptable étant donné que pour le calcul des dommages, l'IGA nécessite moins de points d'intégration et d'éléments de maillage.

- L'optimisation avec des variables de conception comme points de contrôle peut fournir des modèles cohérents.

Mots clés Analyse isogéométrique ; Méthode des éléments finis ; Vibration aléatoire ; Essais numériques et expérimentaux

Acknowledgement

Firstly, I would like to express my sincere gratitude to my supervisor madame Khalij for the continuous support of my PhD study and related research, for her patience, motivation, and immense knowledge. Her guidance helped me in all the time of research and writing of this thesis.

I also thank my supervisor madame Troian who read my numerous revisions and helped clarify the confusion. She is an ideal teacher, mentor, and thesis supervisor, offering advice and encouragement with a perfect blend of insight and humor. I'm proud of and grateful for my time working with her.

My sincere thanks also go to professor Lemosse, professor Aoues, Dr. Haobai, Dr. Jieshi, who provided me with valuable advice. Without their precious instructions and support, it would be hard to conduct this research.

I thank my friends Adrien, Ad Elia, Simon, Benoît, Grégoire, Manon, Judith, Laurent, Damien, Doorian, Morgan, Adeline. Their friendship and music accompanied me these years and helped me pass through the difficult time.

My special thanks go to Mimi, Guy, Pascal, Arnould, Nicola, Christine, Jacques and Marie. In a foreign country, they accepted me as their family member. I appreciate these experiences, which I never forget in my life.

I also appreciate the financial support from the China Scholarship Council (CSC). Without the scholarship, it would be difficult for me to focus on my PhD studies.

Last but not the least, I would like to thank my family: my mother, my sister for supporting me spiritually throughout writing this thesis and my life in general.

Contents

| | |
|---|--------------|
| Abstract | i |
| Acknowledgement | iv |
| General Introduction | viii |
| List of Figures | xii |
| List of Tables | xviii |
| List of Terms and Abbreviations | xix |
| 1 Fatigue Induced by Deterministic and Random Loading | 1 |
| 1.1 Introduction | 1 |
| 1.2 Deterministic fatigue analysis | 3 |
| 1.2.1 Cumulative damage for variable amplitudes of stresses | 5 |
| 1.2.2 Factors affecting fatigue strength | 5 |
| 1.2.3 Summary | 7 |
| 1.3 Random vibration fatigue analysis | 8 |
| 1.3.1 Gaussian and stationary random process | 8 |
| 1.3.2 Fatigue analysis induced by random acceleration | 9 |
| 1.3.3 Cumulative fatigue and frequency formulation for random excitation | 11 |
| 1.3.4 Fatigue analysis under different probability density functions | 12 |
| 1.3.5 The random time signal generation from the corresponding PSD function | 15 |
| 1.3.6 Equivalent stress for random loading | 15 |
| 1.4 Conclusion | 16 |
| 2 Isogeometric Analysis Approach | 17 |
| 2.1 Introduction | 17 |
| 2.2 Theoretical background | 18 |
| 2.2.1 Bézier, B-spline, NURBS | 18 |
| 2.2.2 Basic concepts related to IGA | 32 |
| 2.3 State of the art in IGA | 36 |

| | | |
|----------|---|------------|
| 2.4 | Comparison with FEA | 44 |
| 2.5 | Application on a simple example | 45 |
| 2.5.1 | Analysis preparation | 45 |
| 2.5.2 | Analysis results | 47 |
| 2.5.3 | Analytical solution | 49 |
| 2.6 | Conclusion | 50 |
| 3 | Random Vibration Fatigue Analysis on Mechanical Structures | 51 |
| 3.1 | Introduction | 51 |
| 3.2 | Application on a specimen with a reduced section | 52 |
| 3.2.1 | Numerical study | 52 |
| 3.2.2 | Comparison with experimental tests | 63 |
| 3.2.3 | Summary | 67 |
| 3.3 | L-shaped specimen | 68 |
| 3.3.1 | The analysis preparation | 68 |
| 3.3.2 | Analysis results | 69 |
| 3.3.3 | Summary | 74 |
| 3.4 | Conclusion | 76 |
| 4 | Wind Turbine Tower optimization | 77 |
| 4.1 | Introduction | 77 |
| 4.2 | Random vibration fatigue analysis | 78 |
| 4.3 | Sizing optimization | 85 |
| 4.3.1 | Analysis preparation | 85 |
| 4.3.2 | Sizing optimization results | 86 |
| 4.4 | The first shape optimization | 89 |
| 4.4.1 | Analysis preparation | 89 |
| 4.4.2 | Shape optimization results | 90 |
| 4.5 | The second shape optimization | 94 |
| 4.5.1 | Analysis preparation | 94 |
| 4.5.2 | Analysis results | 95 |
| 4.6 | Conclusion | 97 |
| 5 | Conclusions | 98 |
| | Appendices | 100 |
| A | IGA Formulation in vibration | 100 |
| B | IGA in Ls Dyna | 103 |

| | | |
|----------|-----------------------------------|------------|
| C | Wind load calculation | 110 |
| D | General analysis procedure | 117 |
| | Bibliography | 119 |

General Introduction

Based on industrial data, 80 to 95% of mechanical structures fail to function due to fatigue [1], in which most loadings are random. It's essential to predict the structural fatigue strength before its application in a working environment.

Under most circumstances, the fatigue analysis relies on the FEA, which has some weaknesses. Firstly, the time spent in the mesh generation process is often much longer than analysis time [2]. It is assumed that 80% of overall analysis time is spent on the mesh generation in automotive, aerospace, and shipbuilding industries [3]. Furthermore, it is necessary to communicate with the original geometry model during each mesh refinement process. Secondly, the approximate finite element mesh model often results in inaccurate analysis results.

On the other hand, the geometry and analysis models have different representations in the FEA field. The shape optimization with design variables as element nodes would result in zigzag and unrealistic shapes. Moreover, an extra post-processing step is required to exchange data with the CAD system to obtain the final design results, making the structural optimization more complicated.

At present, mechanical structures often consist of numerous components. It is vital to develop structural fatigue analysis and design optimization with a compact, time-efficient analysis process, precise and ideal analysis results to improve the effectiveness and efficiency.

Pitoiset et al. [4] proposed two kinds of frequency domain fatigue analysis methods, the equivalent von Mises stress and multiaxial rainflow methods, to evaluate the high cycle fatigue damage of a supported rectangular plate subjected to a band-limited white noise random pressure. The results show that the two approaches can provide similar PSD functions and damage ratios, allowing a designer to localize the most critical elements. After, Pitoiset et al. [5] also applied frequency domain fatigue analysis methods on an L-shaped plate model subjected to multiaxial random loading to estimate the high-cycle fatigue life and compared the analysis results with the critical plane time-domain method. It has been found that compared with the time-domain approach, the frequency domain methods are extremely time-saving (17 seconds for the equivalent von Mises stress, 1.6 minutes for the multiaxial rainflow, and one week for the critical plane) and have a good agreement in localizing critical areas in the structure. E.Dowling [6] investigated the different fatigue life correction methods, including Goodman, Morrow, and Smith Watson Topper (SWT) and Walker as their ability to correlate stress and strain life on several sheets of steel and nonferrous metals, and obtained the following conclusions from stress-life correlation: 1) the modified Goodman equation with ultimate tensile strength was found to be highly inaccurate; 2) the Morrow equation using the true fracture strength worked well on certain materials;

3) the Morrow expression with fatigue strength coefficient led to non-conservative values; 4) the SWT method was a rational choice that can avoid above shortcomings; 5) Walker method with an adjustable exponent can fit very well with the test data, allowing higher accuracy. Seong-in Moon et al. [7] proposed a methodology to decide the optimum vibration fatigue test, which gives an equivalent failure mode with driving test condition, through a series of vibration fatigue analyses by changing acceleration directions and magnitudes. Arshad et al. [8] developed frequency domain random vibration fatigue analysis on an auxiliary heater bracket in Abaqus commercial software. By modifying the geometry model, an infinite fatigue life in 1σ and 2σ level of confidence was achieved. It has been concluded that Abaqus is efficient in modeling random vibration fatigue. Adam et al. [9] firstly proposed to take into account the effects of mean stress on the fatigue life calculation using the spectral method, in which the PSD has been determined based on the transformed stress considering the mean value, and the detailed steps have been presented. Essam et al. [10] developed random vibration fatigue analysis on a landing gear based on spectral methods with the use of different ways, including Dirlik, Steinberg, Hancock, Wirsching, Tunna, Chaudhury, and Dover in Ls Dyna commercial software. Through comparison of analysis results, it was observed that there were many discrepancies among obtained fatigue life based on these methods. Yusuf et al. [11] developed finite element random vibration fatigue analysis on a cantilever beam using different damage models and compared fatigue life of the beam obtained from the frequency domain, time domain, and experimental test. On the other hand, they also studied the effects of the damping ratio on damage results. It has been observed that the damping ratio is vital to determine correct fatigue damage, and compared with other damage models, the Dirlik method can provide more rational results. Giovanni de Morai Teixeira [12] developed random vibration fatigue analysis on a notched plate in the software Fe-safe. The analysis results were validated by the time-domain method based on an equivalent approach, predicting that the fatigue life from frequency and time domain fatigue analysis at critical locations differs by 20%, in the acceptable range. It was concluded that the random fatigue analysis in fe-safe is robust and can provide accurate results. Yun Huang et al. [13] developed frequency and time domain fatigue analysis on different cases in commercial software Ls Dyna, in which in the frequency domain, random and steady-state vibration fatigue analysis were introduced, and in the time domain, stress and strain-based fatigue analysis were applied. In the frequency domain fatigue analysis, the mean stress correction methods, such as Goodman, Soderberg, Gerber, were developed on a bracket model. From analysis results, it can be shown that the adoption of mean stress correction can lead to obtaining shorter fatigue life. Demirel [14] developed random vibration fatigue analysis on a rectangular cross-section notched beam based on Dirlik's model, studied the effects of modal damping ratio on fatigue analysis results, and validated the fatigue analysis results with an experimental test. However, some discrepancies in fatigue analysis and experimental test results have been found, which have been explained by the different ultimate tensile strength values, damping ratio, and the difficulties of observing the crack initiation time in a real experimental test. Böhm et al. [15] developed frequency and time domain random vibration fatigue analysis with the application of mean stress compensation in hybrid materials consisting of three layers of aluminum and two layers of Glass Fiber Reinforced Polymer, in which the fatigue life was calculated under three different fiber orientations. It has been observed that in a high-cycle fatigue regime, the fatigue life calculated from Rainflow and spectral methods show good agreement; in a low-cycle fatigue regime, compared with the Goodman model, the fatigue life based on the

Gerber model can provide good compatibility between Rainflow and spectral calculations.

Based on the papers above, it can be concluded that the fatigue analysis mainly focused on the numerical simulation and experimental test. In terms of numerical analysis: some mean stress compensation methods, including Goodman and Gerber, were proposed; different fatigue analysis methods like Dirlik, Steinberg, Tuna were applied to analyze fatigue damage in the frequency domain, and the results were validated by the Rainflow counting method in the time domain or experimental tests. It can also be found that almost all of the fatigue analysis simulations were based on the FEA, in which the approximate mesh models may lead to inaccurate results.

Therefore, this work addresses to develop a random vibration fatigue analysis and design optimization on a complex mechanical structure based on a new numerical analysis method, IGA. In the beginning, the IGA was carried on plate models to validate the static, convergence, and fatigue analysis results by an analytical solution, experimental test, FEA, and Matlab programming. Then, the isogeometric random vibration fatigue analysis and design optimization were developed on a wind turbine model and validated by FEA and Matlab programming.

This thesis consists of 6 chapters, organized as follows. Chapter 1 focuses on the theories related to the fatigue damage calculation induced by deterministic and random loading, followed by the chapter conclusion. The isogeometric modeling is described in Chapter 2. It starts from the description of fundamental theories, concepts, and research state of IGA. At the same time, the IGA is considered on a simple plate model, based on the validation by an analytical solution. Chapter 3 presents the IGA on a specimen and an L-shaped plate model. The isogeometric static, convergence, and random vibration fatigue analysis are respectively taken into account in which the fatigue analysis results are validated by FEA, Matlab programming, and experimental tests. The isogeometric random vibration fatigue analysis, size, and shape optimization are carried on a wind turbine tower model in Chapter 4 with the design variables of tower segment thicknesses and control point position, respectively. Chapter 5 summarizes this work. IGA formulations, wind loads calculation, the IGA procedures in Ls Dyna, and this work's general analysis procedures are given in the appendices.

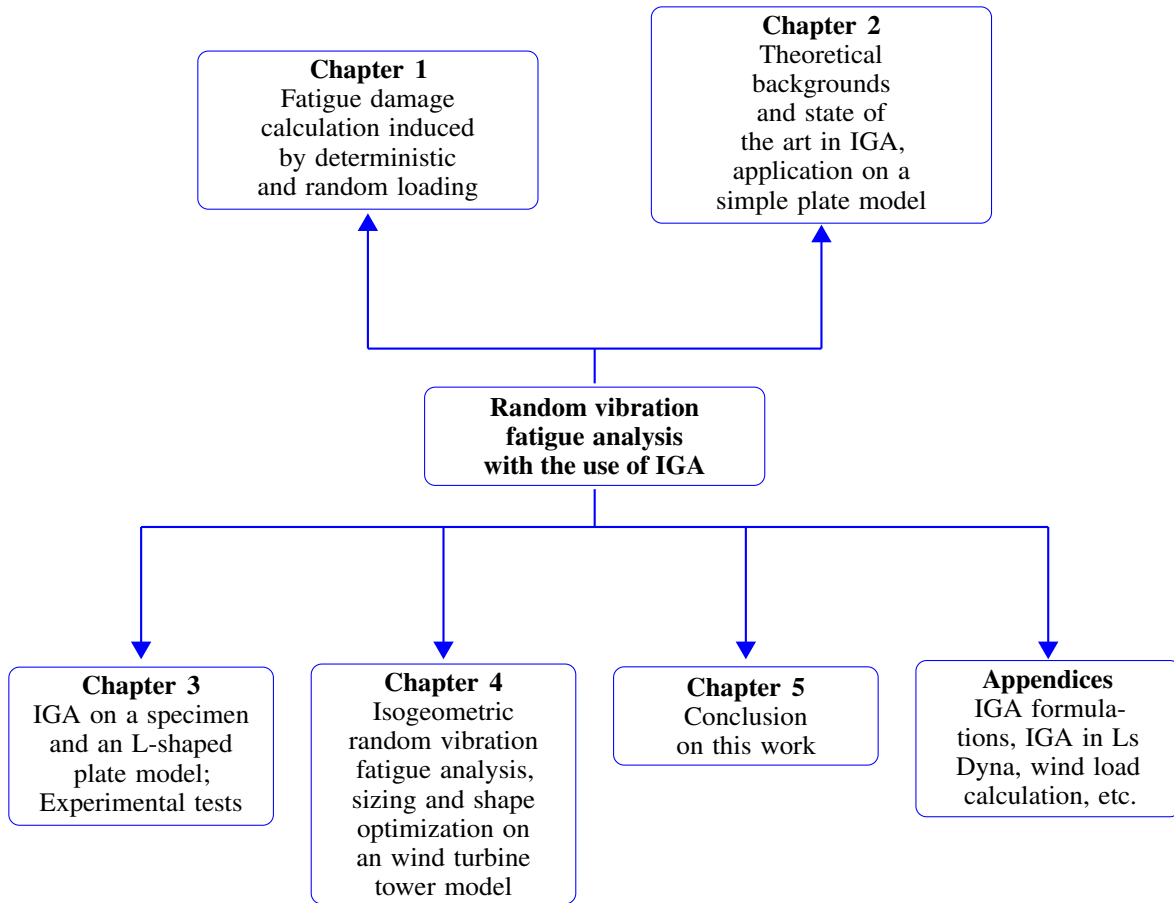


Figure 1: Schematic illustration of the thesis outline

List of Figures

| | | |
|------|---|----|
| 1 | Schematic illustration of the thesis outline | xi |
| 1.1 | Schematic illustration of the first chapter | 3 |
| 1.2 | Schematic illustration of a material S-N curve | 4 |
| 1.3 | Deterministic fatigue analysis procedures | 7 |
| 1.4 | Schematic illustration of a random process | 8 |
| 1.5 | Bandwidth definition | 12 |
| 1.6 | Vibration fatigue analysis procedures in the frequency domain | 14 |
| 2.1 | Schematic illustration of the second section | 18 |
| 2.2 | Bernstein basis functions | 19 |
| 2.3 | Bézier curve | 20 |
| 2.4 | Bézier surface | 21 |
| 2.5 | Constant basis functions corresponding to $\Xi = \{0, 0, 0, 0.5, 1, 1, 1\}$ | 23 |
| 2.6 | Linear basis functions corresponding to $\Xi = \{0, 0, 0, 0.5, 1, 1, 1\}$ | 24 |
| 2.7 | Quadratic basis functions corresponding to $\Xi = \{0, 0, 0, 0.5, 1, 1, 1\}$ | 26 |
| 2.8 | B-spline curve corresponding to the knot vector $\Xi = \{0, 0, 0, 0.5, 1, 1, 1\}$ | 27 |
| 2.9 | B-spline surface | 28 |
| | (a) $R_{1,2}$ | 29 |
| | (b) $R_{2,2}$ | 29 |
| 2.10 | NURBS basis functions corresponding to $\Xi = \{0, 0, 0, 0.5, 1, 1, 1\}$ | 30 |
| | (c) $R_{3,2}$ | 30 |
| | (d) $R_{4,2}$ | 30 |
| 2.11 | NURBS curve | 31 |
| 2.12 | NURBS surface | 32 |
| 2.13 | Schematic illustration of different spaces | 33 |
| | (a) Index space | 33 |
| | (b) Parameter space | 33 |
| | (c) Physical space | 33 |
| 2.14 | Schematic illustration of the space transformations | 35 |
| 2.15 | Schematic illustration of patch elements | 36 |
| | (a) Model 1 | 36 |
| | (b) Model 2 | 36 |
| 2.16 | Schematic illustration of mesh elements | 36 |
| 2.17 | T-spline repairment (from [16]) | 37 |
| | (a) B-spline surfaces | 37 |
| | (b) T-splines | 37 |
| 2.18 | NURBS, T-spline control mesh and surfaces (from [17]) | 38 |
| | (a) NURBS and T-spline control mesh | 38 |
| | (b) NURBS and T-spline surfaces | 38 |

| | | |
|------|--|----|
| (a) | Underbody cross member | 40 |
| 2.19 | Isogeometric and finite element analysis comparison on a underbody cross member (from [18]) . . . | 41 |
| (b) | Comparison of contact forces between upper die and blank | 41 |
| (c) | Comparison of necessary CPU-time | 41 |
| 2.20 | NURBS surfaces (from [19]) | 43 |
| (a) | Initial NURBS surface | 43 |
| (b) | Modified NURBS surface after the position of control point Q is changed from Q_a to Q_b | 43 |
| (c) | Modified NURBS surface after the weight of control point ω is changed from ω_a to ω_b | 43 |
| 2.21 | Meshing process in isogeometric and finite element analysis. | 44 |
| 2.22 | The schematic diagram of of the plate model | 46 |
| 2.23 | Mesh models and boundary conditions | 47 |
| (a) | IGA | 47 |
| (b) | FEA | 47 |
| 2.24 | Convergence analysis results | 48 |
| (a) | IGA | 48 |
| (b) | FEA | 48 |
| 2.25 | Maximum stresses in y directions | 49 |
| (a) | IGA | 49 |
| (b) | FEA | 49 |
| 2.26 | Schematic diagram of a plate model | 50 |
| 3.1 | Schematic illustration of the third Chapter | 52 |
| 3.2 | The plate model with reduced section | 53 |
| 3.3 | Mesh models and boundary conditions | 54 |
| (a) | IGA | 54 |
| (b) | FEA | 54 |
| 3.4 | Convergence analysis results | 55 |
| (a) | IGA | 55 |
| (b) | FEA | 55 |
| 3.5 | The effective stress | 56 |
| (a) | IGA | 56 |
| (b) | FEA | 56 |
| 3.6 | Isogeometric first five vibration modes | 57 |
| (a) | First | 57 |
| (b) | Second | 57 |
| (c) | Third | 57 |
| (d) | Fourth | 57 |
| (e) | Fifth | 57 |
| (a) | First | 57 |
| (b) | Second | 57 |
| (c) | Third | 57 |
| 3.7 | Finite element first five vibration modes | 58 |
| (d) | Fourth | 58 |
| (e) | Fifth | 58 |
| 3.8 | Applied acceleration PSD | 58 |
| 3.9 | Effective stress PSD | 59 |
| 3.10 | The effective stress RMS | 60 |
| (a) | IGA | 60 |
| (b) | FEA | 60 |

| | | |
|------|--|----|
| (a) | Steinberg | 61 |
| (b) | Dirlik | 61 |
| (c) | Narrow band | 61 |
| (d) | Wirshing | 61 |
| (e) | Chaudhury and Dover | 61 |
| (f) | Tunna | 61 |
| 3.11 | Isogeometric cumulative damage ratios | 61 |
| (g) | Hancock | 61 |
| 3.12 | Finite element cumulative damage ratios | 62 |
| (a) | Steinberg | 62 |
| (b) | Dirlik | 62 |
| (c) | Narrow band | 62 |
| (d) | Wirshing | 62 |
| (e) | Chaudhury and Dover | 62 |
| (f) | Tunna | 62 |
| (g) | Hancock | 62 |
| 3.13 | Schematic representation of the system | 63 |
| (a) | The vibration-based bending fatigue bench | 63 |
| (b) | The schematic details | 63 |
| 3.14 | Frequency responses during fatigue test (4 measures) | 64 |
| (a) | Complete signal during fatigue test | 64 |
| 3.15 | Strain measure | 65 |
| (b) | A focus of signal | 65 |
| 3.16 | Spectrogram obtained from strain measure | 65 |
| 3.17 | Resonant frequency deviation during fatigue test | 66 |
| (a) | Versus time | 66 |
| (b) | Versus number of cycle | 66 |
| 3.18 | Dimensions of the plate (in mm) | 68 |
| 3.19 | Mesh models | 69 |
| (a) | IGA | 69 |
| (b) | FEA | 69 |
| (c) | Splitted geometry model | 69 |
| 3.20 | Convergence analysis | 70 |
| (a) | IGA | 70 |
| (b) | FEA | 70 |
| (a) | First | 71 |
| (b) | Second | 71 |
| (c) | Third | 71 |
| (d) | Fourth | 71 |
| 3.21 | Isogeometric first five vibration modes | 71 |
| (e) | Fifth | 71 |
| (a) | First | 72 |
| (b) | Second | 72 |
| (c) | Third | 72 |
| (d) | Fourth | 72 |
| 3.22 | Finite element first five vibration modes | 72 |
| (e) | Fifth | 72 |
| 3.23 | Applied load PSD | 73 |
| 3.24 | Effective stress PSD | 74 |

| | | |
|------|--|----|
| 3.25 | Effective stress RMS | 74 |
| (a) | IGA | 74 |
| (b) | FEA | 74 |
| 3.26 | Cumulative damage ratio | 74 |
| (a) | IGA | 74 |
| (b) | FEA | 74 |
| 4.1 | Schematic illustration of the fourth chapter | 78 |
| 4.2 | Layout of a 45 KW wind turbine tower with a height of 38 m | 78 |
| 4.3 | Geometric model (in mm) | 79 |
| 4.4 | Mesh models | 80 |
| (a) | IGA | 80 |
| (b) | FEA | 80 |
| (c) | Flange model for IGA | 80 |
| (d) | Flange model for FEA | 80 |
| (a) | First | 81 |
| (b) | Second | 81 |
| (c) | Third | 81 |
| 4.5 | Isogeometric first five vibration modes | 82 |
| (d) | Fourth | 82 |
| (e) | Fifth | 82 |
| (a) | First | 82 |
| (b) | Second | 82 |
| (c) | Third | 82 |
| 4.6 | Finite element first five vibration modes | 82 |
| (d) | Fourth | 82 |
| (e) | Fifth | 82 |
| 4.7 | Effective stress PSD | 83 |
| 4.8 | Effective stress RMS | 83 |
| (a) | IGA | 83 |
| (b) | FEA | 83 |
| 4.9 | Cumulative damage ratio | 84 |
| (a) | IGA | 84 |
| (b) | FEA | 84 |
| 4.10 | Sizing optimization procedures | 86 |
| 4.11 | Isogeometric sizing optimization results | 87 |
| (a) | Sizing optimization result | 87 |
| (b) | Sizing optimization result with consideration of mass constraint | 87 |
| 4.12 | Finite element sizing optimization results | 88 |
| (a) | Sizing optimization result | 88 |
| (b) | Sizing optimization result with consideration of mass constraint | 88 |
| 4.13 | NURBS curves for the door | 89 |
| (a) | NURBS curves | 89 |
| (b) | Same control points | 89 |
| (c) | Fixed control points | 89 |
| (a) | Without constraint | 90 |
| 4.14 | Isogeometric shape optimization results | 91 |
| (b) | With mass constraint | 91 |
| (c) | With mass constraint | 91 |

| | | |
|------|--|-----|
| (a) | Without constraint | 92 |
| 4.15 | Isogeometric shape optimization results | 93 |
| (b) | With mass constraint | 93 |
| (c) | With mass constraint | 93 |
| 4.16 | Isogeometric shape optimization results | 94 |
| (a) | Original state | 94 |
| (b) | With optimization | 94 |
| (c) | With optimization | 94 |
| 4.17 | Illustration of fixed control points | 94 |
| (a) | Without constraint | 95 |
| (b) | With mass constraint | 96 |
| 4.18 | Isogeometric shape optimization results | 96 |
| (c) | With mass constraint | 96 |
| 4.19 | Isogeometric shape optimization results | 97 |
| (a) | With optimization | 97 |
| (b) | With optimization | 97 |
| (a) | Plate construction | 103 |
| (b) | Circle construction | 103 |
| (c) | Geometry trimming | 103 |
| B.1 | The geometry construction | 104 |
| (d) | Created model | 104 |
| (e) | Final model | 104 |
| B.2 | The mesh model construction | 105 |
| (a) | Rough mesh model | 105 |
| (b) | Mesh refinement | 105 |
| (c) | Final mesh model | 105 |
| B.3 | Element shell NURBS patch | 106 |
| B.4 | Material, section properties and boundary condition setting | 107 |
| (a) | Material properties | 107 |
| (b) | Section properties | 107 |
| (c) | Boundary condition | 107 |
| B.5 | The setting procedures of load application on control points | 108 |
| (a) | Material properties | 108 |
| (b) | Section properties | 108 |
| (c) | Boundary condition | 108 |
| B.6 | load applied on NURBS elements | 108 |
| B.7 | Modal analysis procedures | 109 |
| (a) | Material properties | 109 |
| (b) | Section properties | 109 |
| (c) | Boundary condition | 109 |
| B.8 | Fatigue analysis procedures | 109 |
| (a) | First | 109 |
| (b) | Second | 109 |
| (c) | Third | 109 |
| C.1 | Wind velocity against the height in Normandy region | 111 |
| C.2 | The wind speed PSDs | 114 |
| C.3 | The normalized wind speed PSDs | 115 |
| C.4 | The force PSD | 116 |

| | | |
|-----|---|-----|
| (a) | Wind force PSD | 116 |
| (b) | Normalized wind force PSD | 116 |
| C.5 | Eurocode 1 force PSDs | 116 |
| (a) | Longitudinal force PSDs | 116 |
| (b) | Lateral force PSDs | 116 |
| (c) | Vertical force PSDs | 116 |
| (d) | Vertical force PSDs | 116 |
| D.1 | Schematic illustration of the overall analysis procedures | 117 |
| D.2 | Schematic illustration of the fatigue analysis procedure | 118 |

List of Tables

| | | |
|-----|---|----|
| 2.1 | Material properties | 46 |
| 3.1 | Material properties | 53 |
| 3.2 | The first five natural frequencies (Hz) | 56 |
| 3.3 | The isogeometric and finite element cumulative damage ratios | 60 |
| 3.4 | The fatigue life $E[T_f]$ results related to the 5% variation of σ_f variation (in the units of hours: minutes: seconds) | 63 |
| 3.5 | Results of the fatigue life $E[T_f]$ obtained from the resonant frequency deviation | 66 |
| 3.6 | Material properties | 68 |
| 3.7 | The first five natural frequencies from [5] | 70 |
| 3.8 | The first five natural frequencies (Hz) | 71 |
| 4.1 | Main parameters of the wind turbine tower | 79 |
| 4.2 | Material properties | 79 |
| 4.3 | The first five natural frequencies (Hz) | 81 |
| 4.4 | The first natural frequencies (Hz) | 90 |
| 4.5 | The effective stress RMS | 92 |
| 4.6 | The effective stress RMS | 95 |

Nomenclature

| | |
|---|--|
| FEA: Finite Element Analysis | $\sigma_{-1}, (\sigma_{-1})_k$: Material and component fatigue limit under symmetric cycles |
| IGA: Isogeometric Analysis | |
| NURBS: Non-Uniform Rational B-spline | $(\sigma_{-1})_d, (\sigma_{-1})_{d_0}$: Symmetric cycle fatigue limit under the specimen diameters of d and d_0 |
| PSD: Power Spectrum Density | $(\sigma_{-1})_{\beta_S}, (\sigma_{-1})_{\beta_0}$: Symmetric cycle fatigue limit under certain and fine polishing surface states |
| FRF: Frequency Response Function | |
| CDF: Cumulative Distribution Function | K_σ : Component stress concentration coefficient |
| PDF: Probability Density Function | ϵ_σ : Component dimension coefficient |
| SSS: Strict Sense Stationary random process | β_σ : Component surface state coefficient |
| WSS: Wide Sense Stationary random process | $(K_\sigma)_D$: Comprehensive impact coefficient |
| R : Fatigue cycle characteristic | σ_a : Stress amplitude |
| N : Fatigue cycle number | σ_{ar} : Obtained stress amplitude from the Goodman equation |
| S_{rN} : Fatigue limit under the cycle characteristic r and cycle number N | σ_m : Mean stress |
| $C, \beta, \sigma_f = C^{\frac{1}{\beta}}, b = -\frac{1}{\beta}$: Material constants | s_d : Safety coefficient |
| K_N : Fatigue life coefficient | σ_e : von Mises stress |
| N_b : Base cycle number | $\sigma = (\sigma_1, \sigma_2, \sigma_3, \sigma_{12}, \sigma_{23}, \sigma_{31})^T$: Stress vector |
| σ_b : Base fatigue limit (endurance limit) | $\sigma_1, \sigma_2, \sigma_3$: Normal stresses |
| σ_u : Ultimate strength | $\sigma_{12}, \sigma_{23}, \sigma_{13}$: Shear stresses |
| N : Applied cycle number | Q : Matrix used in definition of von Mises stress |
| N_f : Number of cycles allowable at a particular stress amplitude | $\sigma(t)(t \in T)$: A random process |
| $[\sigma_{-1}]$: Allowable stress under a symmetric cycle | $\sigma_i, i = 1, 2, \dots$: Random variable |
| $[\sigma_0]$: Allowable stress under a pulsating cycle | $t \in T$: Time parameter |
| | τ : Time shift |

| | |
|---|---|
| $E[\sigma\sigma^T]$: Covariance matrix of the stress vector σ | $R_{i,p}(\xi), R_{i,j}^{p,q}(\xi, \eta), R_{i,j,k}^{p,q,z}(\xi, \eta, \zeta)$: Univariate, bivariate, trivariate NURBS basis functions |
| $\Phi_{\sigma\sigma}(\omega)$: PSD of the stress vector | |
| $\Phi_c(\omega)$: PSD of the equivalent von Mises stress | $W(\xi)$: Weighted linear combination of B-spline basis functions |
| D : Total damage for deterministic loading | n, m, l : Number of basis functions along ξ, η, ζ parametric directions |
| $E[N_0^+]$: Expected number of zero-crossing per unit time | |
| $E[T_f]$: Fatigue life for random loading (sec.) | $\mathbf{P}_i, \mathbf{P}_{i,j}, \mathbf{P}_{i,j,k}$: Control point vector, net and volume arrays |
| $F_\sigma(r)$: Cumulative density function of stress | n_{cp}^e : Number of control points in element Ω^e |
| $E[p]$: The number of peak per second | n^e : Number of nodes in element Ω^e |
| $E[D]_{NB}$: Cumulative damage ratio defined by Benda's PDF | $\Omega^e, \tilde{\Omega}^e, \overline{\Omega}^e$: An element in the physical space, parameter space, and parent domain |
| $E[D]_W$: Wirching's cumulative damage ratio expression | n_{gp}^e : Number of Gauss points |
| $(\sigma_{eq})_{\text{Hancock}}, (\sigma_{eq})_{\text{C and D}}, (\sigma_{eq})_{\text{Steinberg}}$: Equivalent stress expression given by Hancock, Chaudhuery and Dover, and Steinberg | \mathbf{K} : Stiffness matrix |
| $p_{\sigma_B}(r), p_{\sigma_T}(r), p_{\sigma_D}(Z)$: Benda, Tuna, Dirlik's PDF | \mathbf{M} : Mass matrix |
| γ : Irregularity factor | \mathbf{F} : Force vector |
| e, cp : Element and control point | $\mathbf{e} = (e_1, e_2, e_3)^T$: Orthonormal basis |
| f : Frequency (Hz) | \mathbf{f} : Deterministic volume force |
| $\sqrt{m_0}$: Root mean square value of stress | \mathbf{n} : Outward normal vector |
| m_k : k th order spectral moment | \mathbf{t} : Deterministic surface force |
| n^e : Number of element | \mathbf{u}, \mathbf{u}^e : Global and element displacement vector |
| n_{cp}^e : Number of control points in an element e | $\dot{\mathbf{u}}, \ddot{\mathbf{u}}$: Velocity and acceleration vectors |
| p, q, z : Polynomial order along ξ, η and ζ parametric directions | $\mathbf{x} = (x, y, z)^T$: Global Cartesian reference system |
| $B_{i,p}(\xi), B_{j,q}(\eta), B_{k,z}(\zeta)$: i th, j th, k th Bernstein basis functions of order p, q, z along ξ, η, ζ parametric directions | \mathbf{B} : Strain displacement matrix |
| $N_{i,p}(\xi), M_{j,q}(\eta), R_{k,z}(\zeta)$: i th, j th, k th B-spline basis functions of order p, q, z along ξ, η, ζ parametric directions | \mathbf{C} : Damping matrix |
| | \mathbb{C} : Fourth order material constitutive tensor |
| | \mathbf{F}, \mathbf{F}^e : Global and element external force vector |
| | $ \mathbf{H}(f) $: Magnitude of frequency response matrix |
| | \mathbf{K}, \mathbf{K}^e : Global and element stiffness matrix |
| | \mathbf{P}_i : i th control point vector |

\mathbf{R} : NURBS basis functions matrix

$\mathbf{S}_{FF}(f)$: External force PSD matrix

$\mathbf{S}_{uu}(f)$: Displacement PSD matrix

$\mathbf{S}_{\sigma\sigma}(f)$: Stress PSD matrix

ε : Strain tensor

η : Parametric coordinates given by ξ in one dimension,
 (ξ, λ) in 2 dimensions and (ξ, λ, ζ) in 3 dimensions

σ : Cauchy stress tensor

Ξ, Λ : Knot vectors

$E[\cdot]$: Expected value operator

δ : Use for virtual quantities

∇ : Divergence operator

\otimes : Tensor Product

Chapter 1

Fatigue Induced by Deterministic and Random Loading

1.1 Introduction

In the mid-nineteenth century, with the invention of steam locomotives, it was discovered that wheel structures failed under the limit stresses far less than their static strength, promoting the occurrence of general fatigue problems. Then, it was observed that under the effects of structural resonance frequency, a vehicle would also experience failure, even though the load was much smaller than the general fatigue load, and this contributed to the occurrence of vibration fatigue problems (or dynamic fatigue problems) [20]. Fatigue is defined as the progressive and localized structural damage caused by repeated loads [7, 11]. In the beginning, only static fatigue analysis that doesn't consider the inertial effects has attracted much attention. In 1963 S.H.Crandall and W.D.Mark firstly proposed that vibration fatigue is irreversible and is a cumulative damage process caused by dynamic loads [21]. However, it's not enough for a vibration fatigue analysis. In recent decades, Yao Qihang, Yao Jun, Zhang Azhou et al. [20, 22–25] proposed that "vibration fatigue" refers to the fatigue damage caused by applied dynamic loads including vibration, noise, harshness approximate the natural frequency of a system.

The fatigue failures are featured by: 1) under the repetitive action of alternating load, fatigue may also occur, even though the obtained component stress is much smaller than the material's strength limit (sometimes elastic limit); 2) regardless of whether a material is brittle or plastic, macroscopically, the sudden fatigue fracture is featured by no obvious plastic deformation and low-stress brittle fracture, which make fatigue damage difficult to predict, and dangerous; 3) there are two main zones close to the fatigue crack areas, the smooth and the rough zone, also termed

as fatigue crack growth zone and fast fracture zone, and these are important criteria in determining fatigue failure; 4) fatigue failure often has a local feature and does not involve all materials of the entire structure. Most of the time, as long as the local detailed design or process measures are changed, the fatigue life can be increased significantly. Therefore, the ability of a structure or component to resist fatigue damage not only depends on the materials used but also sensitively depends on the structural shape, size, components connection and matching form, performance shape, and environmental conditions, etc; 5) fatigue failure is a cumulative damage process, which usually involves crack formation, cracks propagation, and rapid fracture when the crack propagates to a critical size, requiring a certain time history, even a long time course.

The fatigue performance of materials or components under alternating loads can be measured by fatigue strength. The intensity of fatigue strength represented by fatigue limit or endurance limit refers to the maximum stress at which a material or component can withstand unlimited cycles under stress cycle characteristic R . As the fatigue limit of a material varies with the loading method and stress ratio, the fatigue limit under symmetrical stress cycles is used as the basic fatigue limit of the corresponding material. Usually, fatigue life is given as the cycle numbers of stress or strain experienced during a failure, generally denoted by N . The fatigue life of a test piece depends on the mechanical properties of the material and the level of applied stress. Generally speaking, the higher the strength limit of the material and the lower the applied stress level, the longer the fatigue life of a specimen; otherwise, the shorter the fatigue life. Based on the highness of cyclic stress or the condition of occurrence in plastic strain, the fatigue can be classified into stress fatigue or strain fatigue. When the obtained maximum cyclic stress is much less than the corresponding material yield one, and no plastic strain occurs, the fatigue is called stress fatigue. In this situation, the number of stress cycles is relatively high, generally higher than 10^4 times. Therefore, the stress fatigue is also called high cycle fatigue (HCF). On the other hand, if the maximum cyclic stress is higher than the material yield limit, and there is an occurrence of plastic strain, it is more appropriate to use strain as the fatigue life estimation parameter. And due to the lower number in stress cycles, generally less than 10^4 times, the strain fatigue is also called low cycle fatigue.

This chapter provides a general introduction to the theoretical backgrounds of fatigue damage induced by deterministic and random loading. As shown in Fig. 1.1, it begins with the introduction in Section 1.1 in which the historical backgrounds in fatigue analysis, and the concepts in fatigue strength, fatigue limit, fatigue life, stress and strain fatigue are respectively described. Section 1.2 presents the deterministic fatigue analysis theories in S-N curves, Miner's rule, Rainflow counting, etc. Subsequently, Section 1.3 proposes the random vibration fatigue analysis theories such as the definition, classification of random processes, the power spectral density (PSD) and probability density function (PDF), and the fatigue analysis formulation in the frequency domain, etc. The chapter conclusions are given in Section 1.4.

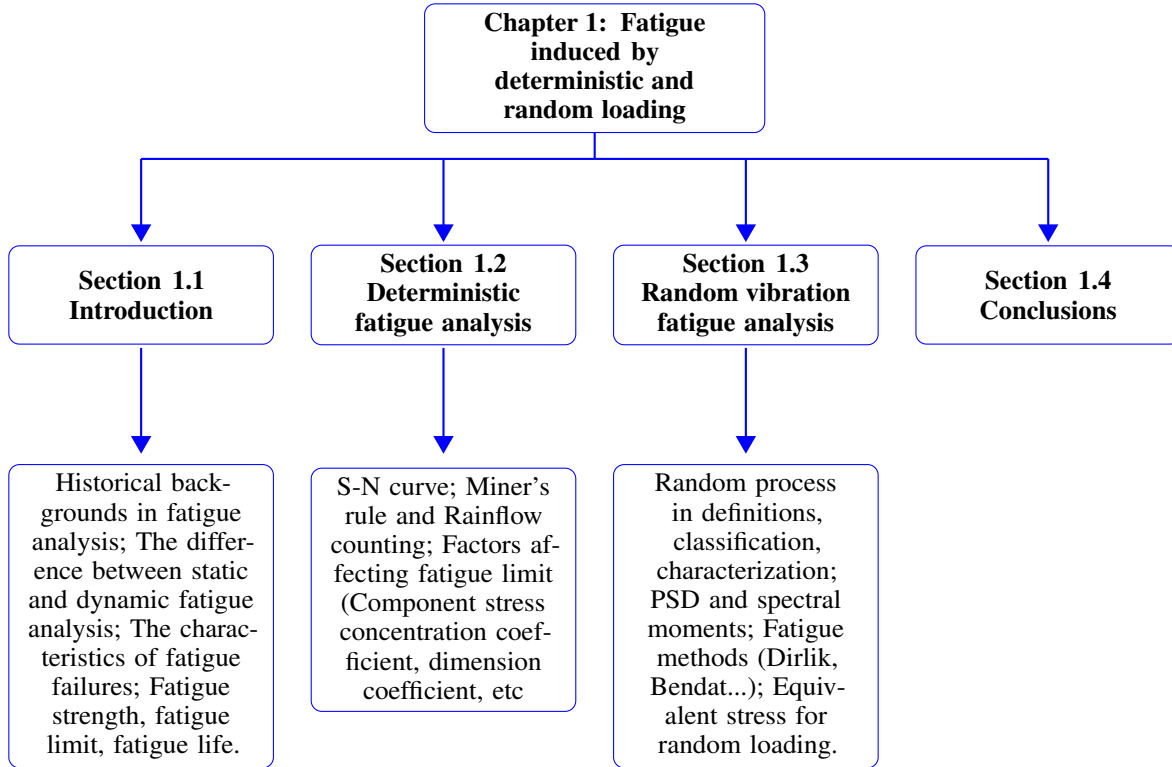


Figure 1.1: Schematic illustration of the first chapter

1.2 Deterministic fatigue analysis

Fatigue is defined as a progressive change in the material properties following the application of loading cycles, the repetition of which can lead to the fracture. Schijve [26] defines fatigue life as the addition of the initiation period and the crack growth period. The author found that more than 90% of the fatigue life is usually spent before detectable cracks under HCF conditions. A cumulative damage calculation is used to quantify the total damage characterized by the fraction of life consumed by the crack initiation.

This study focused on HCF thus the material behaviour remains elastic during the fatigue loading until crack initiation. Therefore, an elastic computation was performed to obtain stress states used for the damage calculations. For deterministic excitation, the linear model of Palmgren-Miner damage accumulation [27], [28] known as Miner's rule, is one of the most widely used methods [29–31]. Let us consider m stress amplitudes denoted $\sigma_{a,i}$ ($i = 1, \dots, m$), which characterize the time history response calculated at the maximum stress location of a structure (by FEA or IGA). The authors assume that each significant stress amplitude extracted from the stress-time history (by using Rainflow counting techniques, see [32], [33]) produces an individual damage and the total damage D is obtained by the following summation:

$$D = \sum_{i=1}^m \frac{1}{N_{f,i}} N_i \quad (1.1)$$

where $N_{f,i}$ is the number of cycles allowable at particular stress before a material fails by fatigue (the number of cycles to failure at constant stress amplitude σ_a) defined from the S-N curve (representing the stress amplitudes versus the number of cycles to failure). N_i the i th applied stress cycle number. For steel structures, if the cumulative fatigue damage reaches a critical value of 1, thus the structure is considered damaged.

The relationship between the fatigue limit σ_{RN} (a particular value of stress amplitude, expressed as σ_a , for the simplification in the following) and cycle number N is called the fatigue curve or S-N curve in which the stress cycle characteristic R is defined as the proportion between the minimum and maximum stresses. As shown in Fig. 1.2, when the cycle number $N < 10^3 - 10^4$, the fatigue limit almost approximates the ultimate strength σ_u and generally can be calculated based on the standard of static strength. When the cycle number $10^3 - 10^4 < N < N_b$, the fatigue limit would decrease with the increase of cycle number N . For most materials, the relationship between the fatigue limit σ_a and cycle number N_f follows the exponent Eq. (1.2). When the fatigue cycle $N > N_b$, or the fatigue limit $\sigma < \sigma_b$, it is traditionally assumed that the fatigue would not happen.

$$\sigma_a^\beta N_f = C \tag{1.2}$$

which can also be written as:

$$\sigma_a = \sigma_f N_f^b \tag{1.3}$$

with $\sigma_f = C^{\frac{1}{\beta}}$ and $b = -\frac{1}{\beta}$.

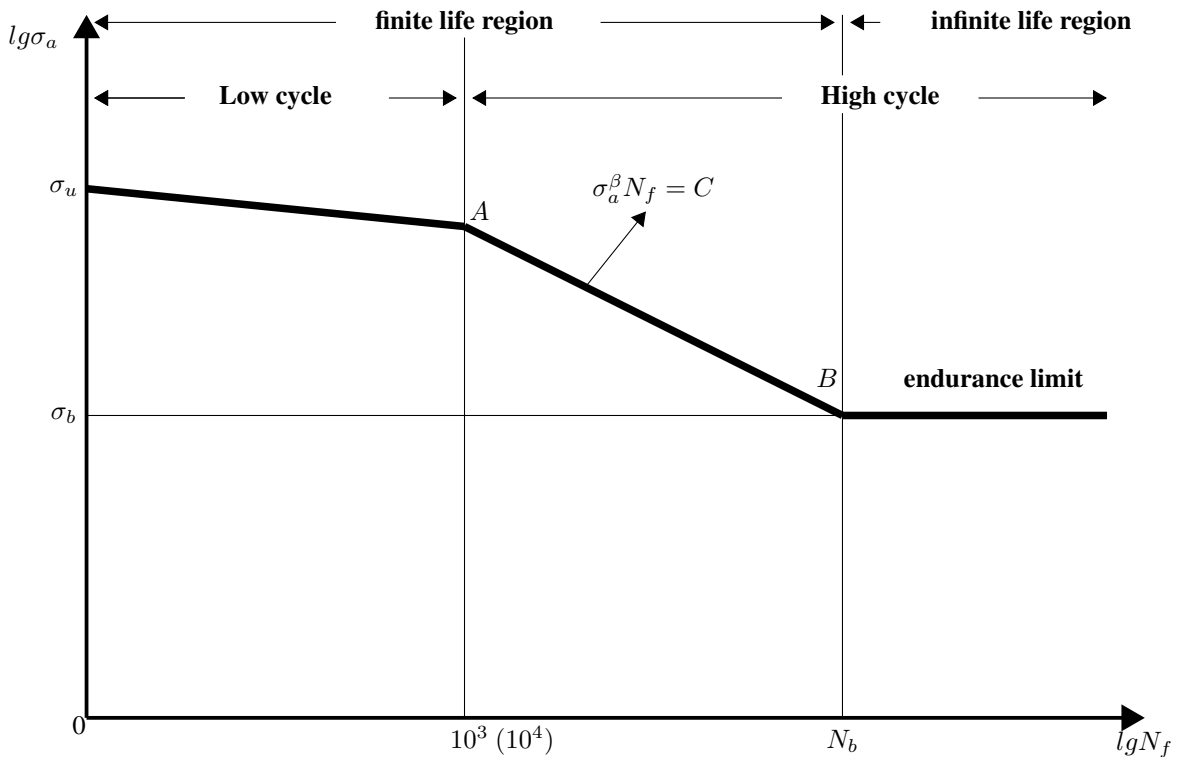


Figure 1.2: Schematic illustration of a material S-N curve

Therefore, with the consideration of Eq. (1.2), Eq. (1.1) becomes:

$$D = \sum_{i=1}^m C^{-1} \sigma_{a,i}^{\beta} N_i \quad (1.4)$$

For a deterministic loading, the fatigue analysis is performed in the time domain while for Gaussian random excitation, it can be developed in the time domain or in the frequency domain.

1.2.1 Cumulative damage for variable amplitudes of stresses

The cumulative damage is easy to calculate when a load signal behaves in a sine function. However, when the load amplitudes are variable, the rainflow cycle counting method, firstly proposed by Matsuishi and Endo [34], is used to count the number of fatigue cycles from a given stress or strain time history. There are several rainflow counting methods, such as hysteresis filtering, Peak-valley Filtering, four-point counting method, etc. The Hysteresis Filtering removes tiny oscillations from the load-time history that contribute negligible damage through the definition of a gate of a specific amplitude. Any cycle with amplitude smaller than the gate would be removed from the load-time history. The purpose of peak-valley filtering is to save data points that are reversals in direction. Any intermediate data points between the maximum and minimum values of a given cycle can be deleted. The four-point counting method roughly requires the following steps: firstly, define inner and outer stress; secondly, based on the inner and outer stress range, the stress cycle is counted; thirdly, store the obtained cycles in a rainflow matrix, which is an $n \times n$ matrix of data, and n equals the number of bins. Then the combination of rainflow counting, material S-N curve, and Miner's rule allows calculating the fatigue damage of a component subjected to complex loads.

1.2.2 Factors affecting fatigue strength

Under the effects of alternating loads, the fatigue strength of a mechanical component is affected by several factors, such as stress concentration, component dimension, surface state, environmental medium, load sequence, load characteristics, etc., in which the first three ones are most significant. Thus, the component fatigue curve is different from the corresponding material counterpart.

- I) Component stress concentration coefficient K_{σ}

With the demands of structures, a component usually has abrupt changes in holes, fillets, grooves, etc., leading to a phenomenon of stress concentration, under a load application. The component stress concentration coefficient K_{σ} is applied to represent the reduced certainties of the material fatigue limit and defined by the Eq. (1.7).

$$K_{\sigma} = \frac{\sigma_{-1}}{(\sigma_{-1})_k} \quad (1.5)$$

where σ_{-1} and $(\sigma_{-1})_k$ are respectively the material and component fatigue limit under a symmetric cycle.

- II) Component dimension coefficient ϵ_S

Under the same conditions, the larger the component dimension, the higher the chance of fatigue defects. This is because when a component size is large, the material particles are coarse, the probability of defects is high, and the fatigue cracks are easy to form. Component dimension coefficient ϵ_S is defined as:

$$\epsilon_\sigma = \frac{(\sigma_{-1})_d}{(\sigma_{-1})_{d_0}} \quad (1.6)$$

where $(\sigma_{-1})_d$ and $(\sigma_{-1})_{d_0}$ are respectively the fatigue limit with the specimen diameters of d and d_0 (normally $d_0 = 6 - 10 \text{ mm}$).

- III) Component surface state coefficient β_σ

The component surface state represent the component surface roughness and surface processing state. It can produce significant effects on fatigue failure in the aspects of crack initiation, stress concentration, and anti-fatigue ability. The Component surface state coefficient β_σ is defined as:

$$\beta_\sigma = \frac{(\sigma_{-1})_{\beta_\sigma}}{(\sigma_{-1})_{\beta_0}} \quad (1.7)$$

where $(\sigma_{-1})_{\beta_\sigma}$ is the fatigue limit under certain surface state, $(\sigma_{-1})_{\beta_0}$ is the fatigue limit under fine polishing.

- IV) The allowable stress

Under considerations of these factors mentioned above and safety coefficient s_d , the allowable stress of the symmetric and pulsating cycle can be defined by the Eqs. (1.8) and (1.9), respectively.

$$[\sigma_{-1}] = \frac{\epsilon_\sigma \beta_\sigma \sigma_{-1}}{k_\sigma s_d} \quad (1.8)$$

$$[\sigma_0] = \frac{\epsilon_\sigma \beta_\sigma \sigma_0}{k_\sigma s_d} \quad (1.9)$$

- V) Component σ_a - σ_m

It has been found that the component stress concentration, dimensions, and surface state coefficients have effects mainly only on stress amplitude σ_a . Thus, through the combination of these three factors, the comprehensive impact coefficient $(K_\sigma)_D$ is decided by Eq. (1.10).

$$(K_\sigma)_D = \frac{k_\sigma}{\epsilon_\sigma \beta_\sigma} \quad (1.10)$$

The component fatigue limit diagram is obtained after the consideration of comprehensive impact coefficient $(K_\sigma)_D$ and fatigue life coefficient K_N . The comprehensive impact coefficient $(K_\sigma)_D$ has effects on the component stress amplitude. The fatigue life coefficient K_N has effects both on the component stress amplitude and mean stress.

1.2.3 Summary

As shown in Fig. 1.3, a deterministic fatigue analysis usually would require Miner's rule, stress cycle counting algorithm, and component S-N curve to calculate the total fatigue damage. In the first step, obtain the stress time history of a structure from numerical simulation methods in which for a multiaxial stress state, the equivalent von Mises stress can be calculated, based on the Eq. (1.41); Then, according to the stress cycle counting method like the rainflow counting approach, compute the stress cycle numbers under different mean and alternating stresses in which for a material S-N curve obtained under the condition of zero mean stress, the component S-N curve with non-zero mean stress can be computed considering the comprehensive impact factor, as shown in Eq. (1.10), and mean stress correlation algorithm like Goodman [35], as shown in Eq. (1.11). In the final step, with the utilization of obtained component S-N curves under different mean stresses, Miner's rule, and stress cycle numbers from the algorithm of stress cycle, calculate the fatigue damage.

$$\frac{\sigma_a}{\sigma_{ar}} = 1 - \frac{\sigma_m}{\sigma_u} \quad (1.11)$$

where σ_{ar} is the obtained stress amplitude, σ_u is the ultimate strength.

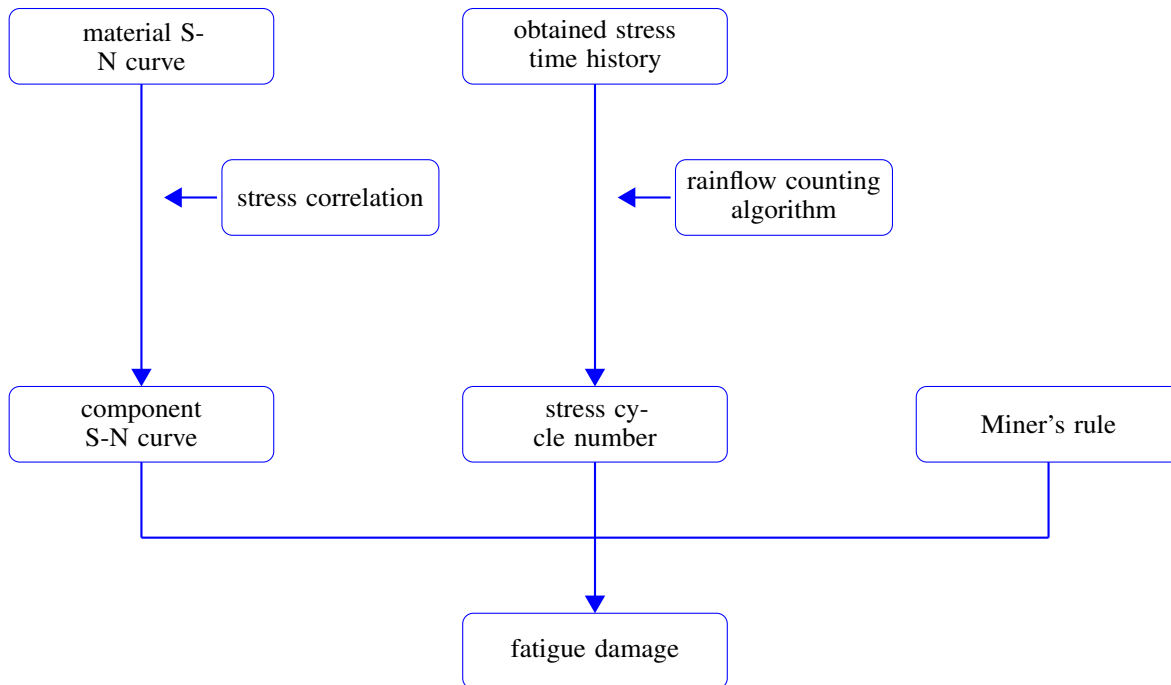


Figure 1.3: Deterministic fatigue analysis procedures

1.3 Random vibration fatigue analysis

For a deterministic fatigue loading, the fatigue analysis is ideally suited to the time domain. However, the fatigue analysis in the time domain would often require extensive time records to obtain an accurate analysis for a random loading, so the analysis process is always time-consuming. In reality, most real fatigue loads are unexpected. And for the case of a random loading signal, there are several advantages for a fatigue analysis in the frequency domain rather than the time domain. The main advantage is that the fatigue damage calculation is time-efficient [36].

1.3.1 Gaussian and stationary random process

When random loading is considered, the damage and fatigue life are random variables. The random process $\sigma(t)$ corresponds to a random variation in time of a stress component or effective stress. At each instant $t_i, i = 1, 2, \dots, n$, the process is composed of a number of random variables $\sigma(t_i)$ that follow a Gaussian distribution.

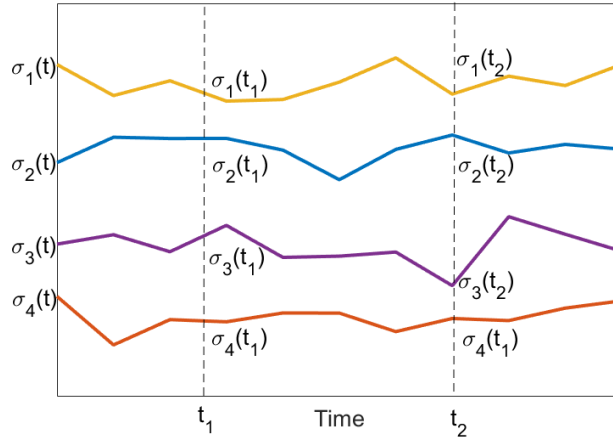


Figure 1.4: Schematic illustration of a random process

If the time t is continuous, the process is termed as a continuous-time random process. Similarly, if t is discrete, the process is called a discrete-time random process. Over a duration of observation T , the probability that a random process $\sigma(t)$ does not exceed, in absolute value, a given value denoted by r can be given by the cumulative distribution function (CDF) of the amplitudes (or maxima for zero-mean stress) denoted by $F_\sigma(r)$:

$$F_\sigma(r) = \int_{-\infty}^r p_\sigma(r) dr = \text{prob}(|\sigma(t)| \leq r), t \in [0, T] \quad (1.12)$$

where $p_\sigma(r)$ is the probability density function (PDF).

The m th order statistical moments of the continuous random variable $\sigma(t_i)$ is obtained from the expected value operator:

$$E[\sigma(t)^m] = \int_{-\infty}^{+\infty} r^m p_\sigma(r) dr \quad (1.13)$$

$m = 1$ corresponds to the expected value and $m = 2$ gives the second moment or variance for the zero mean.

The random variables are completely characterized by their statistical properties and more precisely by the CDF of each variable such as:

$$F_{\sigma(t_1), \dots, \sigma(t_n)}(r_1, \dots, r_n) = \text{prob}(\sigma(t_1) \leq r_1, \sigma(t_2) \leq r_2, \dots, \sigma(t_n) \leq r_n) \quad (1.14)$$

where $0 < t_1 < t_2 < \dots < t_n$.

The autocorrelation function measures the similarity between two different observation times t_1 and t_2 at the random process $\sigma(t)$, defined as:

$$R_{\sigma\sigma}(t_1, t_2) = E[\sigma(t_1)\sigma(t_2)] \quad (1.15)$$

A stationary random process can be categorized into a strict or wide sense counterpart based on its statistical properties. If its CDF, given in Eq. (1.14) is invariant to a time shift τ , the random process can be defined as a strict sense stationary (SSS) random process:

$$F_{\sigma(t_1), \dots, \sigma(t_n)}(r_1, r_2, \dots, r_n) = F_{\sigma(t_1-\tau), \dots, \sigma(t_n-\tau)}(r_1, r_2, \dots, r_n) \quad (1.16)$$

The random process is a wide sense stationary (WSS) random process if its moments and autocorrelation functions do not depend on absolute time, such as :

$$E[\sigma(t_1)^m] = E[\sigma(t_2)^m] = \dots = E[\sigma(t_n)^m] = E[\sigma(t)^m] \quad (1.17)$$

and,

$$R_{\sigma\sigma}(t, t - \tau) = R_{\sigma\sigma}(\tau) \quad (1.18)$$

Note, the autocorrelation function reaches his maximum for $\tau = 0$. In this case $R_{\sigma\sigma}(0) = E[\sigma(t)^2]$.

In addition, a random process is ergodic if the time average of the sample function and the statistical average are equals:

$$E[\sigma(t)] = \lim_{T \rightarrow \infty} \frac{1}{2T} \int_{-T}^{+T} \sigma(t) dt \quad (1.19)$$

and the time autocorrelation is identical to the statistical autocorrelation:

$$R_{\sigma\sigma}(\tau) = \lim_{T \rightarrow \infty} \frac{1}{2T} \int_{-T}^{+T} \sigma(t)\sigma(t - \tau) dt \quad (1.20)$$

1.3.2 Fatigue analysis induced by random acceleration

The study of the dynamic response exploiting vibration phenomena aimed to determine the dynamic properties which are directly connected to the geometrical and mechanical characteristics of a system. Hence, some concepts of structural dynamic response and how to obtain the dynamic parameters will be summarized in this section. The excitation with base motion (e.g., car suspension, earthquake ground motion or electrodynamic shaker, etc.) does not provide the force

applied information. Therefore the formalism related to the base motion is different from the classical force-excitation theory.

For random vibration loading, the global matrices \mathbf{M} , \mathbf{C} and \mathbf{K} (and mode shapes) given in Eq.(A.6) remain deterministic. In time domain, the force and displacement field are written in terms of expected values denoted, respectively, $E[\mathbf{F}(t)]$ and $E[\mathbf{u}(t)]$. In spectral domain, these two quantities are connected by the following relation:

$$\mathbf{S}_{uu}(f) = |\mathbf{H}_{uF}(f)|^2 \mathbf{S}_{FF}(f) \quad (1.21)$$

$\mathbf{S}_{uu}(f)$ and $\mathbf{S}_{FF}(f)$ are the PSDs of control point displacement and external forces. $|\mathbf{H}_{uF}(f)|$ corresponds to the frequency response magnitude of the structure obtained from the ratio between the displacement and the force given in frequency domain. In time domain, the stress expected value of the structure can be, therefore, deduced from the force expected value by using the following expression:

$$E[\boldsymbol{\sigma}(t)] = \mathbb{C} \mathbf{B} \mathbf{K}^{-1} E[\mathbf{F}(t)] \quad (1.22)$$

$\mathbf{K}^{-1} = \mathbf{H}_{uF}(0)$ represents the static part. The transformation of Eq.(1.22) into the spectral domain leads to a relationship between the stress and displacement PSDs:

$$\mathbf{S}_{\sigma\sigma}(f) = \mathbb{C} \mathbf{B} \mathbf{S}_{uu}(f) \mathbf{B}^T \mathbb{C}^T \quad (1.23)$$

1.3.3 Cumulative fatigue and frequency formulation for random excitation

To work in the frequency domain, it is necessary to make certain assumptions on a random excitation to ensure its stability. Firstly, a random signal should be stationary, meaning the statistical properties, including expected value, variance do not change with time. Secondly, it should be ergodic to ensure that an arbitrary sample of the excitation can be applied to substitute for the whole sample. Thus, the Fourier transform applied on the autocorrelation function $R_{\sigma\sigma}(\tau)$ to obtain the power spectral density (PSD) defined by:

$$S_{\sigma\sigma}(f) = \int_{-\infty}^{+\infty} R_{\sigma\sigma}(\tau) \exp(-j2\pi f\tau) d\tau \quad (1.24)$$

When a Gaussian stationary random process is considered, these parameters are mainly the k th order spectral moments given by:

$$m_k = \int_0^{+\infty} |2\pi f|^k S_{\sigma\sigma}(f) df \quad (1.25)$$

$S_{\sigma\sigma}(f)$ is the stress PSD function. When the mechanical structure is submitted to a zero-mean Gaussian stationary random excitation, the expected damage per unit time can be obtained from the cumulative expression given in Eq. (1.1):

$$E[D] = C^{-1} E[|\sigma(t)|^\beta] E[N] \quad (1.26)$$

where C and β are deterministic. To determine the expected value of $|\sigma(t)|^\beta$, we can use the expectation definition of random variable in HCF domain such as:

$$E[|\sigma(t)|^\beta] = \int_0^{+\infty} r^\beta p_\sigma(r) dr \quad (1.27)$$

it corresponds to β th order statistical moment.

Knowing that for period T , $E[N] = T \times E[N_0^+]$, so Eq. (1.26) becomes:

$$E[D] = C^{-1} T E[N_0^+] \int_0^{+\infty} r^\beta p_\sigma(r) dr \quad (1.28)$$

$E[N_0^+] = \sqrt{\frac{m_2}{m_0}}$ is the expected number of zero-crossings with positive slope per second. m_0 and m_2 are respectively the zeroth-order and second-order spectral moments of the PSD. $\sqrt{m_0}$ is the root mean square (RMS) and represents the square root of the area under the PSD-frequency graph. The expected fatigue life denoted $E[T_f]$ can be then deduced from Eq. (1.28):

$$E[T_f] = \frac{T}{E[D]} = \frac{1}{C^{-1} E[N_0^+] \int_0^{+\infty} r^\beta p_\sigma(r) dr} \quad (1.29)$$

Before the damage evaluation, it is necessary to define a probability density function $p_\sigma(r)$ of the maxima. The different spectral methods for fatigue damage assessment were first characterized by the cycle counting procedure. Since the Rainflow method has been recognized to give the best predictions, the spectral methods were mainly focused on the Rainflow cycle distribution. There is no analytical formula to establish the cycle distribution, therefore the existing spectral methods evaluate these distributions approximately or empirically. Some of the most commonly used methods

include the narrowband approach based on Rayleigh approximation, Dirlik's amplitude distribution [37]. In this work, Dirlik's distribution is used to evaluate the expected value of damage from Eqs. (1.28) and (1.29).

1.3.4 Fatigue analysis under different probability density functions

A signal can be classified into the narrow-band (NB) or wide-band (WB), based on the bandwidth value (the difference between the upper and lower frequencies). The NB refers to the signal, whose maximum bandwidth is 3400 Hz, as illustrated by the solid line in Fig. 1.5. The WB is the combination of NB and upper-band (UB) and has the bandwidth of 50-7000 Hz, defined by the international telecommunication union (ITU) [38].

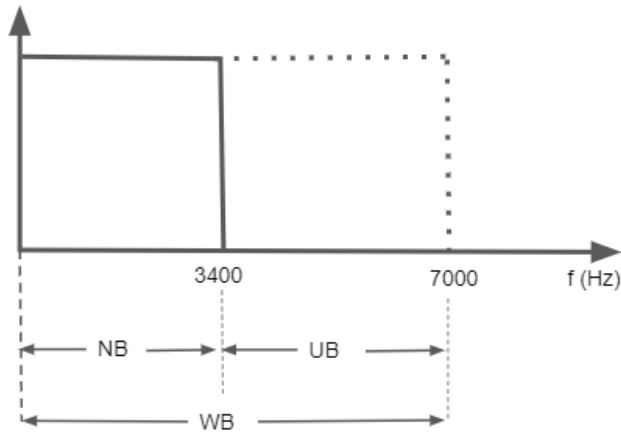


Figure 1.5: Bandwidth definition

During random fatigue damage calculation, it is necessary to identify the band character from obtained PSD (narrow or wide bands), which can be decided by the irregularity factor γ deduced from the expected number of zero-crossings $E[N_0^+]$ and peaks $E[P]$ per second, as shown in Eq. (1.30). The irregularity factor varies from 0 to 1. As it approaches 1, the random stress signal is close to NB. It comes 0, the stress signal approaches WB.

$$\gamma = \frac{E[N_0^+]}{E[P]} = \sqrt{\frac{m_2^2}{m_0 \cdot m_4}} \quad (1.30)$$

In 1964, Bendat [39] firstly provided the frequency domain fatigue damage calculation through the definition of the PDF function, as shown in Eq. (1.31). But the damage values from Bendat's equation give conservative results for Wide-Band application. Therefore, Bendat's solution is also termed a narrow-band solution.

$$p_{\sigma_B}(r) = \frac{r}{4m_0} \exp\left(\frac{-r^2}{8m_0}\right) \quad (1.31)$$

$$E[D]_{NB} = \frac{E[N_0^+]T}{C} \int_0^{+\infty} r^\beta \frac{r}{4m_0} \exp\left(\frac{-r^2}{8m_0}\right) dr \quad (1.32)$$

To solve this problem, the conservative results for wide-band application, Wirsching [40] firstly proposed the expression for wide-band solution based on Bendat's, as shown in Eq. (1.33).

$$E[D]_W = E[D]_{NB} (a + (1 - a)(1 - \varepsilon)^c) \quad (1.33)$$

where $E[D]_{NB}$ is the expected damage determined by the narrow band solution and $a = 0.926 - 0.033b$, $c = 1.587b - 2.323$, $\varepsilon = \sqrt{1 - \gamma^2}$.

In the field of narrow-band fatigue analysis, Tuna [41] and Dirlik [37] respectively proposed the new PDF. Tuna's PDF is defined by:

$$p_{\sigma_T}(r) = \frac{r}{4\gamma m_0} \exp\left(\frac{-r^2}{8\gamma m_0}\right) \quad (1.34)$$

Dirlik's PDF for a normalized variable $Z = \frac{\sigma_a}{\sqrt{m_0}}$ is:

$$p_{\sigma_D}(Z) = \frac{\frac{D_1}{Q} \exp\left(\frac{-Z}{Q}\right) + \frac{D_2 Z}{R^2} \exp\left(\frac{-Z^2}{2R^2}\right) + D_3 Q_S \exp\left(\frac{-Z^2}{2}\right)}{2\sqrt{m_0}} \quad (1.35)$$

with m_4 the fourth-order spectral moment of the PSD. x_m is defined by Dirlik as the mean frequency and is expressed such as:

$$x_m = \frac{m_1}{m_0} \sqrt{\frac{m_2}{m_4}} \quad (1.36)$$

and the other parameters are obtained from:

$$\begin{aligned} D_1 &= \frac{2(x_m - \gamma^2)}{1 + \gamma^2} & D_2 &= \frac{1 - \gamma - D_1 + D_1^2}{1 - R} & D_3 &= 1 - D_1 + D_2 \\ Q_S &= \frac{1.25(\gamma - D_3 - D_2)}{D_1} & R &= \frac{\gamma - x_m - D_1^2}{1 - \gamma - D_1 + D_1^2} \end{aligned}$$

The expected damage ratio can also be expressed in the form of equivalent stress, given by Eq. (1.37). Hancock [42] firstly gave the equivalent stress expression by the Eq. (1.38). Later Chaudhuri and Dover (C&D) [43] and Steinberg [44] respectively gave the expression also, as shown in Eqs. (1.39) and (1.40).

$$E[D] = \frac{E[N_0^+] T}{C} \sigma_{eq} \quad (1.37)$$

$$(\sigma_{eq})_{\text{Hancock}} = (2\sqrt{2m_0}) \left[\gamma \Gamma\left(\frac{\beta}{2} + 1\right) \right]^{\frac{1}{\beta}} \quad (1.38)$$

$$(\sigma_{eq})_{\text{C and D}} = (2\sqrt{2m_0}) \left[\frac{\epsilon^{\beta+2}}{2\sqrt{\pi i}} \Gamma\left(\frac{\beta}{2} + 1\right) + \frac{\gamma}{2} \Gamma\left(\frac{\beta}{2} + 2\right) + \text{erf}(\gamma) \frac{\gamma}{2} \Gamma\left(\frac{\beta}{2} + 2\right) \right]^{\frac{1}{\beta}} \quad (1.39)$$

$$(\sigma_{eq})_{\text{Steinberg}} = [0.683(2\sqrt{m_0})^\beta + 0.271(4\sqrt{m_0})^\beta + 0.043(6\sqrt{m_0})^\beta]^\frac{1}{\beta} \quad (1.40)$$

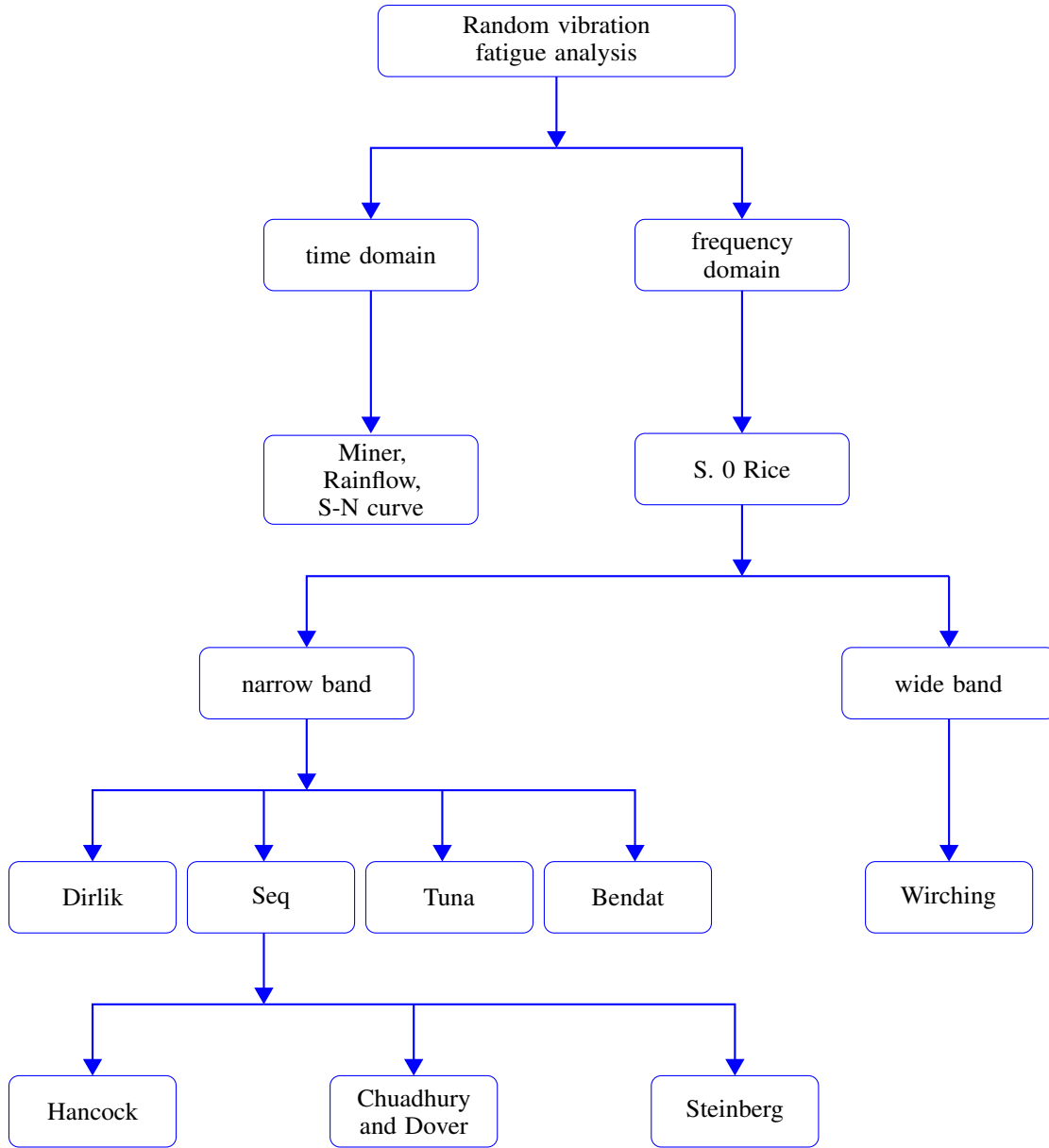


Figure 1.6: Vibration fatigue analysis procedures in the frequency domain

1.3.5 The random time signal generation from the corresponding PSD function

The time-series generation method from a given spectrum can be classified into deterministic or random amplitude scheme, in which the former is commonly applied [45]. Generally, the deterministic amplitude scheme has several procedures for generating random signals from the given PSD function. That are respectively 1) the selection of the frequencies f_i and random phase angles φ_i from the PSD function; 2) evaluation of the deterministic amplitudes: $A_i = \sqrt{2G_i \times \Delta f_i}$, where Δf_i is the frequency bandwidth; 3) summation for each time t : $Y(t) = \sum_i^n A_i \sin(2\pi f_i t + \varphi_i)$.

1.3.6 Equivalent stress for random loading

In triaxial stress state, the von Mises stress σ_c is given as:

$$\sigma_c = \sqrt{\frac{1}{2}[(\sigma_1 - \sigma_2)^2 + (\sigma_2 - \sigma_3)^2 + (\sigma_3 - \sigma_1)^2 + 6(\sigma_{12}^2 + \sigma_{23}^2 + \sigma_{31}^2)]} \quad (1.41)$$

where $\sigma_1, \sigma_2, \sigma_3$ and $\sigma_{12}, \sigma_{23}, \sigma_{31}$ are respectively normal and shear stresses. Defining the stress vector as $\sigma = (\sigma_1, \sigma_2, \sigma_3, \sigma_{12}, \sigma_{23}, \sigma_{31})^T$, Eq. (1.41) can be written as:

$$\sigma_c^2 = \sigma^T Q \sigma = \text{Trace} Q [\sigma \sigma^T] \quad (1.42)$$

where:

$$Q = \begin{bmatrix} 1 & -\frac{1}{2} & -\frac{1}{2} & 0 & 0 & 0 \\ -\frac{1}{2} & 1 & -\frac{1}{2} & 0 & 0 & 0 \\ -\frac{1}{2} & -\frac{1}{2} & 1 & 0 & 0 & 0 \\ 0 & 0 & 0 & 3 & 0 & 0 \\ 0 & 0 & 0 & 0 & 3 & 0 \\ 0 & 0 & 0 & 0 & 0 & 3 \end{bmatrix} \quad (1.43)$$

In recent decades, multiaxial fatigue damage models were defined in the stress, strain, or energy time histories [46]. However, these methods are often time-consuming for a finely discretized structure, as they often require complete stress-strain time histories. 1996, Pitoiset et al. [4] proposed a frequency domain fatigue analysis method for multiaxial stress states based on the definition of equivalent von Mises stress (an equivalent uniaxial stress PSD).

Take the expectation on Eq. (1.42):

$$E[\sigma_c^2] = \text{Trace}\{QE[\sigma \sigma^T]\} \quad (1.44)$$

where $E[\sigma \sigma^T]$ is the covariance matrix of the stress vector σ , which is related to the PSD $\Phi_{\sigma\sigma}(\omega)$ of the stress vector:

$$E[\sigma \sigma^T] = \int_{-\infty}^{+\infty} \Phi_{\sigma\sigma}(\omega) d\omega \quad (1.45)$$

where $\Phi_{\sigma\sigma}$ characterizes a zero mean Gaussian random stress field.

Thus, combine the Eqs. (1.44) and (1.45), obtain:

$$E[\sigma_c^2] = \int_{-\infty}^{+\infty} \text{Trace}\{Q\Phi_{\sigma\sigma}(\omega)\}d\omega \quad (1.46)$$

$E[\sigma_c^2]$ also equals to:

$$E[\sigma_c^2] = \int_{-\infty}^{+\infty} \Phi_c(\omega)d\omega \quad (1.47)$$

Combining the Eqs. (1.46) and (1.47), obtain the PSD $\Phi_c(\omega)$ of equivalent von Mises stress as:

$$\Phi_c(\omega) = \text{Trace}\{Q\Phi_{\sigma\sigma}(\omega)\} \quad (1.48)$$

1.4 Conclusion

In this chapter, the fatigue analysis backgrounds were described in the introduction. Then deterministic fatigue analysis theories, such as the explanations in Miner's rule, S-N curves were presented in Section 1.2. The dynamic fatigue analysis theories, including the definition of the random process and formulations in the frequency domain damage calculation, were given in Section 1.3, and based on these theories, the random vibration fatigue analysis will be developed on different models in chapter 3. In the chapter 2, I will present the theoretical backgrounds of the IGA approach and perform IGA on a simple plate model.

Chapter 2

Isogeometric Analysis Approach

2.1 Introduction

Isogeometric Analysis (IGA) proposed by T.J.R Hughes et al. [3] is a relatively new numerical analysis method, which integrates Computer-Aided Design (CAD) and Computer-Aided Engineering (CAE) to save the time spent in mesh generation, and also to obtain more precise analysis results, through exact geometric representation and direct utilization of CAD-based NURBS described geometric information.

Numerical modelling of a complex structure is a time-consuming aspect. Nowadays, mechanical systems are an assembly of many components, leading to specific requirements on numerical analysis methods in terms of accuracy and speed of analysis. Conventional FEA has some weaknesses. The time spent in the mesh generation process is often much longer than analysis time [2]. It is estimated that 80% of analysis time is devoted to the mesh generation in some fields, such as automotive or shipbuilding industries [3]. On the other hand, it is often necessary to communicate with the original geometry during each mesh refinement, and this process is time-consuming. The second disadvantage lies in geometric approximation. Indeed, it is challenging to accurately represent complex geometric models based on the Lagrangian basis function in classical FEA. Thus, the approximate models would result in inaccurate analysis results. A possible alternative to finite elements is IGA, often based on non-uniform rational B-splines (NURBS) basis functions.

This chapter mainly introduces the IGA approach regarding theoretical backgrounds and applications on a simple plate model. As shown in Fig. 2.1, in Section 2.2, the isogeometric theoretical backgrounds are presented. The present research state in IGA is reviewed in Section 2.3 through the discussion of the isogeometric algorithm, shape optimization, shell and vibration analysis. In Section 2.4, the differences between IGA and FEA are described. The

IGA and FEA are developed on a simple plate model in Section 2.5, in which the convergence analysis is carried on with the criterion of maximum stress, and the results are validated by the analytical solution.

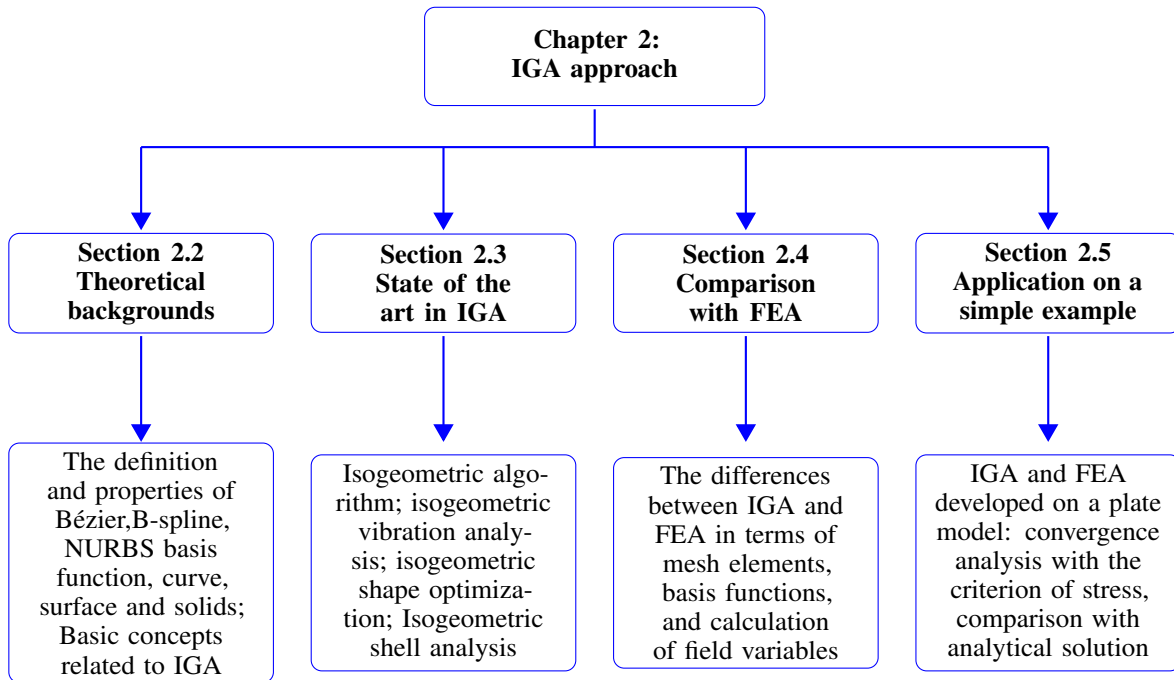


Figure 2.1: Schematic illustration of the second section

2.2 Theoretical background

2.2.1 Bézier, B-spline, NURBS

- I) Bézier curve, surface, and solid

A Bézier curve $C(\xi)$ ($\xi \in [0, 1]$) has been widely employed in practical engineering including mechanical design and computer graphics [47, 48]. It is a parametric curve defined by Bernstein polynomials and control points. A Bézier surface $C(\xi, \eta)$ ($\xi \in [0, 1], \eta \in [0, 1]$) and solid $C(\xi, \eta, \zeta)$ ($\xi \in [0, 1], \eta \in [0, 1], \zeta \in [0, 1]$) are respectively defined by the bivariate and trivariate Bernstein polynomials and control points.

1) Bernstein basis function

A p th degree Bernstein polynomial $B_{i,p}(\xi)$ is defined as:

$$B_{i,p}(\xi) = C_p^i \xi^i (1 - \xi)^{p-i} \quad \xi \in [0, 1] \quad (2.1)$$

where p is the polynomial order in ξ parametric direction, C_p^i is the i th binomial coefficient and expressed by:

$$C_p^i = \frac{p!}{i!(p-i)!} \quad (2.2)$$

Considering polynomial order $p = 4$, the formulation process of the Bernstein basis function would be presented following. Beginning with $i = 0$, obtain:

$$B_{0,4}(\xi) = C_4^0 \xi^0 (1-\xi)^4 = (1-\xi)^4 \quad (2.3)$$

$i = 1$, obtain

$$B_{1,4}(\xi) = C_4^1 \xi^1 (1-\xi)^3 = 4\xi(1-\xi)^3 \quad (2.4)$$

$i = 2$, obtain

$$B_{2,4}(\xi) = C_4^2 \xi^2 (1-\xi)^2 = 6\xi^2(1-\xi)^2 \quad (2.5)$$

$i = 3$, obtain

$$B_{3,4}(\xi) = C_4^3 \xi^3 (1-\xi)^1 = 4\xi^3(1-\xi) \quad (2.6)$$

$i = 4$, obtain

$$B_{4,4}(\xi) = C_4^4 \xi^4 (1-\xi)^0 = \xi^4 \quad (2.7)$$

Based on obtained Eqs. from 2.3 to 2.7, the corresponding basis functions can be constructed in Matlab, as shown in Fig. 2.2.

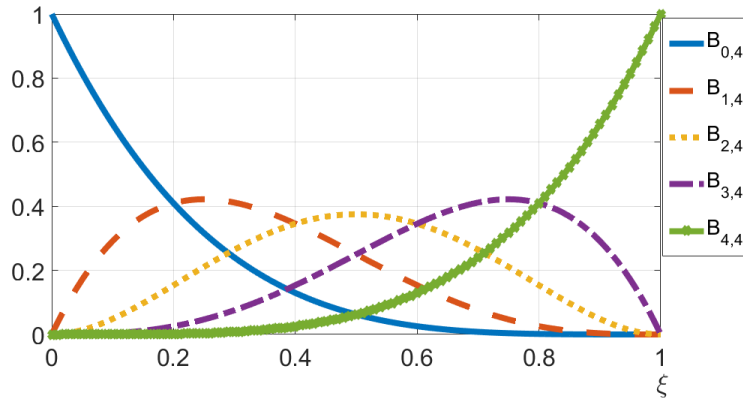


Figure 2.2: Bernstein basis functions

The important properties of Bernstein basis functions can be concluded as:

- (1) partition of unity $\xi \in [0, 1]$, $\sum_{i=1}^{p+1} B_{i,p}(\xi) = 1$
- (2) non negative $\xi \in [0, 1]$, $B_{i,p}(\xi) \geq 0$,
- (3) kronecker's delta $B_{i,p}(\xi_j) = \delta_{ij}$ which is satisfied at element boundary.
- (4) linear independence $\sum_{i=1}^{p+1} \alpha_i B_{i,p} = 0$, if $\alpha_1 = \alpha_2 = \dots = \alpha_n = 0$
- (5) satisfy variation diminishing property, which leads to Bézier curves behaving monotonous with the increase of

polynomial orders of basis functions.

(6) C^0 inter element continuity.

2) Bézier curve

The general form of a p degree Bézier curve $C(\xi)$, which requires $p + 1$ number of control point is expressed as:

$$C(\xi) = \sum_{i=1}^{p+1} B_{i,p}(\xi) \mathbf{P}_i, \quad \xi \in [0, 1], \quad (2.8)$$

where $\mathbf{P}_i = (x_i, y_i, z_i)^T$ ($i = 1, \dots, p + 1$) is the i th control point vector. As shown in Fig. 2.3, the polynomial order of 4 Bézier curve is defined by 5 control points, which begins at control point \mathbf{P}_1 and ends at \mathbf{P}_5 .

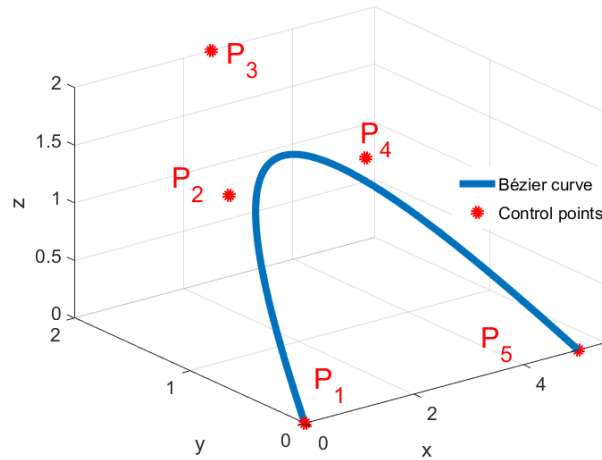


Figure 2.3: Bézier curve

3) Bézier surface and solid

A Bézier surface $C(\xi, \eta)$ is defined by the parametric Eq. (2.9),

$$C(\xi, \eta) = \sum_{i=1}^{p+1} \sum_{j=1}^{q+1} B_{i,p}(\xi) B_{j,q}(\eta) \mathbf{P}_{i,j} \quad (2.9)$$

A simplified form of Eq. 2.9 can be written as:

$$C(\xi, \eta) = \sum_{i=1}^{p+1} \sum_{j=1}^{q+1} B_{i,j}^{p,q} \mathbf{P}_{i,j} \quad (2.10)$$

A Bézier solid can be defined as:

$$C(\xi, \eta, \zeta) = \sum_{i=1}^{p+1} \sum_{j=1}^{q+1} \sum_{k=1}^{z+1} B_{i,p}(\xi) B_{j,q}(\eta) B_{k,z}(\zeta) \mathbf{P}_{i,j,k} \quad (2.11)$$

Similarly, a simplified form of Eq. (2.11) can be written as:

$$C(\xi, \eta, \zeta) = \sum_{i=1}^{p+1} \sum_{j=1}^{q+1} \sum_{k=1}^{z+1} B_{i,j,k}^{p,q,z} \mathbf{P}_{i,j,k} \quad (2.12)$$

where ξ, η, ζ are the parameters defined in the range $[0, 1]$, p, q, z represent the polynomial orders in ξ, η, ζ parametric directions, $\mathbf{P}_{i,j}$ and $\mathbf{P}_{i,j,k}$ are control point net and control point volume arrays, respectively.

According to Eq. (2.9), a Bézier surface can be constructed in Matlab, as shown in Fig. 2.4, in which the polynomial order in x and y directions are respectively 1 and 2.

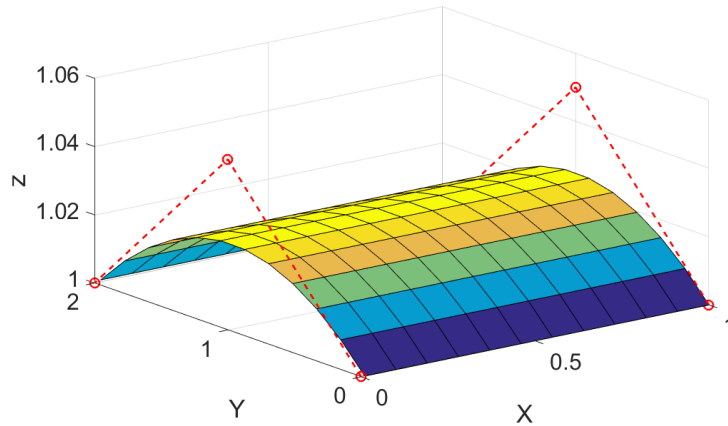


Figure 2.4: Bézier surface

- II) B-spline curve, surface and solids

The main innovation of the B-spline basis functions comparing to Bernstein polynomial is in the knot vector, a set of coordinates defined in parametric space. In univariate Bernstein polynomial, we use the parameter ξ generally in the range $[0, 1]$ to determine the basis function. In the B-spline basis function, however, we use a knot vector.

1) Knot vector

A knot vector in one dimension is defined as a series of non-decreasing coordinates in parametric space, denoted by $\Xi = \{\xi_1, \xi_2, \dots, \xi_{n+p+1}\}$, where $\xi_i \in R$ is the i th knot (or coordinate), and i is the knot index from $1, 2, \dots, n+p+1$, in which n is the number of B-spline basis function along ξ parametric direction, and p is the polynomial order of B-spline basis function. In constructing B-spline surface and solid, it is necessary to use 2 and 3-knot vectors respectively directed along ξ and η directions. Each knot or coordinate of the knot vector is used to divide the parametric space of a geometrical model to obtain elements. Thus all of the mesh elements can be selected by knot values of knot vectors.

In terms of the space between different knots, a knot vector can be a uniform or non-uniform knot vector. In a uniform knot vector, the knots are equally spaced in the parametric space, such as $\Xi = \{0.1, 0.2, 0.3, \dots, \xi_{n+p+1}\}$. Similarly, in a non-uniform knot vector, the knots are unequally spaced in the parametric space, such as $\Xi = \{0.1, 0.15, 0.25, 0.3, \dots, \xi_{n+p+1}\}$. In a knot vector, there can be repeated knots, and a knot vector is said to be open if its first and last knots repetition are equal to the $p + 1$, in which p is the polynomial order of the basis function. In one dimension, the basis functions constructed by an open knot vector interpolate the ends of parametric space. For example, in the following case, the knot vector and polynomial order are respectively $\Xi = \{0, 0, 0, 0.5, 1, 1, 1\}$ and 2. The polynomial order $p + 1$ is 3, which equals the number of first and last repeated knots, leading to the B-spline curve to interpolate the first and last control points, as shown in Fig. 2.8.

2) B-spline basis function

A B-spline basis function is defined by following Eqs. (2.13) and (2.14).

For polynomial order $p = 0$:

$$N_{i,0}(\xi) = \begin{cases} 1 & \text{if } \xi_i \leq \xi < \xi_{i+1} \\ 0 & \text{otherwise} \end{cases} \quad (2.13)$$

for $p > 1$:

$$N_{i,p}(\xi) = \frac{\xi - \xi_i}{\xi_{i+p} - \xi_i} N_{i,p-1}(\xi) + \frac{\xi_{i+p+1} - \xi}{\xi_{i+p+1} - \xi_{i+1}} N_{i+1,p-1}(\xi) \quad (2.14)$$

The building processes of B-spline basis functions corresponding to the knot vector $\Xi = \{0, 0, 0, 0.5, 1, 1, 1\}$ would be presented to explain the effects of the knot vector.

Starting with $i = 1$, polynomial order $p = 0$, obtain

$$N_{1,0}(\xi) = \begin{cases} 1 & \text{if } \xi_1 \leq \xi < \xi_2 \\ 0 & \text{otherwise} \end{cases} \quad (2.15)$$

as $\xi_1 = \xi_2 = \xi_3 = 0$, it can be observed that there is no value of ξ , such that $0 \leq \xi$ and $\xi < 0$, and therefore $N_{1,0}(\xi) = 0$.

Using the same logic to the remaining indices, the following piecewise constant functions can be obtained

$$N_{2,0}(\xi) = 0 \quad (2.16)$$

$$N_{3,0}(\xi) = \begin{cases} 1 & \text{if } 0 \leq \xi < 0.5 \\ 0 & \text{otherwise} \end{cases} \quad (2.17)$$

$$N_{4,0}(\xi) = \begin{cases} 1 & \text{if } 0.5 \leq \xi < 1 \\ 0 & \text{otherwise} \end{cases} \quad (2.18)$$

$$N_{5,0}(\xi) = 0 \quad (2.19)$$

$$N_{6,0}(\xi) = 0 \quad (2.20)$$

As shown in Fig. 2.5, based on Eqs. (2.15) to (2.20), the constant basis functions can be plotted in corresponding index space, in which it can be observed that function $N_{3,0}(\xi)$ and $N_{4,0}(\xi)$ are 1 in index space $0 \leq \xi < 0.5$ and $0.5 \leq \xi < 1$, respectively.

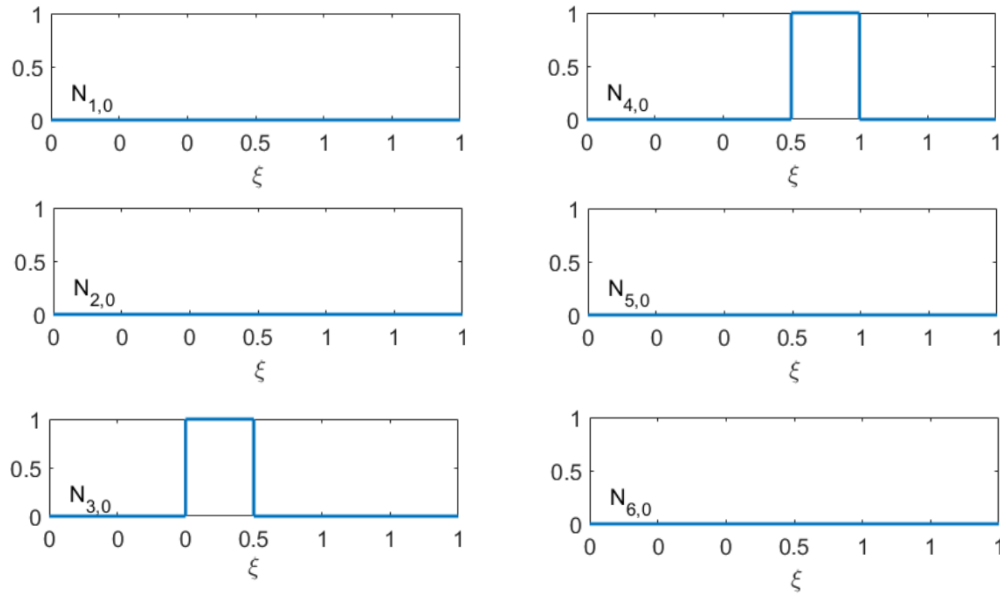


Figure 2.5: Constant basis functions corresponding to $\Xi = \{0, 0, 0, 0.5, 1, 1, 1\}$

Now, consider polynomial order $p = 1$. Beginning with $i = 1$, the following linear functions can be obtained

$$N_{1,1}(\xi) = \frac{\xi - 0}{0 - 0} N_{1,0}(\xi) + \frac{0 - \xi}{0 - 0} N_{2,0}(\xi) \quad (2.21)$$

as $N_{1,0}(\xi) = N_{2,0}(\xi) = 0$, obtain $N_{1,1}(\xi) = 0$.

when $i=2$, obtain

$$\begin{aligned} N_{2,1}(\xi) &= \frac{\xi - \xi_2}{\xi_3 - \xi_2} N_{2,0}(\xi) + \frac{\xi_4 - \xi}{\xi_4 - \xi_3} N_{3,0}(\xi) \\ &= \begin{cases} (1 - 2\xi) & \text{if } 0 \leq \xi < 0.5 \\ 0 & \text{otherwise} \end{cases} \end{aligned} \quad (2.22)$$

when $i=3$, obtain

$$\begin{aligned}
 N_{3,1}(\xi) &= \frac{\xi - \xi_3}{\xi_4 - \xi_3} N_{3,0}(\xi) + \frac{\xi_5 - \xi}{\xi_5 - \xi_4} N_{4,0}(\xi) \\
 &= 2\xi \begin{cases} 1 & \text{if } 0 \leq \xi < 0.5 \\ 0 & \text{otherwise} \end{cases} + 2(1 - \xi) \begin{cases} 1 & \text{if } 0.5 \leq \xi < 1 \\ 0 & \text{otherwise} \end{cases} \\
 &= \begin{cases} 2\xi & \text{if } 0 \leq \xi < 0.5 \\ 2(1 - \xi) & \text{if } 0.5 \leq \xi < 1 \\ 0 & \text{otherwise} \end{cases}
 \end{aligned} \tag{2.23}$$

when $i = 4$, obtain

$$\begin{aligned}
 N_{4,1}(\xi) &= \frac{\xi - \xi_4}{\xi_5 - \xi_4} N_{4,0}(\xi) + \frac{\xi_6 - \xi}{\xi_6 - \xi_5} N_{5,0}(\xi) \\
 &= \begin{cases} (2\xi - 1) & \text{if } 0.5 \leq \xi < 1 \\ 0 & \text{otherwise} \end{cases}
 \end{aligned} \tag{2.24}$$

when $i = 5$, obtain

$$N_{5,1}(\xi) = \frac{\xi - \xi_5}{\xi_6 - \xi_5} N_{5,0}(\xi) + \frac{\xi_7 - \xi}{\xi_7 - \xi_6} N_{6,0}(\xi) \tag{2.25}$$

similarly, as $N_{5,0}(\xi) = N_{6,0}(\xi) = 0$, obtain $N_{5,1}(\xi) = 0$.

Based on the obtained Eqs. (2.21) to (2.25), the corresponding basis functions can be constructed in Matlab, as shown in Fig. 2.6.

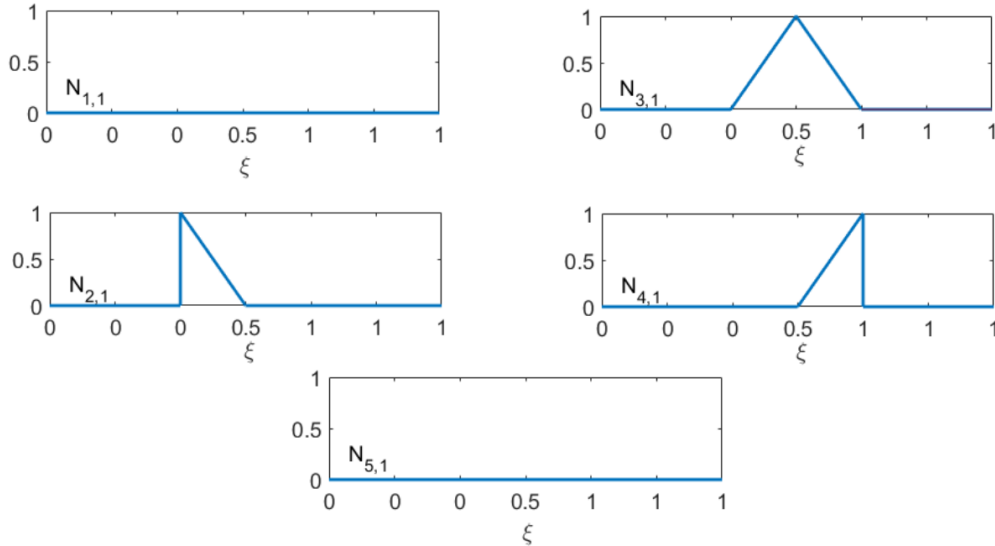


Figure 2.6: Linear basis functions corresponding to $\Xi = \{0, 0, 0, 0.5, 1, 1, 1\}$

Now, consider polynomial order $p = 2$. Beginning with $i = 1$, the following quadratic functions can be obtained

$$\begin{aligned}
N_{1,2}(\xi) &= \frac{\xi - \xi_1}{\xi_2 - \xi_1} N_{1,1}(\xi) + \frac{\xi_4 - \xi}{\xi_4 - \xi_2} N_{2,1}(\xi) \\
&= \begin{cases} \frac{\xi_4 - \xi}{\xi_4 - \xi_2} \frac{\xi_4 - \xi}{\xi_4 - \xi_3} & \text{if } 0 \leq \xi < 0.5 \\ 0 & \text{otherwise} \end{cases} \\
&= \begin{cases} 4(\frac{1}{2} - \xi)^2 & \text{if } 0 \leq \xi < 0.5 \\ 0 & \text{otherwise} \end{cases}
\end{aligned} \tag{2.26}$$

when $i = 2$, obtain

$$\begin{aligned}
N_{2,2}(\xi) &= \frac{\xi - \xi_2}{\xi_4 - \xi_2} N_{2,1}(\xi) + \frac{\xi_5 - \xi}{\xi_5 - \xi_3} N_{3,1}(\xi) \\
&= \begin{cases} \frac{\xi - \xi_2}{\xi_4 - \xi_2} \frac{\xi_4 - \xi}{\xi_4 - \xi_3} + \frac{\xi_5 - \xi}{\xi_5 - \xi_3} \frac{\xi - \xi_3}{\xi_4 - \xi_3} & \text{if } 0 \leq \xi < 0.5 \\ \frac{\xi_5 - \xi}{\xi_5 - \xi_3} \frac{\xi_5 - \xi}{\xi_5 - \xi_4} & \text{if } 0.5 \leq \xi < 1 \\ 0 & \text{otherwise} \end{cases} \\
&= \begin{cases} -6\xi^2 + 4\xi & \text{if } 0 \leq \xi < 0.5 \\ 2(1 - \xi)^2 & \text{if } 0.5 \leq \xi < 1 \\ 0 & \text{otherwise} \end{cases}
\end{aligned} \tag{2.27}$$

when $i = 3$, obtain

$$\begin{aligned}
N_{3,2}(\xi) &= \frac{\xi - \xi_3}{\xi_5 - \xi_3} N_{3,1}(\xi) + \frac{\xi_6 - \xi}{\xi_6 - \xi_4} N_{4,1}(\xi) \\
&= \begin{cases} \frac{\xi - \xi_3}{\xi_5 - \xi_3} \frac{\xi - \xi_3}{\xi_4 - \xi_3} & \text{if } 0 \leq \xi < 0.5 \\ \frac{\xi - \xi_3}{\xi_5 - \xi_3} \frac{\xi_5 - \xi}{\xi_5 - \xi_4} + \frac{\xi_6 - \xi}{\xi_6 - \xi_4} \frac{\xi - \xi_4}{\xi_5 - \xi_4} & \text{if } 0.5 \leq \xi < 1 \\ 0 & \text{otherwise} \end{cases} \\
&= \begin{cases} 2\xi^2 & \text{if } 0 \leq \xi < 0.5 \\ -6\xi^2 + 8\xi - 2 & \text{if } 0.5 \leq \xi < 1 \\ 0 & \text{otherwise} \end{cases}
\end{aligned} \tag{2.28}$$

when $i = 4$, obtain

$$\begin{aligned}
N_{4,2}(\xi) &= \frac{\xi - \xi_4}{\xi_6 - \xi_4} N_{4,1}(\xi) + \frac{\xi_7 - \xi}{\xi_7 - \xi_5} N_{5,1}(\xi) \\
&= \begin{cases} \frac{\xi - \xi_4}{\xi_6 - \xi_4} \frac{\xi - \xi_4}{\xi_5 - \xi_4} & \text{if } 0.5 \leq \xi < 1 \\ 0 & \text{otherwise} \end{cases} \\
&= \begin{cases} 4\xi^2 - 4\xi + 1 & \text{if } 0.5 \leq \xi < 1 \\ 0 & \text{otherwise} \end{cases}
\end{aligned} \tag{2.29}$$

Based on the obtained Eqs. (2.26) to (2.29), the corresponding basis functions can be constructed in Matlab, as shown in Fig. 2.7.

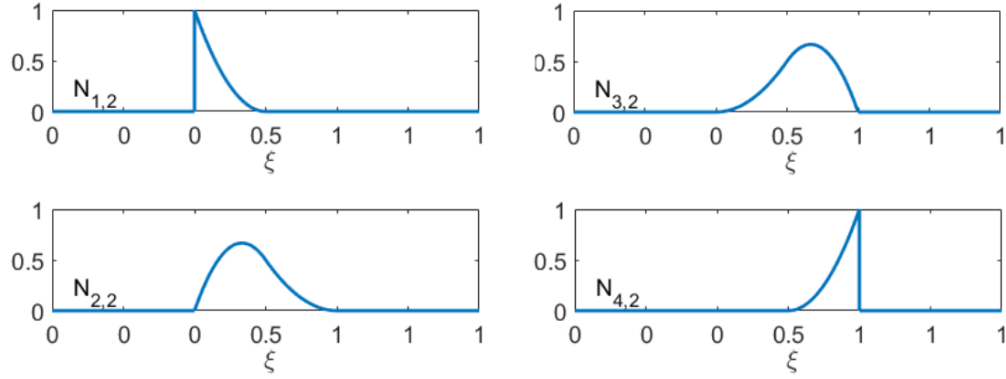


Figure 2.7: Quadratic basis functions corresponding to $\Xi = \{0, 0, 0, 0.5, 1, 1, 1\}$

Important properties of B-spline basis functions can be concluded as:

- (1) partition of unity $\forall \xi, \sum_{i=1}^n N_{i,p}(\xi) = 1$
- (2) non negative $\forall \xi, 0 \leq N_{i,p}(\xi)$
- (3) kronecker's delta $N_{i,p}(\xi_j) = \delta_{ij}$, which is satisfied at patch boundary.
- (4) linear independence $\sum_{i=1}^n \alpha_i N_{i,p} = 0$, if $\alpha_1 = \alpha_2 = \dots = \alpha_n = 0$
- (5) variation diminishing property, leading to B-spline curves behaving monotonous with the increase of polynomial orders of basis functions.
- (6) basis function continuity. p th order basis functions have $p - 1$ continuous derivative C^{p-1} across the knots, element boundaries, under the condition of no repeated knots. With repeated knots, the p th order basis functions would constitute $p - k - 1$ continuous derivatives C^{p-k-1} in which k is the multiplicity number of knots in a knot vector. For an open knot vector in which the multiplicity of the first and last knot is $p + 1$, the basis functions would possess C^0 continuity at the boundary of a patch.

3) B-spline curve

A B-spline curve is defined by the linear combination of B-spline basis function $N_{i,p}(\xi)$ and the corresponding control point $\mathbf{P}_i, i = 1, 2, \dots, n$, as shown in Eq. (2.30).

$$C(\xi) = \sum_{i=1}^n N_{i,p}(\xi) \mathbf{P}_i \quad (2.30)$$

Based on Eq. (2.30), a B-spline curve can be constructed in Matlab, as shown in Fig. 2.8, in which the polynomial order and number of control points are respectively 2 and 4.

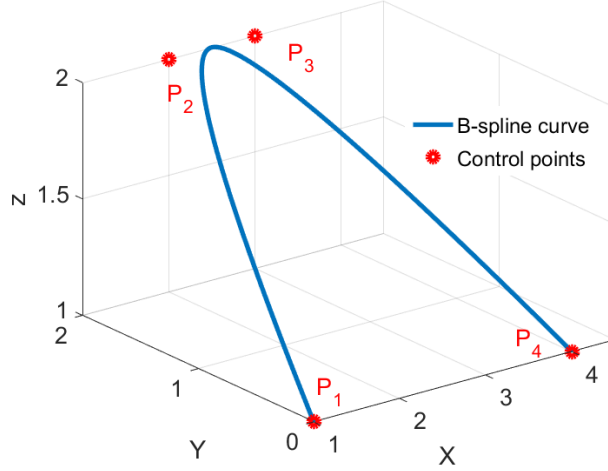


Figure 2.8: B-spline curve corresponding to the knot vector $\Xi = \{0, 0, 0, 0.5, 1, 1, 1\}$

4) B-spline surface, and solid

Given a control net $\mathbf{P}_{i,j}$, $i = 1, 2, \dots, n$, $j = 1, 2, \dots, m$, and knot vectors $\xi = \{\xi_1, \xi_2, \dots, \xi_{n+p+1}\}$, $\eta = \{\eta_1, \eta_2, \dots, \eta_{m+q+1}\}$, a B-spline surface is defined as:

$$C(\xi, \eta) = \sum_{i=1}^n \sum_{j=1}^m N_{i,p}(\xi) M_{j,q}(\eta) \mathbf{P}_{i,j} \quad (2.31)$$

where $N_{i,p}(\xi)$ and $M_{j,q}(\eta)$ are the p th and q th order B-spline basis functions, n and m are respectively number of basis functions in ξ and η parametric directions. A compact form of Eq. (2.31) can be written as:

$$C(\xi, \eta) = \sum_{i=1}^n \sum_{j=1}^m N_{i,j}^{p,q}(\xi, \eta) \mathbf{P}_{i,j} \quad (2.32)$$

For a control point volume array $\mathbf{P}_{i,j,k}$, $i = 1, 2, \dots, n$, $j = 1, 2, \dots, m$, $k = 1, 2, \dots, l$, a B-spline solid is defined as:

$$C(\xi, \eta, \zeta) = \sum_{i=1}^n \sum_{j=1}^m \sum_{k=1}^l N_{i,p}(\xi) M_{j,q}(\eta) R_{k,z}(\zeta) \mathbf{P}_{i,j,k} \quad (2.33)$$

where $R_{k,r}(\zeta)$ is r th order B-spline basis function, and l is the number of basis functions in ζ parametric direction. The simplified form of Eq. (2.33) can be written as:

$$C(\xi, \eta, \zeta) = \sum_{i=1}^n \sum_{j=1}^m \sum_{k=1}^l N_{i,j,k}^{p,q,z}(\xi, \eta, \zeta) \mathbf{P}_{i,j,k} \quad (2.34)$$

Based on Eq. (2.31), a B-spline surface can be constructed in Matlab, as shown in Fig. 2.9.

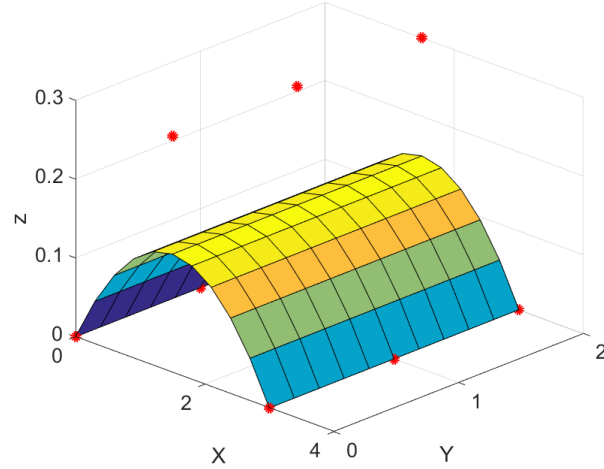


Figure 2.9: B-spline surface

where the polynomial order and number of basis functions along ξ and η parametric directions are respectively 2 and 3, and corresponding knot vectors are respectively $\xi = \eta = \{0, 0, 0, 1, 1, 1\}$.

- III) NURBS curve, surface, and volume

1) NURBS basis function

Univariate NURBS basis function is described by the rationale of weighted B-spline basis functions as:

$$R_{i,p}(\xi) = \frac{\omega_i N_{i,p}(\xi)}{W(\xi)} = \frac{\omega_i N_{i,p}(\xi)}{\sum_{i=1}^n \omega_i N_{i,p}(\xi)} \quad (2.35)$$

where ω_i denotes the weight value of the i th control point \mathbf{P}_i , and $W(\xi)$ is the weighted linear combination of B-spline basis functions.

The building procedure of the NURBS basis function with knot vector $\Xi = \{0, 0, 0, 0.5, 1, 1, 1\}$, and polynomial order $p = 0$ would be presented.

As the related equations of B-spline basis functions have been reviewed before, we only focus on the NURBS basis function.

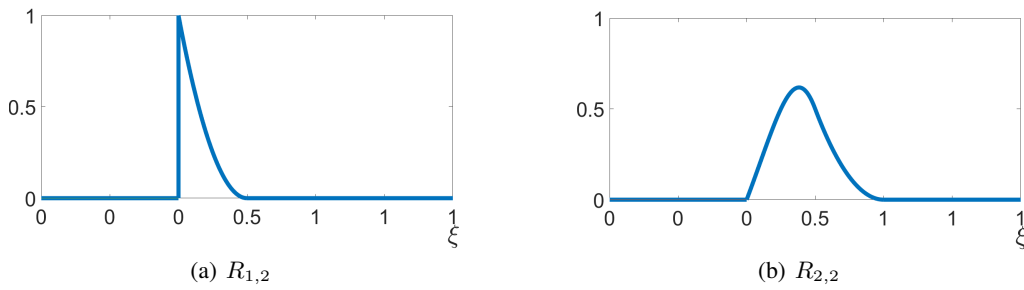
$$\begin{aligned} R_{1,2}(\xi) &= \frac{\omega_1 N_{1,2}(\xi)}{W(\xi)} = \frac{\omega_1 N_{1,2}(\xi)}{\sum_{i=1}^4 \omega_i N_{i,2}(\xi)} \\ &= \frac{\omega_1 N_{1,2}(\xi)}{\omega_1 N_{1,2}(\xi) + \omega_2 N_{2,2}(\xi) + \omega_3 N_{3,2}(\xi) + \omega_4 N_{4,2}(\xi)} \\ &= \begin{cases} 4\xi^2 - 4\xi + 1 & \text{if } 0 \leq \xi < 0.5 \\ 0 & \text{otherwise} \end{cases} \end{aligned} \quad (2.36)$$

$$\begin{aligned}
R_{2,2}(\xi) &= \frac{\omega_2 N_{2,2}(\xi)}{W(\xi)} = \frac{\omega_2 N_{2,2}(\xi)}{\sum_{i=1}^{n_4} \omega_i N_{i,2}} \\
&= \frac{\omega_2 N_{2,2}(\xi)}{\omega_1 N_{1,2}(\xi) + \omega_2 N_{2,2}(\xi) + \omega_3 N_{3,2}(\xi) + \omega_4 N_{4,2}(\xi)} \\
&= \begin{cases} \frac{-6\xi^2 + 4\xi}{4\xi^2 - 4\xi + 2} & \text{if } 0 \leq \xi < 0.5 \\ 2(1 - \xi)^2 & \text{if } 0.5 \leq \xi < 1 \\ 0 & \text{otherwise} \end{cases} \tag{2.37}
\end{aligned}$$

$$\begin{aligned}
R_{3,2}(\xi) &= \frac{\omega_3 N_{3,2}(\xi)}{W(\xi)} = \frac{\omega_3 N_{3,2}(\xi)}{\sum_{i=1}^{n_4} \omega_i N_{i,2}} \\
&= \frac{\omega_1 N_{1,2}(\xi)}{\omega_1 N_{1,2}(\xi) + \omega_2 N_{2,2}(\xi) + \omega_3 N_{3,2}(\xi) + \omega_4 N_{4,2}(\xi)} \\
&= \begin{cases} \frac{2\xi^2}{4\xi^2 - 4\xi + 2} & \text{if } 0 \leq \xi < 0.5 \\ (-6\xi^2 + 8\xi - 2) & \text{if } 0.5 \leq \xi < 1 \\ 0 & \text{otherwise} \end{cases} \tag{2.38}
\end{aligned}$$

$$\begin{aligned}
R_{4,2}(\xi) &= \frac{\omega_4 N_{4,2}(\xi)}{W(\xi)} = \frac{\omega_4 N_{4,2}(\xi)}{\sum_{i=1}^{n_4} \omega_i N_{i,2}} \\
&= \frac{\omega_1 N_{1,2}(\xi)}{\omega_1 N_{1,2}(\xi) + \omega_2 N_{2,2}(\xi) + \omega_3 N_{3,2}(\xi) + \omega_4 N_{4,2}(\xi)} \\
&= \begin{cases} 4\xi^2 - 4\xi + 1 & \text{if } 0.5 \leq \xi < 1 \\ 0 & \text{otherwise} \end{cases} \tag{2.39}
\end{aligned}$$

Based on obtained Eqs. from (2.36) to (2.39), the corresponding basis functions can be constructed in Matlab, as shown in Fig. 2.10.



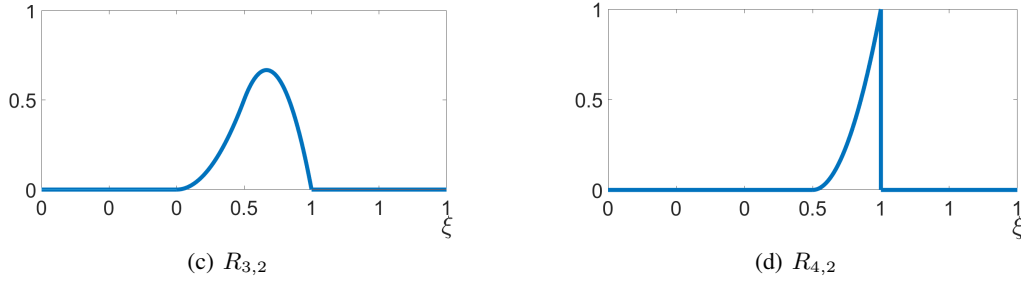


Figure 2.10: NURBS basis functions corresponding to $\Xi = \{0, 0, 0, 0.5, 1, 1, 1\}$

From the construction of NURBS basis functions, the following essential properties can be obtained:

- (1) a partition of unity $\forall \xi, \sum_{i=1}^n R_{i,p}(\xi) = 1$
- (2) non-negative $\forall \xi, 0 \leq R_{i,p}(\xi)$
- (3) kronecker's delta $R_{i,p}(\xi_j) = \delta_{ij}$ which is satisfied at patch boundary.
- (4) linear independence $\sum_{i=1}^n \alpha_i R_{i,p} = 0$, if $\alpha_1 = \alpha_2 = \dots = \alpha_n = 0$
- (5) variation diminishing property, leading to NURBS curves behaving monotonous with increased polynomial orders of basis functions.
- (6) basis function continuity. It can be seen that NURBS basis functions are the rationale of B-spline basis functions, which result in sharing some same properties with B-spline basis functions like basis functions continuity. At the same time, because of the combination of the weight values, the NURBS basis functions are more flexible than the B-spline basis functions. [3,49].

2) NURBS curve

NURBS curve is defined by the linear combination of univariate NURBS basis function $R_{i,p}(\xi)$ and control point \mathbf{P}_i by the following expression [3]:

$$C(\xi) = \sum_{i=1}^n R_{i,p}(\xi) \mathbf{P}_i \quad (2.40)$$

where the NURBS basis function $R_{i,p}(\xi)$ is defined by the Eq. (2.35), $\mathbf{P}_i = \{P_x, P_y, P_z\}$ is the i th control point vector.

Based on the Eq. (2.40), a NURBS curve can be constructed in Matlab, as shown in Fig. 2.11, in which the polynomial order, number of control points are respectively 2 and 4, and the corresponding knot vector and weight values are $\xi = \{0, 0, 0, 0.5, 1, 1, 1\}$ and $\omega = \{1, 1, 1, 1\}$.

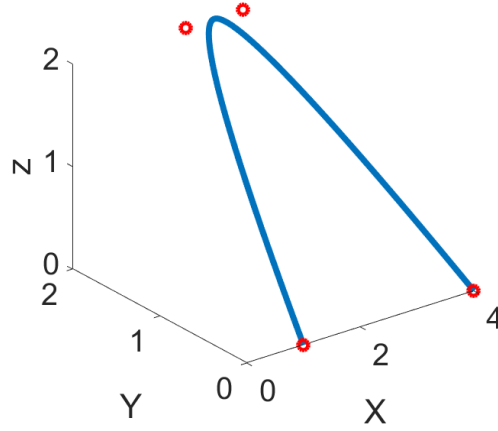


Figure 2.11: NURBS curve

3) NURBS surface, and solid

NURBS surfaces are defined as:

$$C(\xi, \eta) = \sum_{i=1}^n \sum_{j=1}^m \mathbf{R}_{i,j}^{p,q}(\xi, \eta) \mathbf{P}_{i,j} \quad (2.41)$$

where the bivariate NURBS basis function $R_{i,j}^{p,q}(\xi, \eta)$ is given as:

$$\mathbf{R}_{i,j}^{p,q}(\xi, \eta) = \frac{N_{i,p}(\xi)M_{j,q}(\eta)w_{i,j}}{\sum_{i=1}^n \sum_{j=1}^m N_{i,p}(\xi)M_{j,q}(\eta)w_{i,j}} \quad (2.42)$$

where $N_{i,p}(\xi)$ and $M_{j,q}(\eta)$ are respectively the p th and q th order B-spline basis function, which are defined by the Eqs. (2.21) and (2.27).

Similarly, NURBS solids are defined as

$$C(\xi, \eta, \zeta) = \sum_{i=1}^n \sum_{j=1}^m \sum_{k=1}^l \mathbf{R}_{i,j,k}^{p,q,z}(\xi, \eta, \zeta) \mathbf{P}_{i,j,k} \quad (2.43)$$

where the trivariate NURBS basis function $\mathbf{R}_{i,j,k}^{p,q,z}(\xi, \eta, \zeta)$ is given as

$$\mathbf{R}_{i,j,k}^{p,q,z}(\xi, \eta, \zeta) = \frac{N_{i,p}(\xi)M_{j,q}(\eta)R_{k,z}(\zeta)w_{i,j,k}}{\sum_{i=1}^n \sum_{j=1}^m \sum_{k=1}^l N_{i,p}(\xi)M_{j,q}(\eta)R_{k,z}(\zeta)w_{i,j,k}} \quad (2.44)$$

Based on Eq. (2.41), a NURBS surface can be constructed in Matlab, as shown in Fig. 2.12.

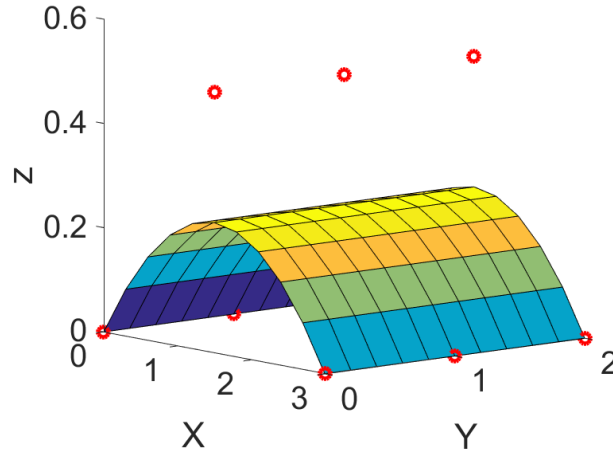


Figure 2.12: NURBS surface

where the polynomial order and number of basis functions along ξ and η parametric directions are respectively 2 and 3, and corresponding knot vectors are respectively $\xi = \eta = \{0, 0, 0, 1, 1, 1\}$.

2.2.2 Basic concepts related to IGA

In this part, some definitions of fundamental concepts related to IGA will be presented based on figures created in Ls Dyna and the paper of Agrawal [49].

- I) Definitions and transformation of different spaces

Index space in two dimensions is equally divided no matter with knot values of knot vectors. In this case, the knot vectors are respectively $\Xi_1 = \{0, 0, 0, 0.5, 1, 1, 1\}$ and $\Xi_2 = \{0, 0, 0, 0.5, 1, 1, 1\}$, in which the index space ranges from $[0, 1]$ (see Fig. 2.13 (a)). Parameter space in two dimensions is $[0, 1] \otimes [0, 1]$ domain where NURBS basis functions are defined (see Fig. 2.13 (b)). Control points, physical mesh, and control mesh are defined in physical space (see Fig. 2.13 (c)).

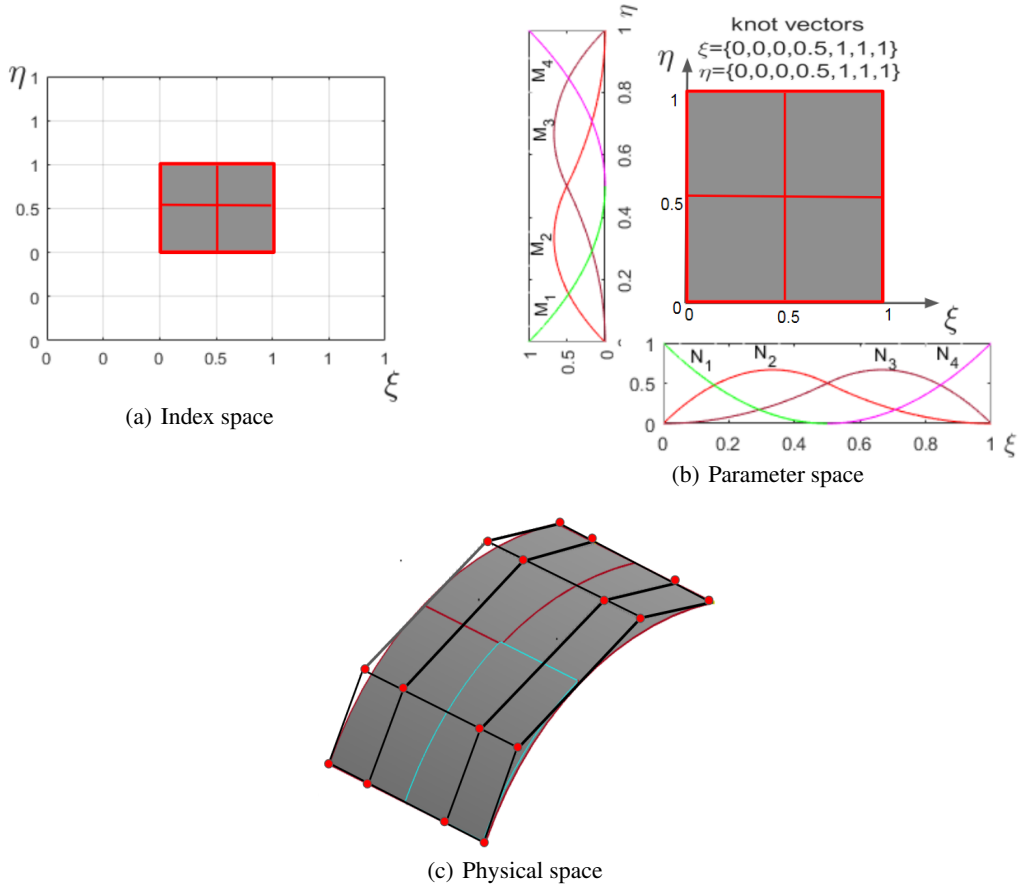


Figure 2.13: Schematic illustration of different spaces

Numerical integration like Gauss-Legendre is developed on parent domain $[-1, 1] \otimes [-1, 1]$, which is also called master space. As shown in Fig. 2.14, an element $\Omega^e = [x_i, x_{i+1}] \otimes [y_i, y_{i+1}]$ of physical space can be transformed to the element $\tilde{\Omega}^e = [\xi_i, \xi_{i+1}] \otimes [\eta_i, \eta_{i+1}]$ of parameter space and also the element $\bar{\Omega}^e = [-1, 1] \otimes [-1, 1]$ of parent domain through the calculation of Jacobian matrices, in which the NURBS basis functions and corresponding derivatives would be evaluated at ξ and η of element $\tilde{\Omega}^e$ in the parameter space, based on the equation 2.45.

$$\begin{aligned}\xi &= \frac{1}{2} [(\xi_{i+1} - \xi_i)\bar{\xi} + (\xi_{i+1} + \xi_i)] \\ \eta &= \frac{1}{2} [(\eta_{i+1} - \eta_i)\bar{\eta} + (\eta_{i+1} + \eta_i)]\end{aligned}\tag{2.45}$$

where $\bar{\xi}$ and $\bar{\eta}$ are the known integration points in the parent domain, which can be obtained based on the Gauss-Legendre quadrature rule.

In order to compute numerical integration, in the first step the mapping from the physical space to parameter space would be developed, based on Eq. (2.46) [49].

$$\mathbf{J}_1 = \begin{bmatrix} \frac{\partial x}{\partial \xi} & \frac{\partial x}{\partial \eta} \\ \frac{\partial y}{\partial \xi} & \frac{\partial y}{\partial \eta} \end{bmatrix} \quad (2.46)$$

where the components of \mathbf{J}_1 , can be calculated by Eqs. (2.47) and (2.48):

$$\frac{\partial x}{\partial \xi} = \sum_{k=1}^{n_{cp}^e} \frac{\partial R_k}{\partial \xi} x_i \quad (2.47)$$

$$\frac{\partial x}{\partial \eta} = \sum_{k=1}^{n_{cp}^e} \frac{\partial R_k}{\partial \eta} x_i \quad (2.48)$$

where n_{cp}^e is the number of control points in an element Ω^e .

In the second step, the mapping from parameter to master spaces can be obtained, based on Eq. (2.49) [49].

$$\mathbf{J}_2 = \frac{\partial \xi}{\partial \bar{\xi}} \frac{\partial \eta}{\partial \bar{\eta}} \quad (2.49)$$

The overall mapping processes can be explained by the following example where a random physical quantity $f(x, y)$ is computed over the physical space, and the Gauss integration is performed over the parent domain [49].

$$\begin{aligned} \int_{\Omega} f(x, y) d\Omega &= \sum_{e=1}^{nel} \int_{\Omega^e} f(x, y) d\Omega \\ &= \sum_{e=1}^{nel} \int_{\tilde{\Omega}^e} f(\xi, \eta) |J_1| d\xi d\eta, \quad (\tilde{\phi} : \Omega^e \rightarrow \tilde{\Omega}^e) \\ &= \sum_{e=1}^{nel} \int_{\bar{\Omega}^e} f(\bar{\xi}, \bar{\eta}) |J_1| |J_2| d\bar{\xi} d\bar{\eta}, \quad (\bar{\phi} : \tilde{\Omega}^e \rightarrow \bar{\Omega}^e) \\ &= \sum_{e=1}^{nel} \int_{-1}^1 \int_{-1}^1 f(\bar{\xi}, \bar{\eta}) |J_1| |J_2| d\bar{\xi} d\bar{\eta} \\ &= \sum_{e=1}^{nel} \left[\sum_{i=1}^{n_{gp}^e} f(\bar{\xi}_i, \bar{\eta}_i) \omega p_i |J_1| |J_2| \right] \end{aligned} \quad (2.50)$$

where n_{gp}^e and ωp_i are respectively the number of Gauss points and their weights in element $\bar{\Omega}^e$ of the parent domain.

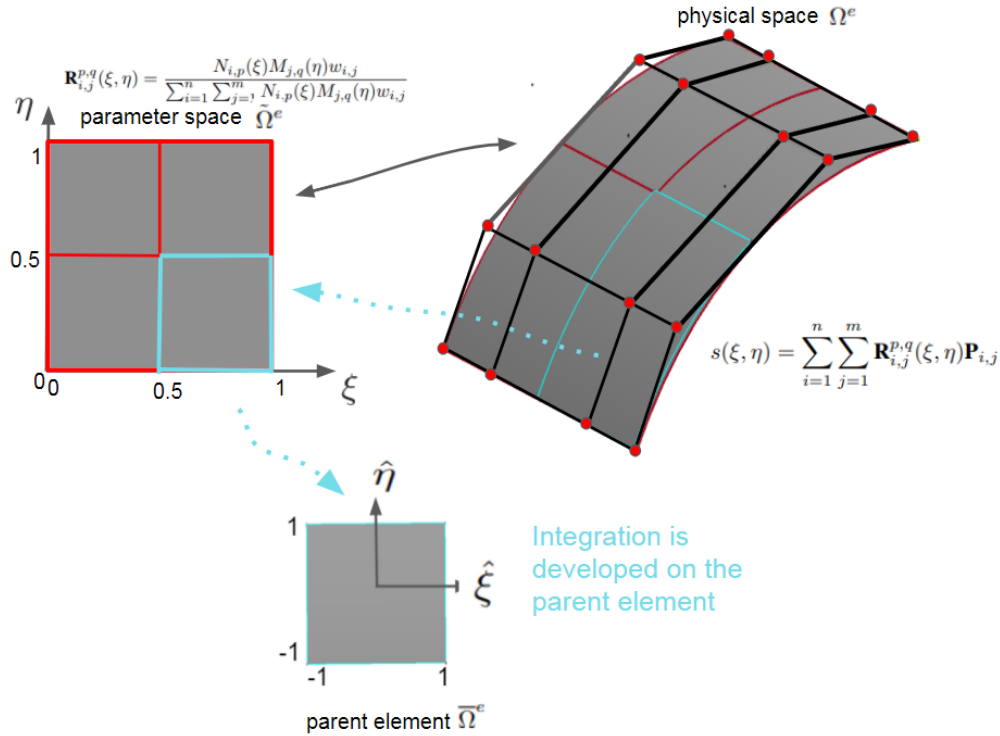


Figure 2.14: Schematic illustration of the space transformations

- II) patch, mesh model

A patch is termed a subdomain in IGA, in which the material properties and section information are defined to be the same. In IGA, a patch can be represented by numerous mesh elements. And a mesh model can be described by several patches, in which we can set different material properties or section details like thickness. The number of patches that a geometrical model needs is usually determined by its complexity. As shown in Fig. 2.15, model 1 is described by one patch, and model 2 is comprised of 2 patches.

In physical space of Fig. 2.16, there are two kinds of mesh models that are respectively control mesh and physical mesh. The control mesh is described by control points, and it controls an actual geometry model. The physical mesh is a real representation of an actual geometry model.

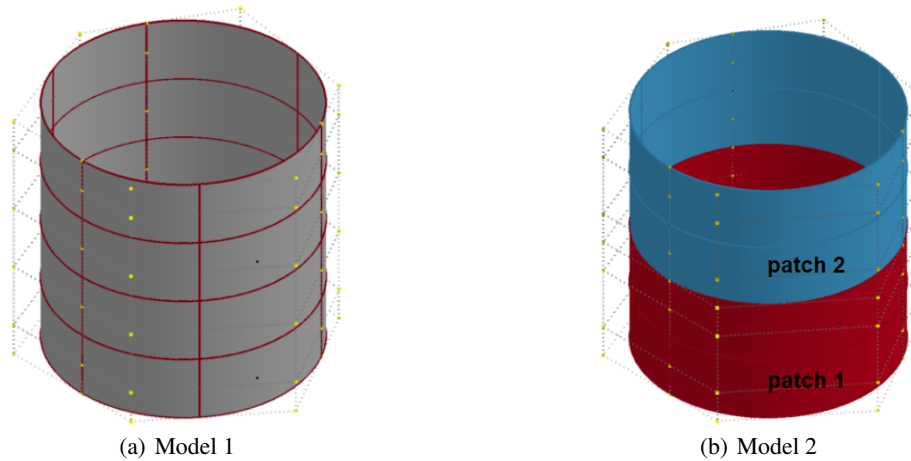


Figure 2.15: Schematic illustration of patch elements

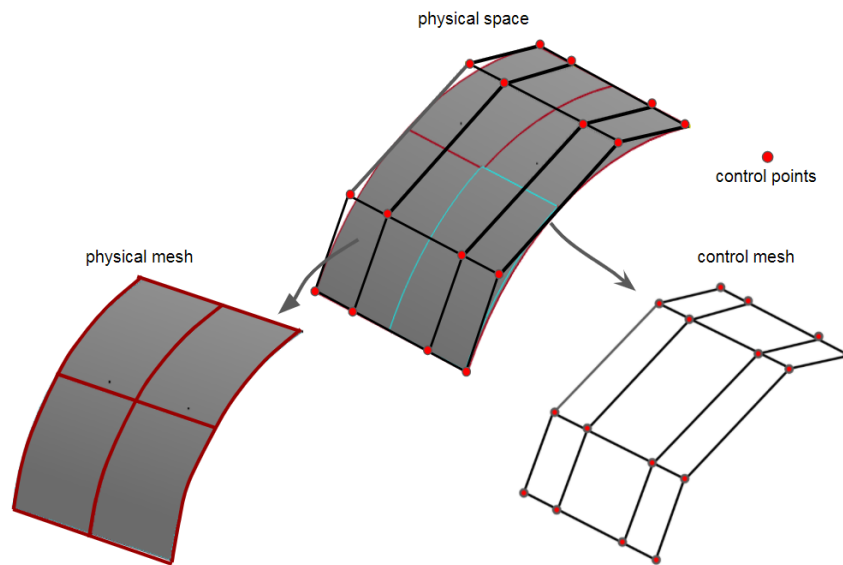


Figure 2.16: Schematic illustration of mesh elements

2.3 State of the art in IGA

At present, the researches in IGA are mainly in the aspect of isogeometric basis functions algorithm [16, 17, 50–54], contact mechanics [55–59], fluid mechanics [60–62], structural optimization [63–74], shell analysis [18, 75–79], damage and fracture mechanics [7, 11, 80], structural vibration analysis [81–86]. In the following, I will mainly present the IGA in the algorithm, structural optimization, shell, and vibration analysis.

- I) Isogeometric algorithm research

NURBS is widely used in CAD systems due to its distinct advantages, in which the most promising is in representing the free-form shapes, such as cylinders, spheres, ellipsoids, and conical sections [17]. However, with the wide

application, the NURBS basis function has been exposed to have some shortcomings. For example, NURBS using tensor product form makes local mesh refinement inefficient. Some structures like a cylinder surface cannot be represented by a simple sealed NURBS face, as there are gaps or overlaps at the junction of NURBS faces. These disadvantages must be improved so it can get a broader range of applications. Sederberg et al. [16] firstly introduced T-splines (non-uniform B-spline surfaces with T-junctions) to computer modeling program, in which the T-junctions enable control points to be inserted without changing the entire row or column of control points, and showed that compared with NURBS, T-splines has advantages in supporting local refinement and eliminating clearances or overlaps between faces and faces. As shown in Fig. 2.17 (a), two B-spline surfaces do not match exactly, and the C^{-1} continuity at the boundary of patches can affect analysis precision. After fixing, a gap-free T-spline surface can be obtained, like in Fig. 2.17 (b), which can save much time spent in repairing gaps and so improve the precision in analysis results.

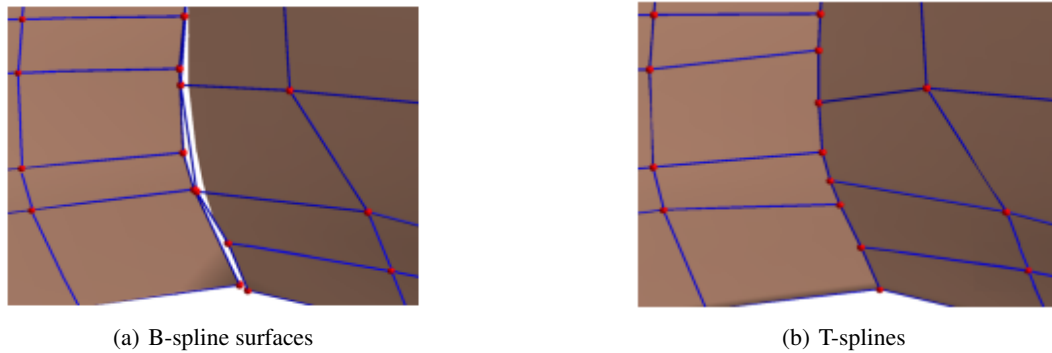


Figure 2.17: T-spline repairment (from [16])

Y. Bazilevs et al. [17] also reviewed the advantages of T-splines. As shown in Fig. 2.18, it can be seen that the control points of the NURBS surface lie in the way of rectangular mesh, topologically, in which most control points don't have significant geometric information and satisfy the topological constraints which to some extent, mean the more analysis time. By comparison, the head model constructed by T-splines has fewer control points, and the T-spline control mesh allows the addition of partial rows of control points without changing the surface. At the same time, Y. Bazilevs et al. developed fluid and structural mechanics analysis on two-dimensional and three-dimensional structures using the method of isogeometric analysis based on T-spline basis function and obtained good results.

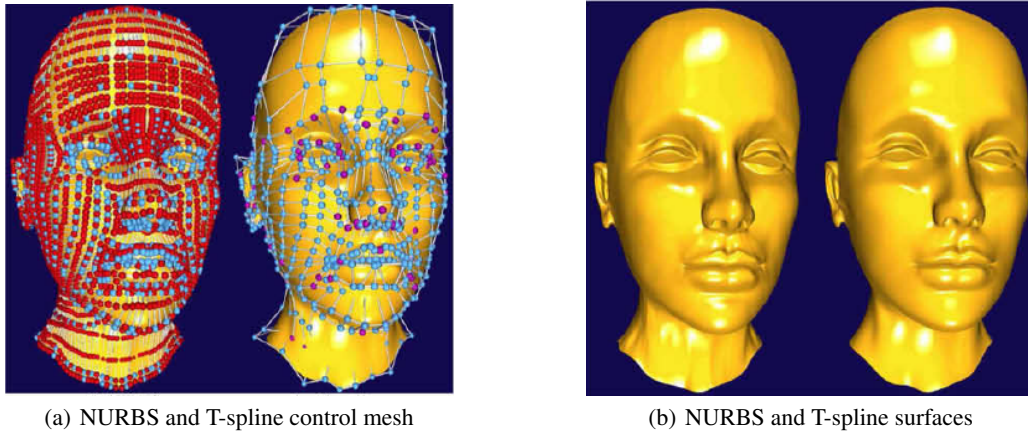


Figure 2.18: NURBS, T-spline control mesh and surfaces (from [17])

Dorfel et al. [51] presented a new local refinement method and combined this approach with the error estimation technique to obtain expected superior performance of isogeometric analysis on 2D examples; However, they also found that the local refinement led to an additional refinement step. In 2011, Wenyang Wang et al. [52] proposed a conversion algorithm method for obtaining T-spline surface or T-spline solids from any unstructured quadrilateral or hexahedral mesh; On the other hand, Wenyang Wang et al. also studied the Bézier extraction technique and linear independence property of the constructed T-splines to facilitate the T-spline based isogeometric analysis.

Through comparison with NURBS, T-splines have several advantages. However, the complexity of knot insertion for local refinement is far from trivial, particularly in 3D problems [51, 53]. Moreover, the linear independence of the T-spline basis functions is not available for generic T-meshes. Nguyen–Thanh et al. [53] proposed a new basis function for isogeometric analysis, that is, PHT-spline, which inherits almost all of the advantages of NURBS basis functions, including the non-negative, partition of unity, local support, etc., and developed isogeometric analysis based on PHT-spline basis functions on four models, and obtain that PHT-splines are superior to finite element cubic quadrilateral elements (FEA-Q16) and NURBS in terms of convergence rates and total errors, also PHT-splines support simpler local mesh refinement.

On the other hand, for obtaining a smooth surface from an input surface, usually, there are two processes, parametrization and construction of spline-based surface, in which the major challenge is in the parametrization process in designing an efficient algorithm to obtain the same topological structure as the input field. In 2017, Campen et al. [54] present a surface construction technique, T-splines with half-edge knots, which is a straightforward generalization of classical T-spline, and a class of parametrizations, a seamless similarity maps, from which a smooth piecewise rational surface with precisely the same input structure can be achieved for any given designs.

- II) Isogeometric design optimization

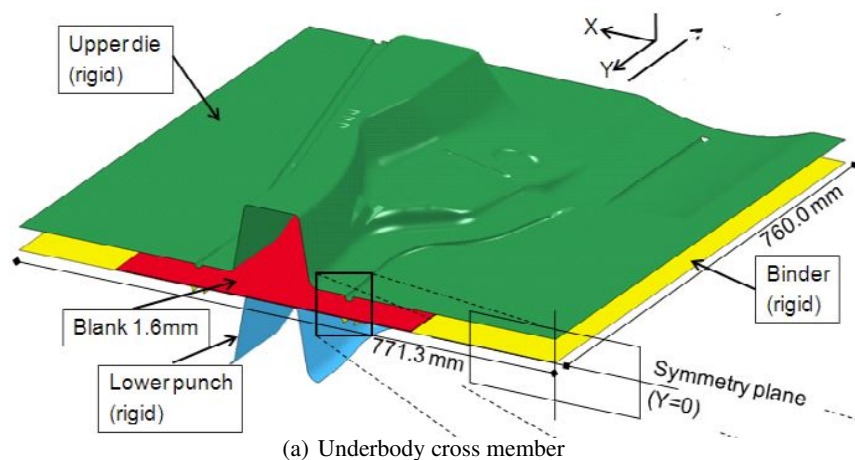
Structural design optimization is the eternal pursuit of the engineering community. It was initially achieved using classical analytical methods, such as variational or differential methods [56]. In 1960 Schmit [87] firstly combined finite element analysis with nonlinear mathematical planning methods for structural design. With the widespread application of computer technology in structural analysis, structural design optimization has evolved from low-level size and shape optimization to high-level topological, structural, and multidisciplinary optimization stages [56]. In most processes of structural optimization, the finite element method is often used to compute structural response and sensitivity. However, the approximate geometry description in classical FEA can cause accuracy issues. At present, B-spline and NURBS have been widely adopted in shape parameterization for structural optimization, since the work [88], in which the B-spline curves were applied to define design elements. The main reasons are because NURBS has a powerful capability in representing complex free form shapes and has a widespread application in CAD systems [89]. On the other hand, for finite element shape and topology optimization, the final design results depend on the mesh elements and extra post-processing steps to exchange data with the CAD system. The geometry and analysis models have different representations in the FEA field, making structural optimization more complicated. This urgently requires a close combination of CAD and CAE, and isogeometric analysis provides a promising way to combine design and analysis models. In 2005, Huges et al. [3] firstly proposed the isogeometric shape optimization method and mentioned that it has a distinct advantage when compared with classical finite element counterparts. Wall et al. [65] presented a framework of isogeometric shape optimization and applied it to the optimization problem of 3 classical cases, cantilever beam, plate with a hole, and a fully open end spanner structure, in which for the case of the cantilever beam, through the validation by an analytical solution, it has been obtained that the proposed method can provide a good result. Cho S et al. [66] proposed a continuum-based adjoint sensitivity method for isogeometric shape optimization and demonstrated the effectiveness and applicability of the isogeometric shape optimization method through the development of several cases. Ha S H [67, 68] introduced T-splines in isogeometric shape optimization to obtain optimal solution more efficiently and developed the T-spline and NURBS based isogeometric shape optimization on a bracket model. Nagy et al. [69] proposed isogeometric structural sizing and shape optimization approach on curved beam structures and also introduced a kind of multilevel approach, the combination of sizing and shape optimization, to solve the difficulties induced by structural sizing and shape optimization method. After Nagy et al. extended the isogeometric design framework to optimize elastic arches for fundamental frequency maximization [70]. Yu-Deok Seo et al. [71] developed isogeometric shape optimization on three cases, a fillet, a plate with a hole, and a cantilever beam, in which for the cantilever beam problem, T-splines were adopted to solve the geometric and numerical instabilities, and then extended this approach to topology optimization, showing the capability to combine shape and topology optimization based splines. However, they found problems in terms of the computation time and systematic strategy for topological changes. To address these challenges, Yu-Deok Seo et al. [72] also proposed a new spline-based topology optimization based on isogeometric analysis. Through numerical analysis, it has been observed that the proposed approach is beneficial in expanding flexible design space, treating design-dependent load problems, and integrating design optimization framework. Manh N D et al. [73] developed isogeometric shape optimization on vibrating membranes with the practical extension of a B-spline parametrization from the boundary of a domain onto its interior. Through the experiment with two numerical

methods, respectively based on constructing a quasi-conformal mapping and a spring-based mesh model, it has been concluded that isogeometric analysis fits very well with shape optimization.

- III) Isogeometric shell analysis

J. Kiendl et al. [79] developed isogeometric bending analysis in Ls DYNA software on a thin shell structure comprised of multiple patches. As Kirchhoff-Love shell theory depends on higher-order basis functions and NURBS elements are usually c^1 or higher-order continuities, J. Kiendl et al. [79] proposed Kirchhoff-Love shell theory based on isogeometric analysis, in which the bending strip method was introduced to treat c^0 patch boundaries, through adding strips of fictitious material with uni-directional bending stiffness and zero membrane stiffness at patch boundaries. The proposed framework demonstrated good analysis results through the application of a series of examples.

2011, Stefan et al. [18] developed isogeometric shell analysis on an underbody cross member and compared the isogeometric analysis with finite element analysis under the condition of different polynomial orders and element size. Through the comparison of draw-in length, contact forces between upper die and blank (as shown in Fig. 2.19 (a)) and CPU time, it was realized that IGA with higher polynomial order sometimes would not lead to better results, if the spacing of the control points will not be changed significantly. And under the condition of comparable discretization with standard linear finite elements, the NURBS shell elements can produce as good results as FEA with less CPU time. For example, for the comparison of contact forces and CPU time, as shown in Fig. 2.19 (b), a higher polynomial order will not produce better results because of the constant control point space, and from Fig. 2.19 (c), it can be observed that the computation time with quadratic NURBS elements with a mesh size of 4 mm (P2-4 mm) is about 30% faster than the one with linear standard shell elements with a mesh size of 2 mm (Std-2 mm). It is also necessary to note that these analysis results were obtained without optimized isogeometric code conditions. Through comparison with FEA, it can be concluded that under adaptive mesh refinements, isogeometric analysis can produce as good results as a comparable discretization with standard linear finite elements.



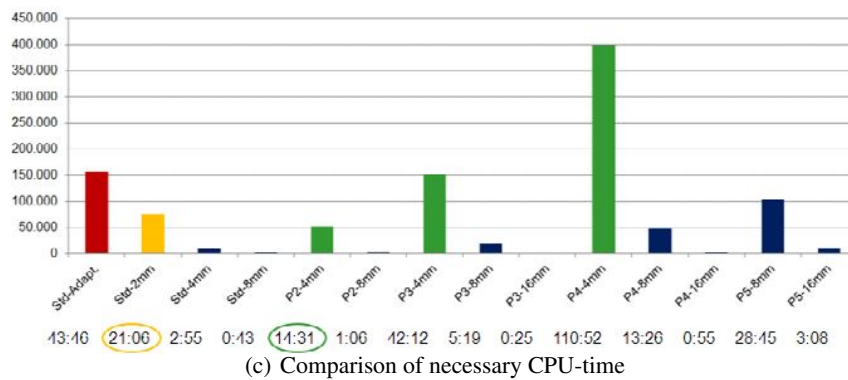
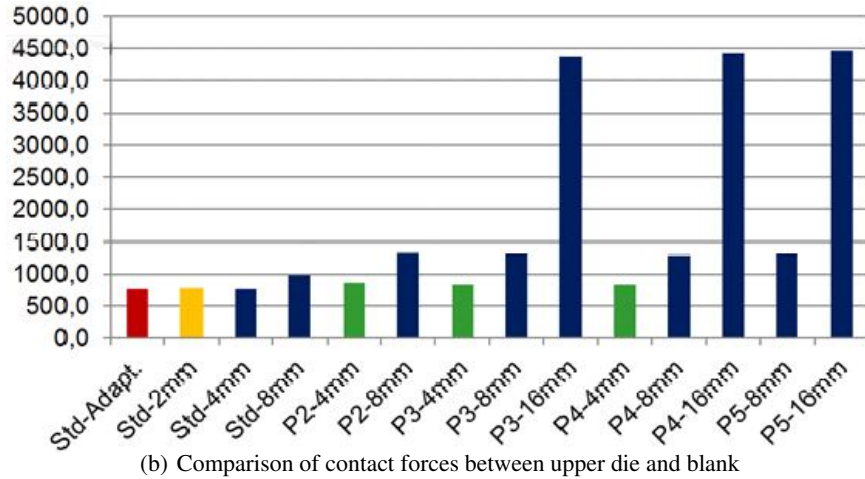


Figure 2.19: Isogeometric and finite element analysis comparison on a underbody cross member (from [18])

- IV) Isogeometric vibration analysis

Cottrell et al. [81] firstly developed isogeometric vibration analysis on several basic structural modes such as rods, beams, membranes, plates, and three-dimensional solids to verify the effectiveness of IGA on vibration problems; from the comparison point of view, with the finite element vibration analysis, it can be observed that the isogeometric analysis results are better than the finite element analysis results. On the other hand, Cottrell et al. [81] also developed isogeometric vibration analysis on a NASA aluminum tested cylinder, made a comparison between numerical analysis and experimental results, and obtained a good agreement. Sangmesh et al. [85] presented complete details of calculation, explanation, and examples in isogeometric static and vibration analysis with the use of Matlab code and verified the results by FEA.

Xiangkui Zhang et al. [82] presented isogeometric modeling with global Timoshenko beam theory, then developed modal analysis on a complex beam structure with random curvature and torsion, in which a multi-patch non-uniform B-spline represents the beam. The isogeometric analysis results were verified by finite element analysis. The results confirmed the efficiency and precision of this formulation. From analysis results, it can be observed that the IGA produces results as same as the FEA with the use of fewer elements; the locking problem can be solved by the increase

of the basis function orders; the number of the patch doesn't have effects on natural frequencies, which furtherly prove the effectiveness of this isogeometric formulations.

The locking problem is a notorious phenomenon in numerical simulation of beams and plates when elements used to analyze deep beams or thick plates are utilized to analyze slender or thin plates. This is featured that the obtained displacement is unreasonably small when calculating beams with large length-radius ratio [82]. At present, several methods were introduced to solve the locking problem in static isogeometric analysis, including the new \bar{B} method for volume and shear locking problems, RI method, order reduction method, the mixed formulation method, the DSG method, the single-variable method, assumed natural strain method, high-order non-uniform rational B-splines interpolation method, and couple polynomial field method.

2013, Dongdong et al. [83] presented a method of higher-order mass matrices to improve the accuracy of isogeometric vibration analysis based on NURBS results, in which the higher-order mass matrix is obtained through a mixed mass matrix that was formulated through a linear combination of reduced bandwidth mass matrix and consistent mass matrix, and verified this method on several models. The analysis results showed that the higher-order matrix method is efficient and can produce high order of accuracy. 2017, Ta Duy et al. [86] applied isogeometric vibration analysis on a stochastic structure with random material properties in which Young's modulus and mass density were modeled as homogeneous Gaussian random fields. In this study, the IGA vibration formulation is presented in the appendices A.

- V) Summary on present studies in IGA

From the papers above, obtain the following conclusions: I) in the isogeometric algorithm, the current research mainly focus on the improvement of basis functions properties to obtain a gap-free model and also develop a simple local mesh refinement method; II) in isogeometric shape optimization, 1) compared with finite element optimization, the isogeometric optimization has advantages in terms of the geometric representation and combination of CAD and CAE models; 2) most isogeometric design optimization is based on NURBS, but in some cases, T-spline based isogeometric optimization has also developed, as T-spline basis functions support local refinement and also seamless geometry, which are difficult to be accomplished using NURBS; 3) isogeometric topology optimization is available for specimen cases. 4) In IGA, both the control point location and weights have effects on a geometry representation, which can be explained by Fig. 2.20 which describes a NURBS surface consisting of the 4×3 control net. As shown in Figs. 2.20 (b) and (c), when control point position and weigh are altered from Q_a to Q_b and ω_a to ω_b , the related knot span and NURBS surface has also changed. However, until recently, for isogeometric shape optimization [66,67], the analytical sensitivities are mainly calculated based on the design variables of control point location. This is mainly due to the complexity in the derivation of analytical sensitivities for control point weights [19]. An analytical formulation of calculating sensitivities for both control point position and weight is necessary, this is because [19]: a) to obtain more precise and effective computation of derivative information essential in gradient-based optimization. b) to achieve more flexible and compact shape representation, and increase design space, which can lead to obtaining a class of optimal

design, including conic curves, circles, ellipses, and cylinders, spheres, ellipsoids; 5) Some scholars present formulation for the utilization of control point position and weights as design variables. It can be found that when compared with formulation just based on control point weight as a design variable, the proposed approach can obtain more robust optimization results.

However, it can also be found that isogeometric design optimization is mainly focused on some basic models. The main contribution of this study is that isogeometric design optimization is developed on an actual industrial model, and the elaborate process of the shape optimization is presented in chapter 4, which would provide easy access for a widespread application of the isogeometric design optimization. Ls DYNA software was chosen for this study. It is a high industrial software that has implemented IGA, and I was in touch with Ls DYNA developing team during my thesis preparation.

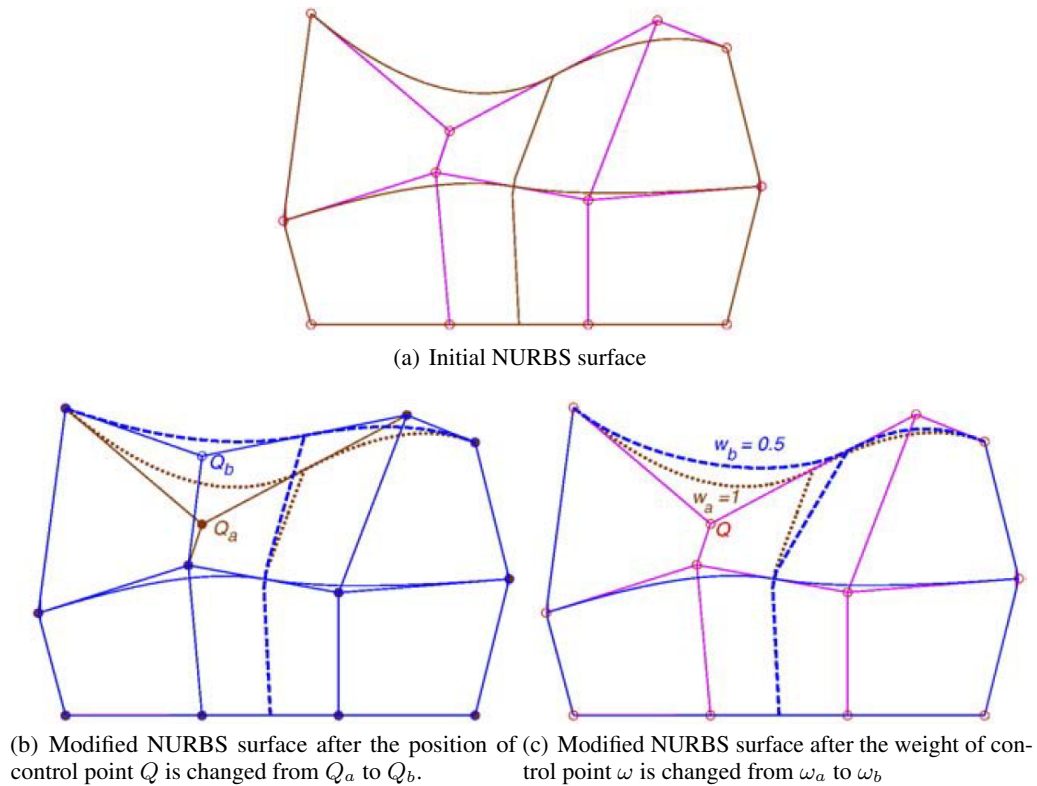


Figure 2.20: NURBS surfaces (from [19])

2.4 Comparison with FEA

The differences between IGA and FEA are the mesh elements formulation, choice of basis functions, and calculation of field variables in the governing equation. As shown in Figure 2.21, the mesh model obtained in FEA consists of mesh elements represented in physical space or parent domain [90]. In physical space, the mesh elements are defined by their nodal coordinates, and finite element basis functions, i.e. Lagrangian functions [49], that interpolate the coordinate between the nodes. Each element in the physical space can be mapped to the parent domain through coordinate transformation, in which the width and length of the parent element are respectively 1, and the Gauss integration is performed on the parent element.

In IGA besides the usual physical mesh and mesh in the parent domain, the control mesh is introduced. The control mesh is defined by control points. It defines geometry, however, it does not have to coincide with the real geometry of a studied object. In two dimensions the control mesh is a bilinear quadrilateral element [3]. The physical mesh is a representation of actual geometry. It is obtained by the projection of control points with NURBS basis functions, and the discretization is governed by knot vectors discretization in the parent domain. A physical mesh model can consist of several patches, e.g. subdomains in which the section and material properties are the same.

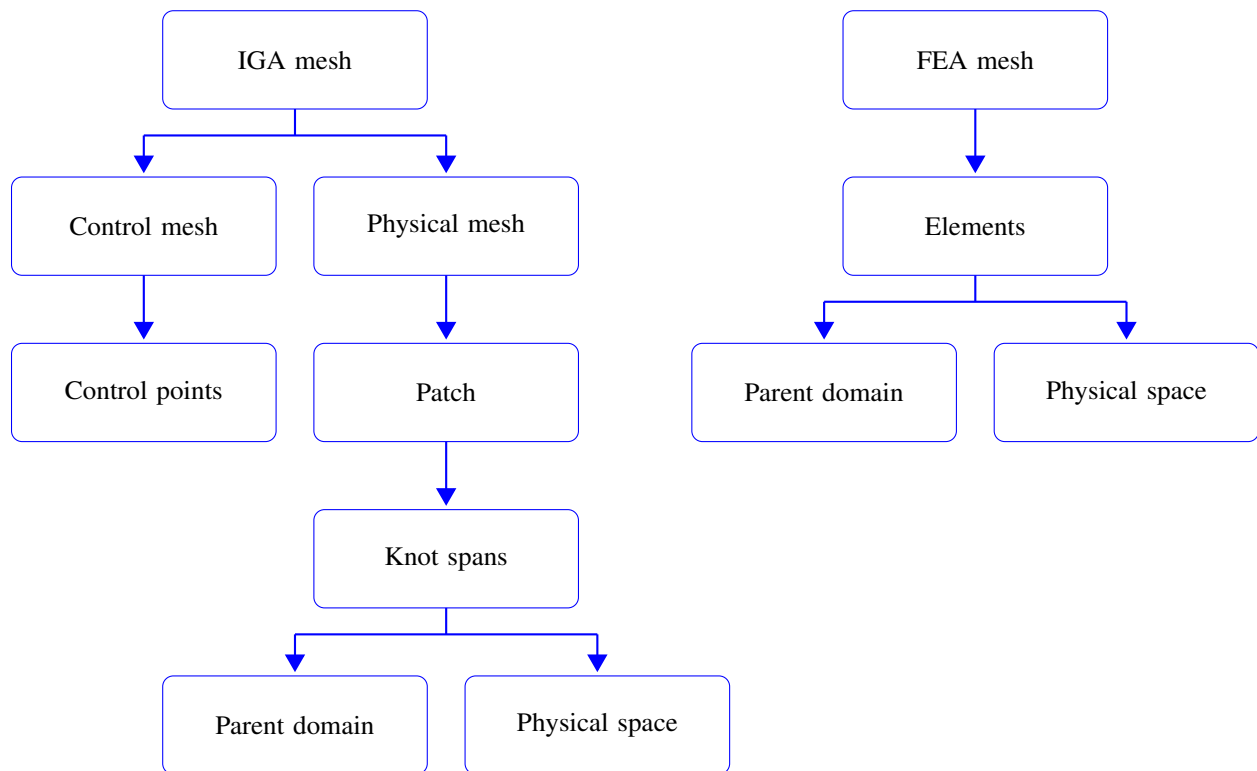


Figure 2.21: Meshing process in isogeometric and finite element analysis.

Next, IGA usually adopts the NURBS as its basis functions. Compared to Bernstein or B-spline basis functions, the NURBS basis functions possess more flexible properties and can exactly represent conic, circular and sphere models due to the effects of B-spline basis function and weight points associations [49]. For FEA, the Lagrangian basis functions shown in Eq. (2.51) are used to approximate solutions at element nodes [90]:

$$L_{i,p}(\xi) = \prod_{k=1, k \neq i}^{p+1} \frac{\xi - \xi_k}{\xi_i - \xi_k}, \quad 1 \leq k \leq p+1 \quad \text{and} \quad -1 \leq \xi \leq 1 \quad (2.51)$$

Due to the different nature of basis functions, the description model also gives different results. The critical properties are in variation diminishing characteristics and inter-element boundary continuity. The variation diminishing property (the number of sign changes) is used to characterize the smoothness of a curve. For FEA, the Lagrangian basis functions can have any sign ($-1 \leq \xi \leq 1$, $-1 \leq L_{i,p}(\xi) \leq 1$), so the oscillation of the fitting curve would be increased with the increase of the polynomial order, resulting in a non-smooth representation of the fitting curve (can not satisfy the variation diminishing property) and leading to contact problems between different description models. In IGA, the NURBS basis functions can satisfy non-negativity ($-1 \leq \xi \leq 1$, $0 \leq R_{i,p}(\xi)$). The obtained results, same as the NURBS curves, are less sensitive to the polynomial orders and can present a smooth representation of the geometry (possess the variation diminishing property) and the contact surfaces.

Additionally, the NURBS basis functions present c^{p-1-k} continuity, in which k is the number of repeating knots in a knot vector. However, the finite element basis functions are restricted to only c^0 continuity, leading to a non-smooth representation of the physical derivative quantities like stresses or strains.

Thirdly, in IGA, the combination of the control point \mathbf{P}_i and NURBS basis function are used to define NURBS-based elements, and field variables, such as displacement \mathbf{u} in Eq. (A.4), are performed based on control points. For FEA, the Langrangian based finite elements are defined by the combination of elements node variable \mathbf{X} and Langrangian basis function. The field variable \mathbf{U} in finite element weak formulation is performed based on element nodes [49, 90].

2.5 Application on a simple example

The IGA is developed on a plate model, in which the FEA and analytical solution verify the isogeometric analysis results. The geometric model of the plate is created in Ls Dyna, as shown in Fig. 2.22. Due to the symmetric effects in geometry and applied load, only a quarter of the model is analyzed. During convergence analysis, different densities of mesh models are constructed to investigate the CPU time and maximum stress in y -direction to demonstrate the differences between IGA and FEA.

2.5.1 Analysis preparation

- I) Geometric model

As shown in Fig. 2.22, the first analyzed model is a rectangular plate with the thickness e , length L_1 , width w_1 , and radius R_r of 0.001, 10, 2, and 0.25 (m).

The material of this model is steel DC01, and properties are given in Tab. 2.1.

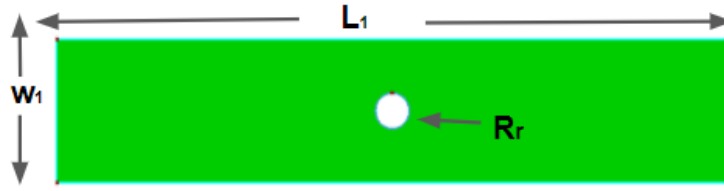


Figure 2.22: The schematic diagram of of the plate model

Table 2.1: Material properties

| Mass density | Young's modulus | poisson's ratio |
|------------------------|-----------------|-----------------|
| 7800 Kg/m ³ | 2.05e+11 Pa | 0.3 |

- II) Mesh models and boundary conditions

The isogeometric and finite element mesh models are presented in Fig. 2.23. In Ls Dyna, a load can be applied on either the NURBS element, chosen by using the keyword, LOAD NURBS SHELL, or on control points. In this section, the load is carried on control points to simulate the traction effects on the plate model. In terms of element formulation, the isogeometric shell element with NURBS is adopted. For FEA, considering analysis accuracy, quadrilateral four nodes elements are used to create mesh models. Because of the applied load condition, it is not necessary to consider the load effects in the z -direction. On the other hand, the aspect ratio $S_w = \frac{W_1}{e}$ of this plate is higher than 20, so plane stress shell element formulation, in which the normal stress σ_z and shear stress τ_{zx} and τ_{zy} are assumed to be 0 is selected in static analysis.

During numerical simulation, the boundary conditions are the same for IGA and FEA. The translational constraints in the x -direction and y -direction are respectively imposed on the bottom and right edges of the model, which are marked by black bracket, as shown in Fig. 2.23.

Then 1 Mpa traction load is applied on the control point (nodes in FEA) on the left edge in the y direction to develop convergence analysis, which is marked by red bracket. Here it is necessary to note that in Ls Dyna, the keyword, LOAD NODE SET, is used to develop force load for each control point, which means that the pressure load should be transformed to force load. Then the obtained force load is divided by the number of control points (for FEA, divided by the number of elements nodes) to calculate the forces for each control point.

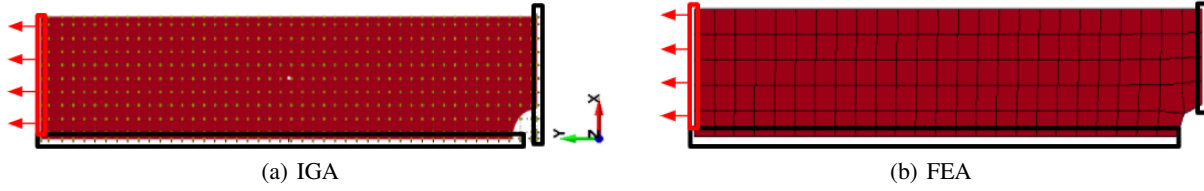


Figure 2.23: Mesh models and boundary conditions

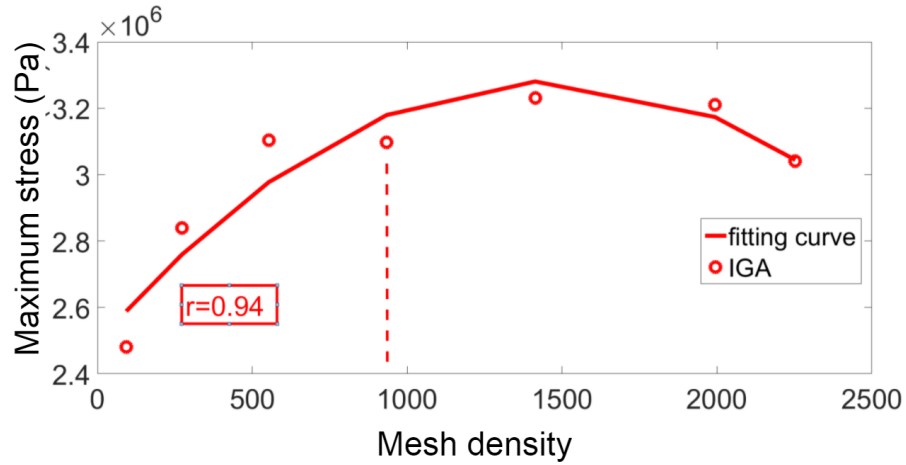
2.5.2 Analysis results

- I) Convergence analysis

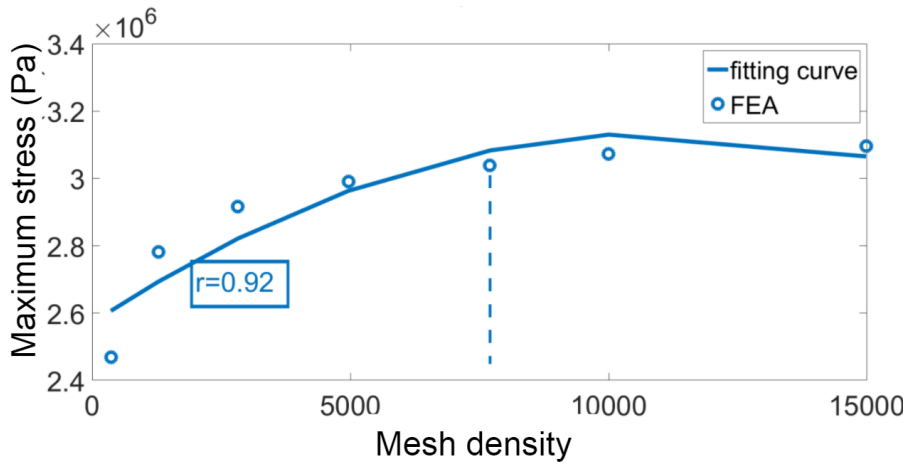
The maximum stress in the y -direction obtained from the static analysis is chosen to decide the convergence rate. From Figure 2.24, it can be seen that with the increase of control points number of IGA and element nodes number of FEA, the maximum stresses tend to reach a stable value. In order to show the isogeometric convergence analysis intuitively, a fitting curve is used to approximate the obtained maximum stresses from different analyses. Furthermore, the minimum correlation coefficient r , which is defined by Eq. (2.52) between the maximum stress values and the values obtained from the fitting curve, is 0.92.

$$r = \frac{\sum_{i=1}^n (Y_i - \bar{Y})(Y_{fit,i} - \bar{Y}_{fit})}{\sqrt{\sum_{i=1}^n (Y_i - \bar{Y})^2} \sqrt{\sum_{i=1}^n (Y_{fit,i} - \bar{Y}_{fit})^2}} \quad (2.52)$$

where Y_i and $Y_{fit,i}$ are the i th values obtained from the numerical analysis and fitting curves, \bar{Y} and \bar{Y}_{fit} are corresponding mean values, n is the extracted number sets and in this case n is 7. In this work, the convergence point is decided from the onset of the constant fitting curve. Thus, for IGA, the maximum stress values start to converge from the mesh density of 933 (the number of control points); for FEA, from the mesh density of 7701 (the number of element nodes). After the analysis results of these convergence points are obtained to compare the differences between IGA and FEA. On the other hand, we can observe some decreased stresses from isogeometric convergence analysis such as the stresses under mesh density of 2000 and 2200 (the final point from Figure 2.24 (a)) This is mainly because of the decreased applied stress on control points (in Ls DYNA, the applied load needs to be divided by the number of control points to obtain the load for each control point in this case). Under the mesh density of 2200, the control point load is smaller than the one under the mesh density of 2000, leading to more minor effects on the corner of the edge curve of the geometry and thus obtaining decreased stress. But, when the mesh density is large or enough, like in FEA, the load effects from element nodes on the corner may be minor. That's why in FEA, we can obtain a more smooth curve.



(a) IGA



(b) FEA

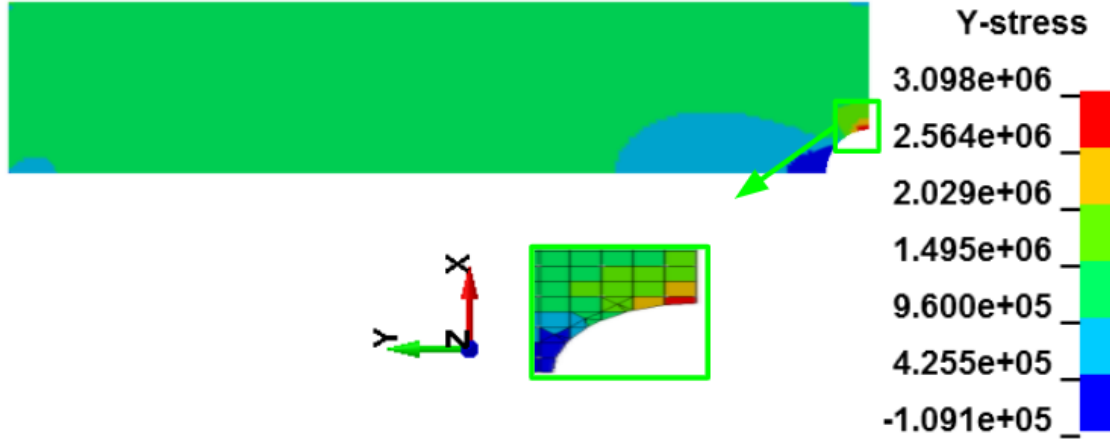
Figure 2.24: Convergence analysis results

- II) Maximum stress in y direction and CPU time

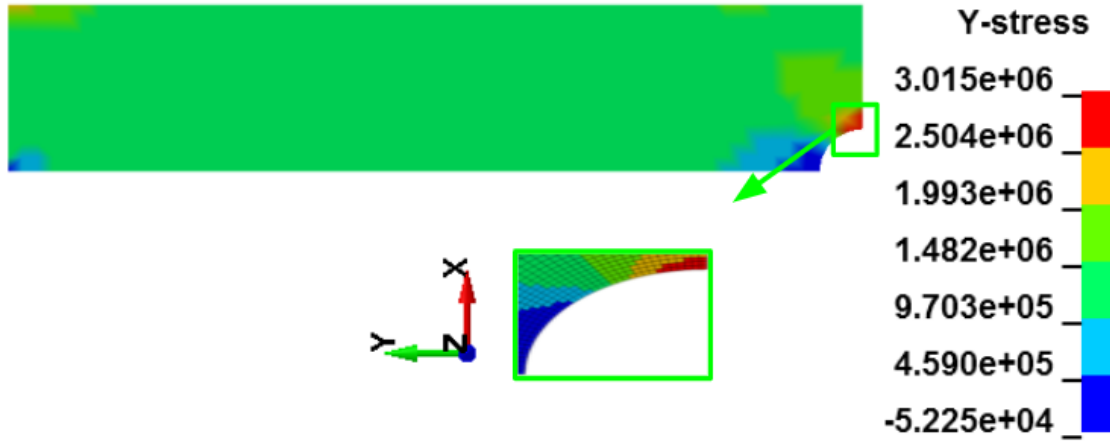
As shown in Fig. 2.25, the isogeometric and finite element maximum stresses are situated on the same zone, at the corner of curves, the values are respectively $3.098e+6$ and $3.015e+6$ pa , and the relative error is 2.7%, based on Eq. (2.53). The CPU time for IGA and FEA are respectively 74 and 720 seconds. It has been found that IGA is more time-efficient compared with FEA, with a time difference of 89%. This is mainly because of mesh density, as IGA can provide similar analysis results with FEA using fewer NURBS elements.

All the numerical calculations presented are run on the computer Intel(R) Core(TM) i5-6440HQ CPU 2.60GHz with RAM 8Gb.

$$Relative\ error = \frac{IGAresult - FEAResult}{FEAResult} \quad (2.53)$$



(a) IGA



(b) FEA

Figure 2.25: Maximum stresses in y directions

2.5.3 Analytical solution

The following well-known application [49, 91] is used to validate the isogeometric and finite element models developed in LS-DYNA software based on Kirsch's solution. A rectangular plate with a hole of radius a is loaded in the plane by a one-direction tension denoted by σ_∞ . The plane stress condition is considered. The plate parameters are depicted in Fig. 2.26 and the related analytical solution of the stress around the hole is given by [92]:

$$\begin{aligned}
 \sigma_{rr} &= \frac{\sigma_\infty}{2} \left(1 - \left(\frac{a}{r} \right)^2 \right) + \frac{\sigma_\infty}{2} \left(1 - 4 \left(\frac{a}{r} \right)^2 + 3 \left(\frac{a}{r} \right)^4 \right) \cos 2\theta \\
 \sigma_{\theta\theta} &= \frac{\sigma_\infty}{2} \left(1 + \left(\frac{a}{r} \right)^2 \right) - \frac{\sigma_\infty}{2} \left(1 + 3 \left(\frac{a}{r} \right)^4 \right) \cos 2\theta \\
 \tau_{r\theta} &= -\frac{\sigma_\infty}{2} \left(1 + 2 \left(\frac{a}{r} \right)^2 - 3 \left(\frac{a}{r} \right)^4 \right) \sin 2\theta
 \end{aligned} \tag{2.54}$$

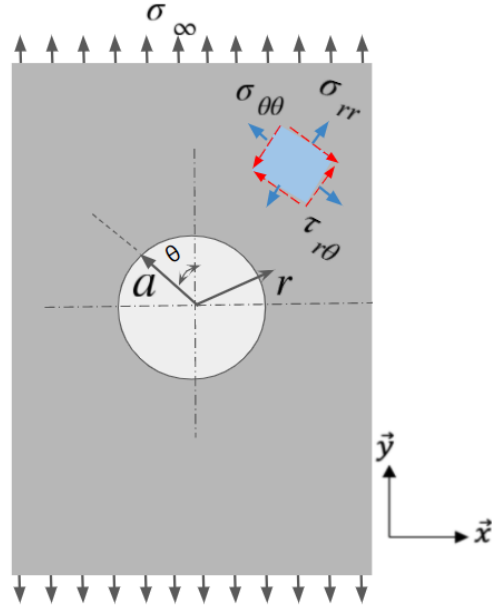


Figure 2.26: Schematic diagram of a plate model

at the hole ($r = a$), Eq. (2.54) becomes (the radial stress σ_{rr} and the shear stress $\tau_{r\theta}$ are zero):

$$\begin{aligned}
 \sigma_{rr} &= 0 \\
 \sigma_{\theta\theta} &= \sigma_{\infty}(1 - 2 \cos 2\theta) \\
 \tau_{r\theta} &= 0
 \end{aligned}
 \tag{2.55}$$

in addition, when $\theta = \pm 90^\circ$, the proportion between the obtained maximum stress $\sigma_{\theta\theta}$ and the applied stress σ_{∞} is 3. This analytical solution is used in the following section to compare FEA and IGA.

2.6 Conclusion

In this chapter, the definition and theoretical backgrounds of IGA are reviewed. Then, IGA is performed on a simple plate model, and FEA and the analytical solution verify the analysis results. By comparing the results, such as the proportion between the obtained maximum stress and applied stress, it is observed that the IGA and FEA results have a good agreement with the analytical solution. Through the comparison of the CPU time, we can find that IGA is time-efficient, compared to FEA, with a time difference of 89%.

Chapter 3

Random Vibration Fatigue Analysis on Mechanical Structures

3.1 Introduction

This chapter develops the IGA and FEA on a specimen with a reduced section and an L-shaped plate model. The own-developed Matlab programming validates the fatigue analysis results.

The static convergence analysis is fulfilled for the specimen to compare the IGA and FEA differences. Then, a random acceleration load is applied to the clamping fixture to assess the random vibration fatigue life, based on the fatigue analysis methods of Steinberg's three bands, Dirlik, Narrowband, Wirsching, Chaudhury and Dover, Tunna, Hancock. And the same excitation is considered in experimental tests to check the numerical results.

For the L-shaped plate model, the modal analysis is developed to compare the analysis results from the reference [5]. A random acceleration in the vertical direction to the plate surface is applied to the clamping fixtures to develop random vibration fatigue analysis. The Matlab program verifies the results.

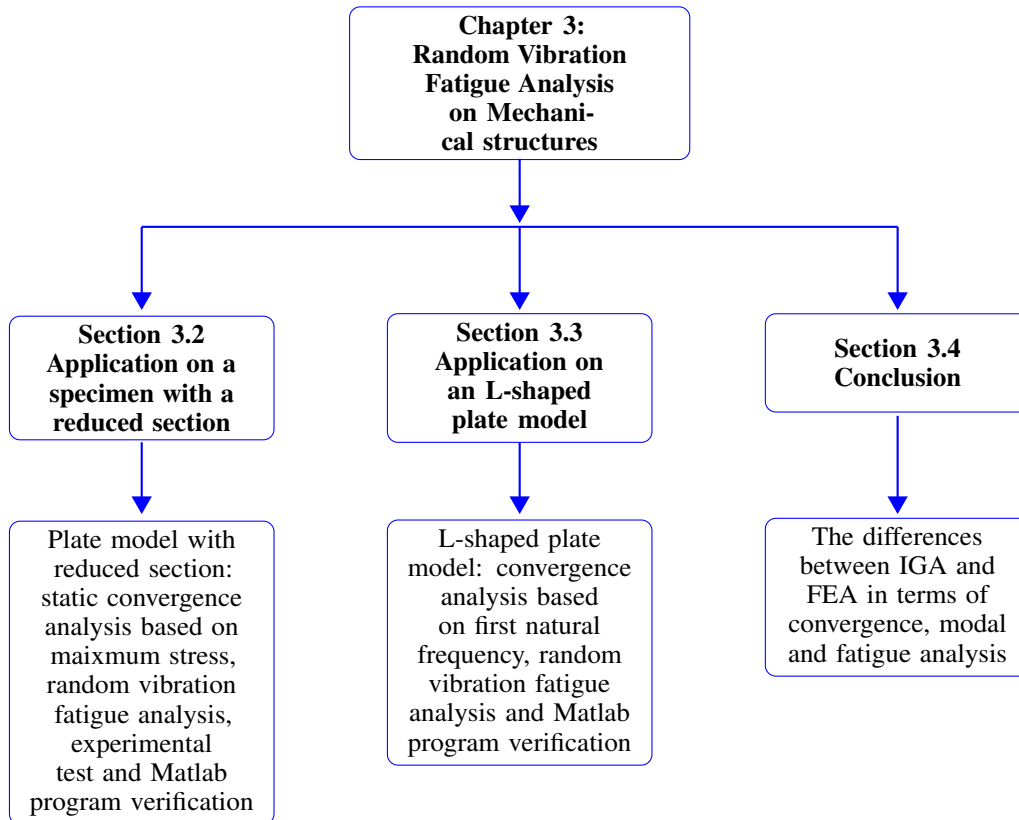


Figure 3.1: Schematic illustration of the third Chapter

3.2 Application on a specimen with a reduced section

3.2.1 Numerical study

- I) Analysis preparation

1) Geometric model

The plate model (as shown in Fig. 3.2), loaded in bending in the static analysis, is firmly clamped on the bottom side and kept free on the other. The reduced section is used to localize the stress away from the clamp. A random acceleration is applied to the clamping fixture during fatigue analysis.

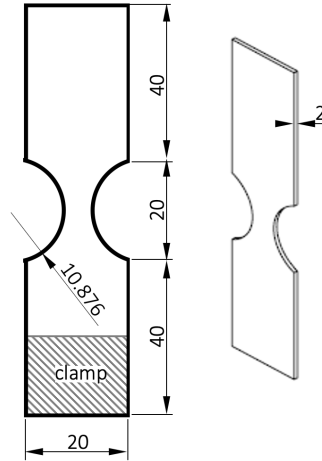


Figure 3.2: The plate model with reduced section

2) Material properties

The material properties of the model are given in Tab. 3.1.

Table 3.1: Material properties

| Mass density | Young's modulus | Poisson's ratio |
|------------------------|-----------------|-----------------|
| 7850 kg/m ³ | 1.7e+11 Pa | 0.3 |

3) Mesh models and boundary conditions

Isogeometric and finite element mesh models are presented in Fig. 3.3. In static analysis, the pressure load fixed at 100 Pa and represented by the red box, is applied on the first top row elements of the model in the minus z direction to simulate the bending effects in which the applied load area is always 5x20 mm related to the length portion and width of the plate. In IGA, the top row NURBS elements are selected by using the keyword, LOAD NURBS SHELL.

The boundary condition is the same for IGA and FEA. The translational and rotational constraints in the x , y , z directions represented by DOFX, DOFY, DOFZ, DOFRX, DOFRY, DOFRZ in Ls Dyna are respectively imposed on the bottom edges of the model, which are marked by the black bracket in Fig. 3.3. On the other hand, it is necessary to divide the 100 pa pressure load by the number of NURBS elements in top rows (for FEA, divide by the number of elements) to obtain the pressure load for each element.

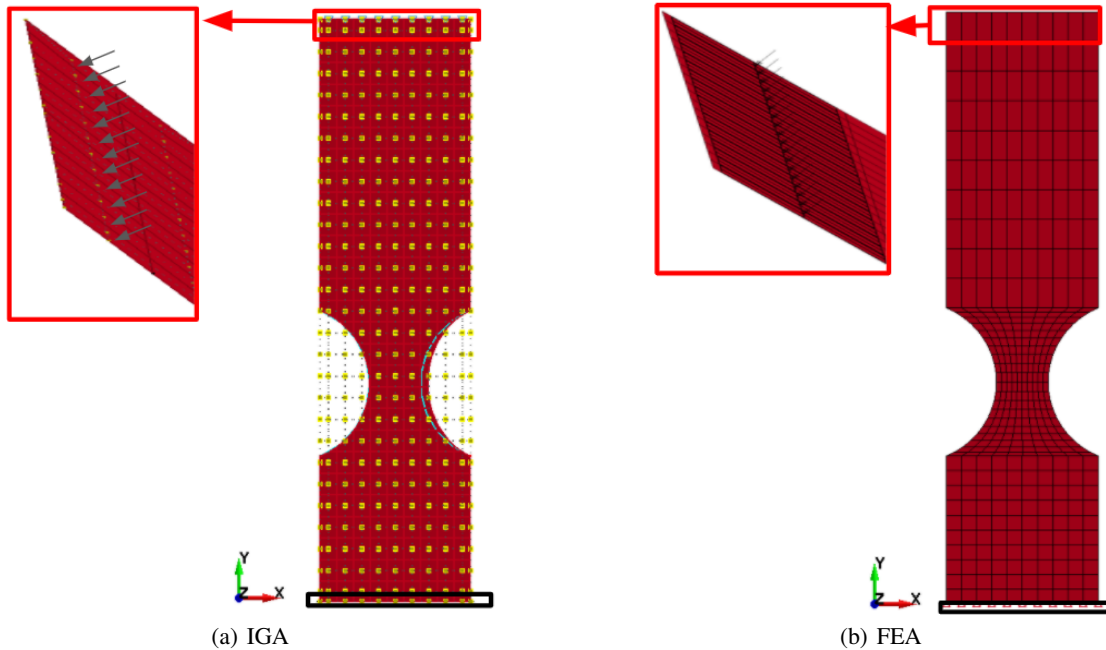


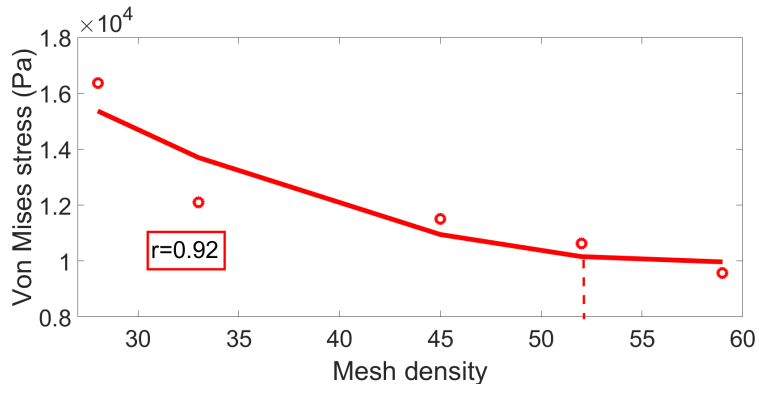
Figure 3.3: Mesh models and boundary conditions

- II) Analysis results

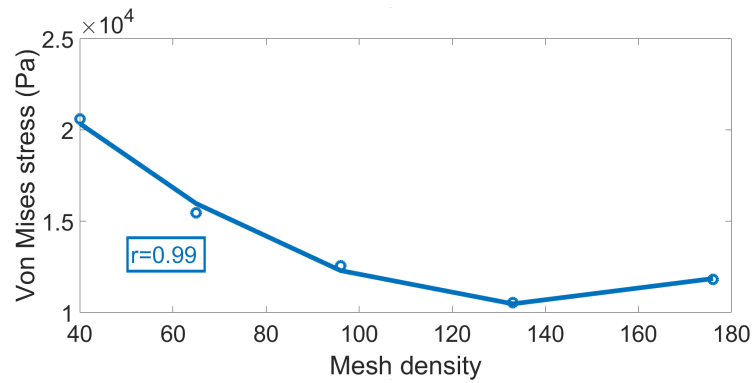
- 1) Convergence analysis

For convergence analysis, the von Mises stresses are computed to decide the convergence points. From Fig. 3.4, it can be observed that with the increase of control points and element nodes number, the von Mises stresses tend to reach stable value, in which fitting curves are used to approximate the obtained stresses. The computed correlation coefficients r between stress values and fitting curves are respectively 0.92 and 0.99.

For IGA, the maximum stress values start to converge from the mesh density of 52 (the number of control points); for FEA, from the mesh density of 133 (the number of element nodes). After the isogeometric and finite element convergence points are decided, the analysis results of these points are obtained to compare the differences between IGA and FEA.



(a) IGA



(b) FEA

Figure 3.4: Convergence analysis results

2) The maximum stress and CPU time

As shown in Fig. 3.5, the isogeometric and finite element maximum stresses are situated on the same zone, at the left notch edges, the values are respectively $1.062e+4$ and $1.054e+4$ Pa, leading to a relative error of 0.75%. The CPU time for IGA and FEA are respectively 231 and 462 seconds. It has been found that IGA is more time-efficient compared with FEA, which is the same as observed in section 2 for the static analysis of the simple plate model.

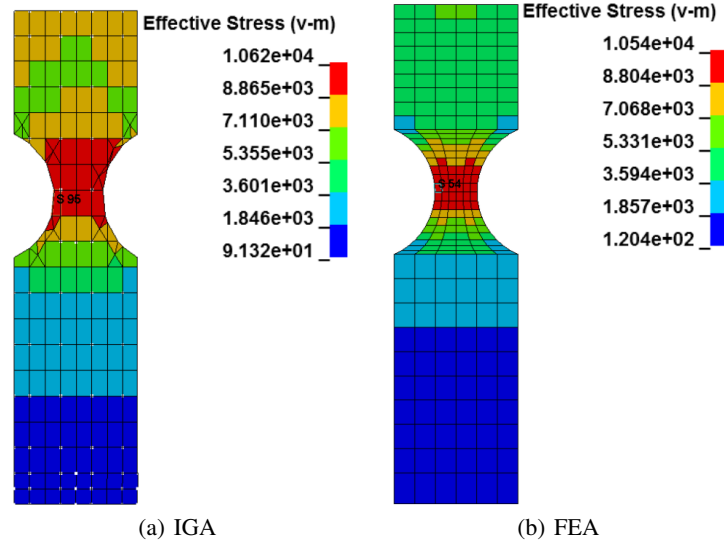


Figure 3.5: The effective stress

3) Fatigue analysis: modal analysis

After the convergence analysis, isogeometric and finite element random vibration fatigue analyses are developed. Tab. 3.2, Figs. 3.6 and 3.7 respectively demonstrate the first five natural frequencies and vibration modes. Through comparison, it can be observed that the obtained isogeometric and finite element natural frequencies and vibration modes match very well. The relative error for the first isogeometric and finite element natural frequency is 0.9%. We can also observe that the relative error for the second and fourth natural frequencies is higher. In our opinion, the difference is due to the low correlation observed in Fig. 3.4 (a). Therefore, the number of control points chosen for the IGA leads to a small deviation of the von Mises stress in static (see Figure 3.5) and to a more consequent deviation in dynamic especially for the pair modes (e.g. torsion). However, only the first mode is useful for this study because it causes the most damage. For this mode, the deviation of the displacements given in Figs 3.6 and 3.7 is small.

Table 3.2: The first five natural frequencies (Hz)

| | 1 | 2 | 3 | 4 | 5 |
|-------------------|-----|------|------|------|------|
| IGA | 211 | 1282 | 1510 | 1623 | 4253 |
| FEA | 209 | 1141 | 1506 | 1579 | 4266 |
| relative error(%) | 0.9 | 12.4 | 0.3 | 2.8 | -0.3 |

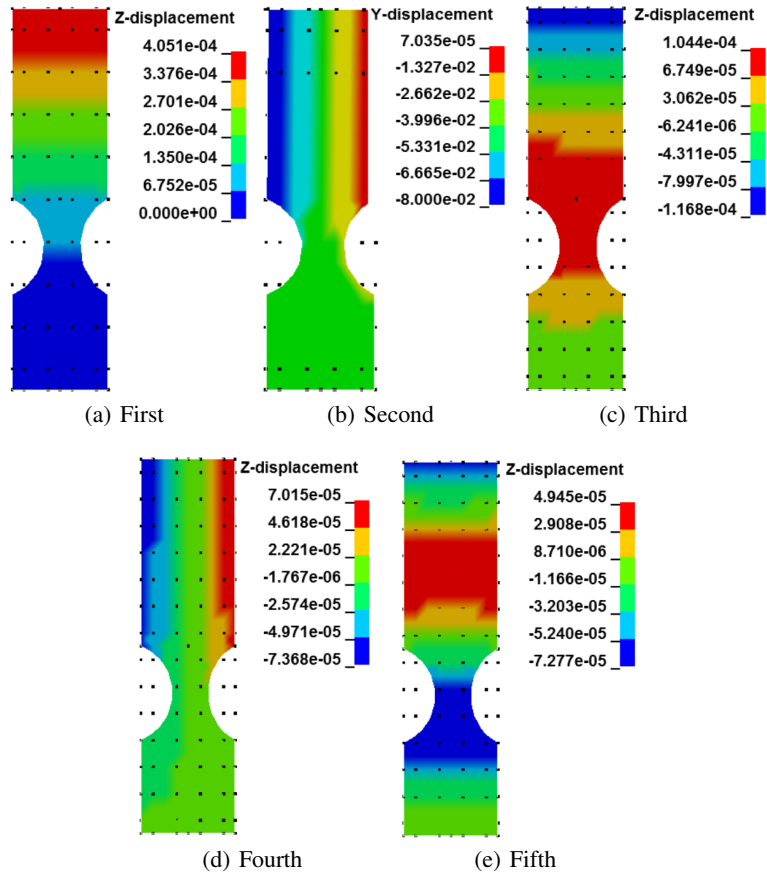
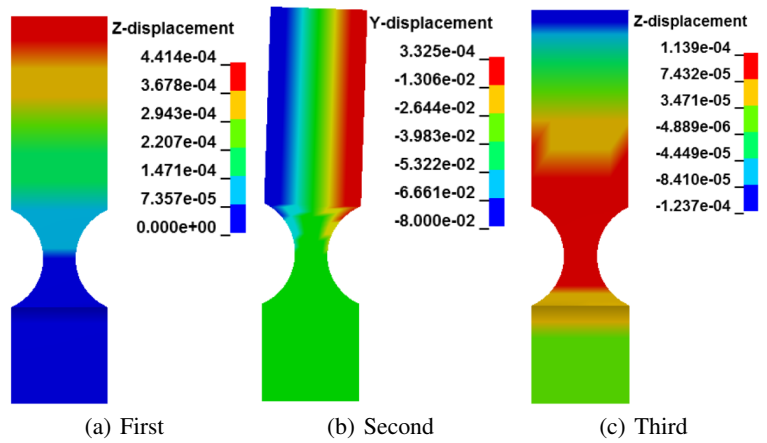


Figure 3.6: Isogeometric first five vibration modes



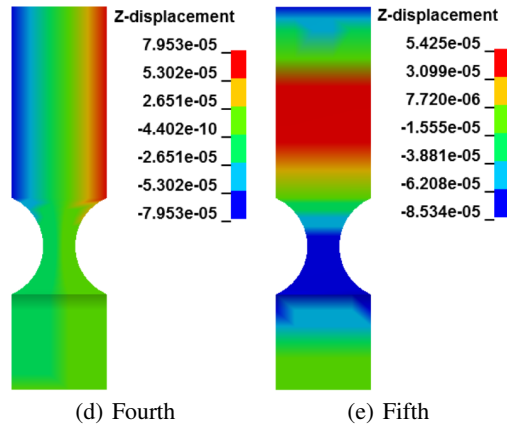


Figure 3.7: Finite element first five vibration modes

4) Fatigue analysis: random response analysis

The acceleration PSD depicted in Fig. 3.8 is applied on the control points (element nodes for FEA) in the z -direction to simulate the base acceleration. The damping ratio and exposure time are respectively set to 0.016 and 18000 seconds. The random vibration fatigue analysis is developed in Ls Dyna to obtain the effective stress PSD, RMS, and cumulative damage ratio. The material constants σ_f and b of the Basquin's equation (see Eq. (1.3)) are respectively $612.3 \pm 5\% \times 612.3$ MPa and -0.105, which are obtained from CES EduPackTM software. The margin on σ_f is used to take into consideration the material uncertainty and overcome the small number of specimens tested in the next section.

On the other hand, the obtained cumulative damage ratio would be validated based on obtained PSD from Ls Dyna and own-developed Matlab programming.

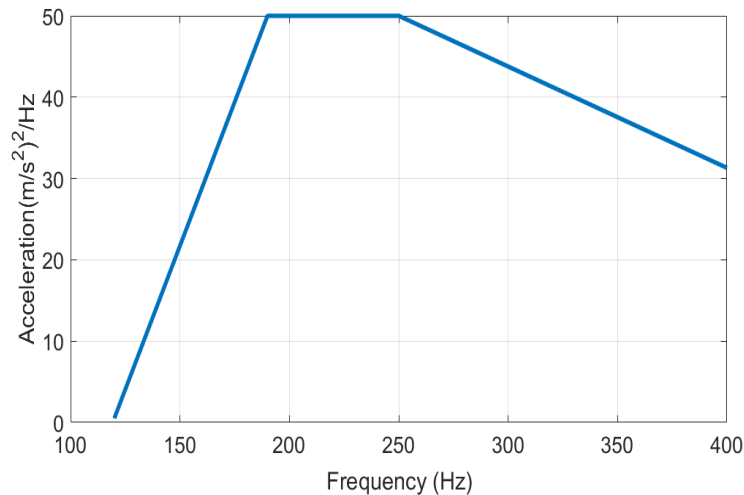


Figure 3.8: Applied acceleration PSD

Figs. 3.9 and 3.10 show the obtained isogeometric and finite element effective stress PSD and RMS. It can be seen that only the first natural frequency was excited by the acceleration PSD, and the resulting PSD and RMS are similar. The RMS values of the maximum effective stress obtained from IGA and FEA are respectively 5.240×10^7 and 5.278×10^7 Pa, leading to a relative error of -0.72%. Figs. 3.11 and 3.12, show the obtained cumulative damage ratios under different fatigue methods, it can be observed that the isogeometric and finite element maximum damage ratios based on Steinberg, Dirlik, and Tunna have good agreements, leading to the relative errors of 1.44%, 1.24%, 1.12% respectively (Tab. 3.3); however the maximum damage ratios from Narrowband, Wirsching, Chaudhury and Dover, Hancock are entirely different (Tab. 3.3); the maximum damage ratios calculated from Steinberg, Dirlik, and Tunna are similar, which is effective for both IGA and FEA, and the maximum damage are situated on same elements. On the other hand, compared with other fatigue analysis methods, Dirlik has long been regarded as an appropriate method for fatigue analysis. Thus, the following fatigue analyses were developed based on Dirlik's method.

The resulting expected damages based on the Dirlik method are respectively 1.449 and 1.467. According to the Eq. 1.29, the expected fatigue lives $E[T_f]$ are reported in Tab. 3.4. It can be observed that under different σ_f , the isogeometric and finite element fatigue life have a good agreement. Based on own developed Matlab programming, the isogeometric and finite element damage ratios are respectively 1.435 and 1.481 under the $\sigma_f = 612.3$ Mpa, which match very well with the damage obtained from Ls Dyna.

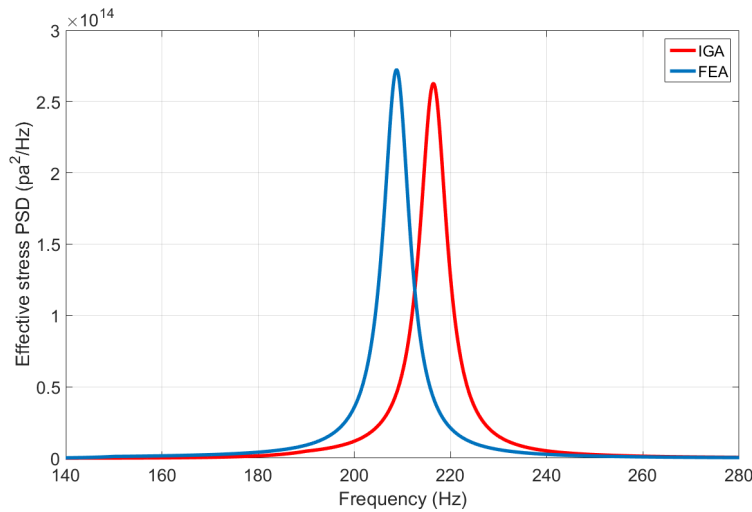


Figure 3.9: Effective stress PSD

Table 3.3: The isogeometric and finite element cumulative damage ratios

| Fatigue methods | Steinberg | Dirlik | Narrow band | Wirsching | Chaudhury and Dover | Tunna | Hancock |
|---------------------|-----------|--------|-------------|-----------|---------------------|-------|---------|
| IGA | 1.180 | 1.449 | 34.25 | 22.14 | 32.61 | 1.424 | 32.73 |
| FEA | 1.197 | 1.467 | 35.10 | 21.49 | 32.26 | 1.440 | 32.24 |
| relative errors (%) | 1.44 | 1.24 | -2.42 | 3.02 | 1.08 | 1.12 | 1.52 |

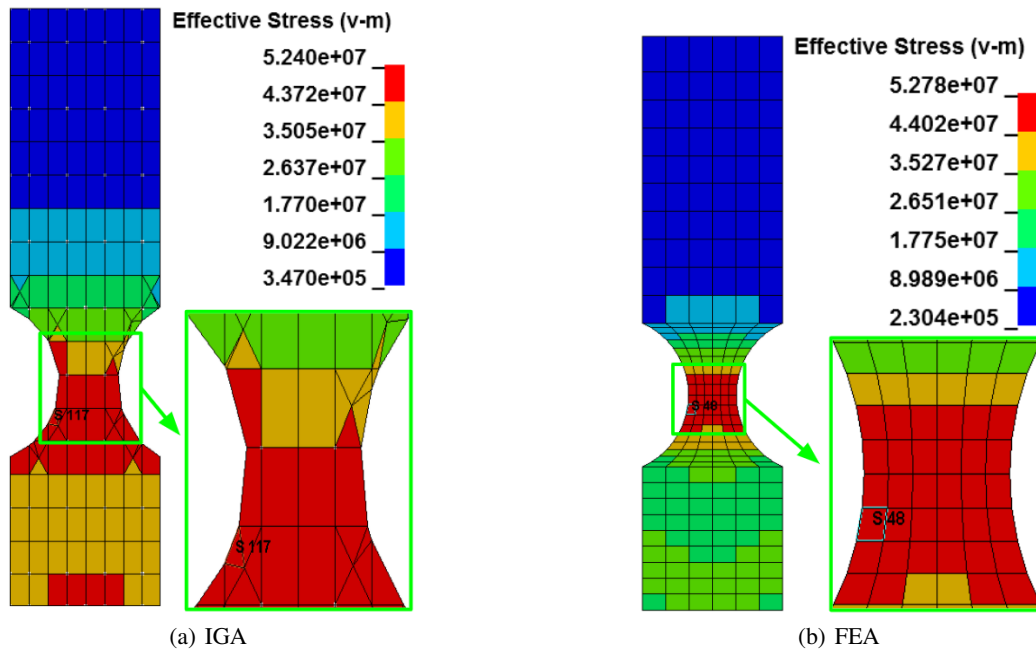


Figure 3.10: The effective stress RMS

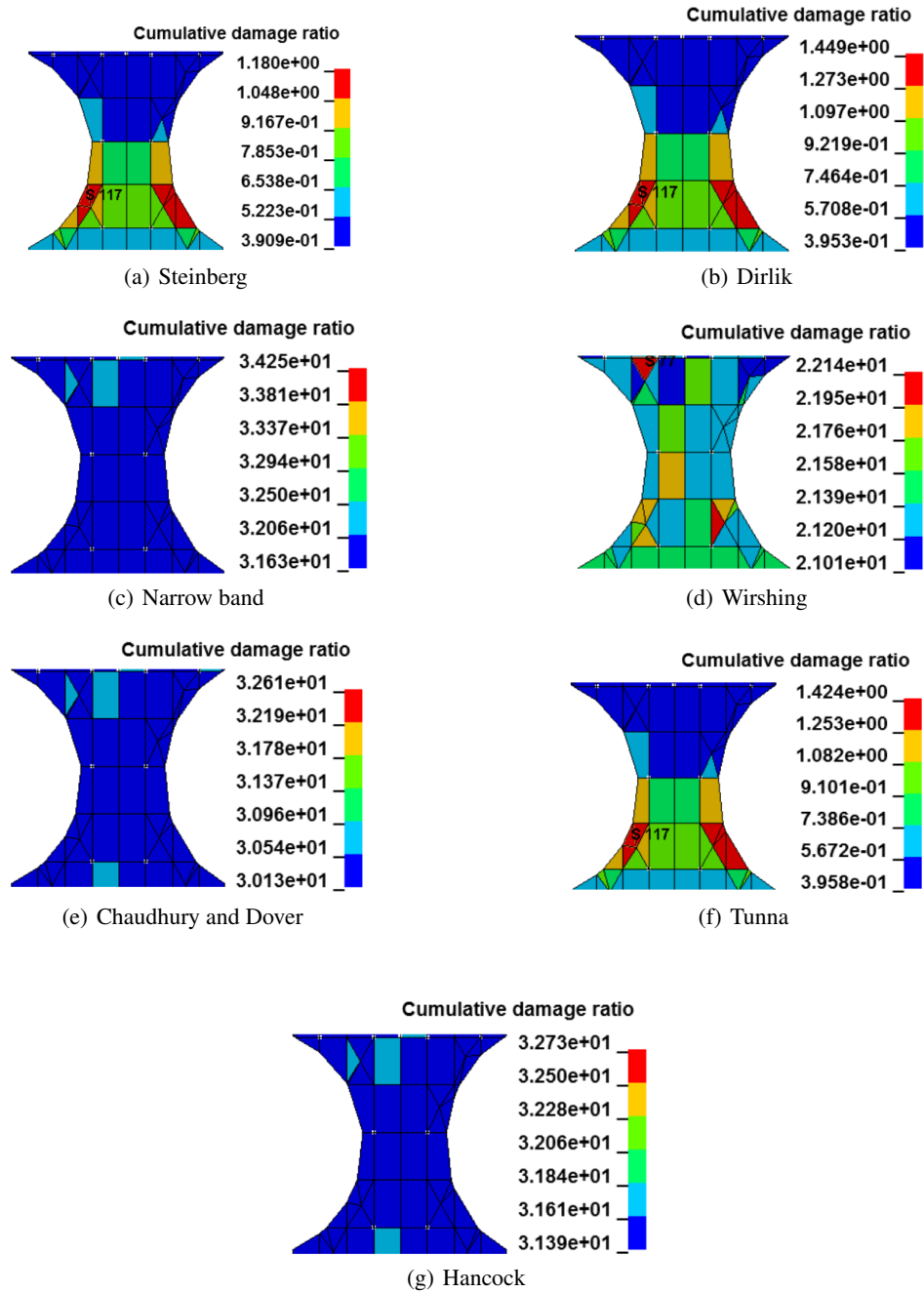


Figure 3.11: Isogeometric cumulative damage ratios

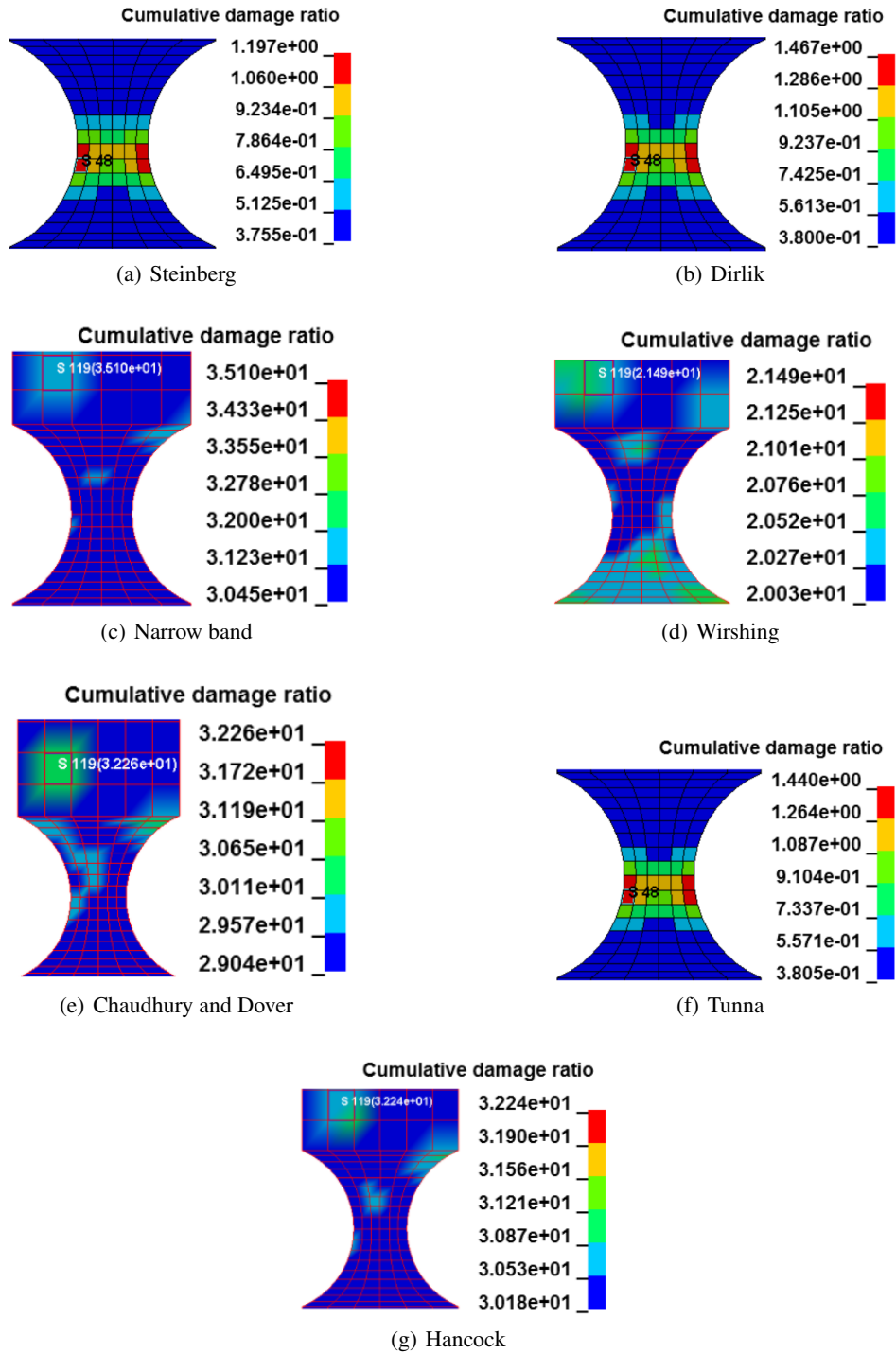


Figure 3.12: Finite element cumulative damage ratios

Table 3.4: The fatigue life $E[T_f]$ results related to the 5% variation of σ_f variation (in the units of hours: minutes: seconds)

| σ_f (Mpa) | 581.685 | 612.3 | 642.915 |
|------------------|---------|---------|---------|
| IGA | 2:19:40 | 3:27:02 | 4:48:43 |
| FEA | 2:17:06 | 3:24:30 | 4:46:48 |

3.2.2 Comparison with experimental tests

Three specimens were tested in fatigue induced by vibration. The test was carried out with random acceleration using the electrodynamic shaker TiraVib TV50100 + BAA1000 + 114 FPS (Fig. 3.13 (a)) of the Mechanical Laboratory of Normandy [93, 94]. Fig. 3.13 (b) gives a schematic representation of the system.

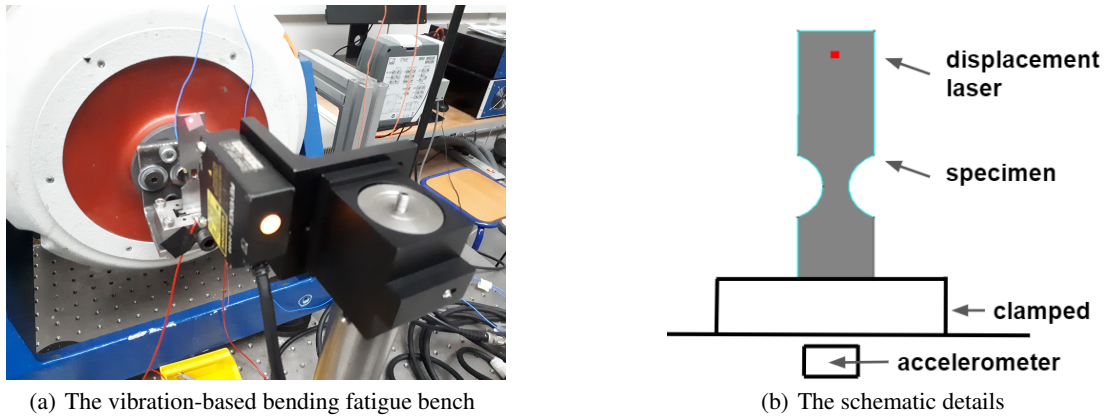


Figure 3.13: Schematic representation of the system

The series of three specimens used for the experimental tests were made of low-carbon steel DC01 (or St10 or XC10 or SAE 1010) with a yield stress of 235 MPa and Young's modulus of 170 GPa. A reduced section was designed on specimens to locate the crack away from clamp. The specimens were clamped on only one edge, the other remaining free. A transversal vibration was imposed at the clamp by driving the shaker with a closed-loop control devise (ACP or Acquisition Control Peripheral of Jaguar of spectral dynamic). The shaker drive is possible thanks to an accelerometer PCB 333A30 mounted at the specimen fixture. The response measurements of specimen are given by a laser displacement sensor REFERENCE located at the free edge and a strain gauge HBM 1LY15-1.5/350 was stucked at the center of the reduced section of the specimen. Frequency and time signal responses were continuously recorded respectively by the ACP and a HBM quantum device.

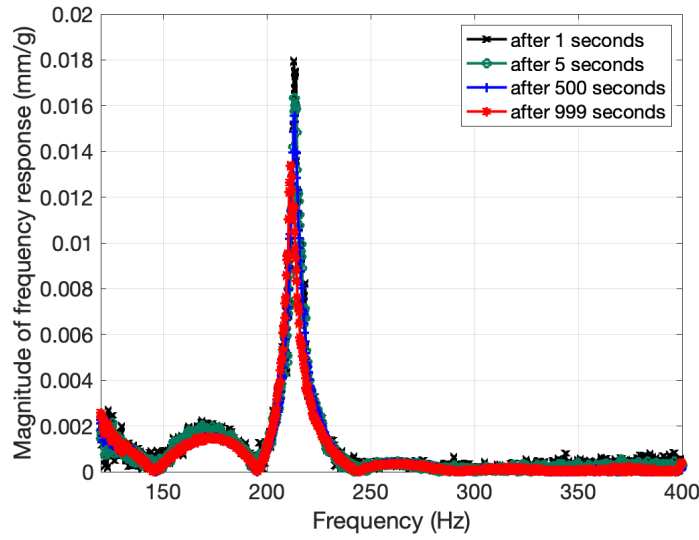


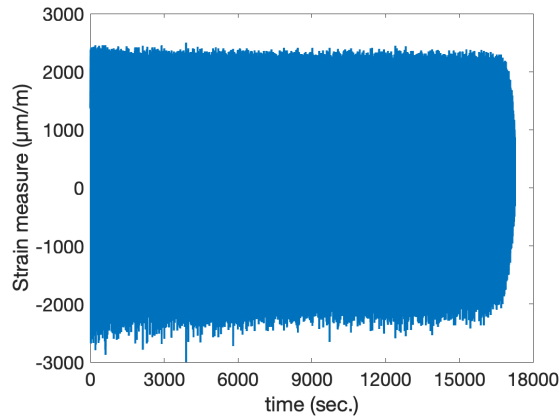
Figure 3.14: Frequency responses during fatigue test (4 measures)

The frequency response corresponding to the ratio of the displacement over the input acceleration were used to follow the resonant frequency of the system. If a crack occurs, a shift and a decrease of magnitude of the frequency response is observed. Therefore, it is possible to detect a change in the response of the specimen by the evolution of the resonant frequency deviation defined by:

$$RFD() = 100 \times \frac{f_r^0 - f_r^i}{f_r^0} \quad (3.1)$$

where f_r^0 corresponds to the initial resonant frequency of undamaged specimen and f_r^i is the i th measure of the resonant frequency during the fatigue test.

The strain signal in time recorded by the HBM device via the strain gauge is represented in Fig. 3.15 for the specimen S_1 (with a sampling rate 4800 per second). The related spectrogram given in Fig. 3.16 shows the evolution of resonant frequency during the exposure time. The deviation of this resonant frequency is clearly visible.



(a) Complete signal during fatigue test

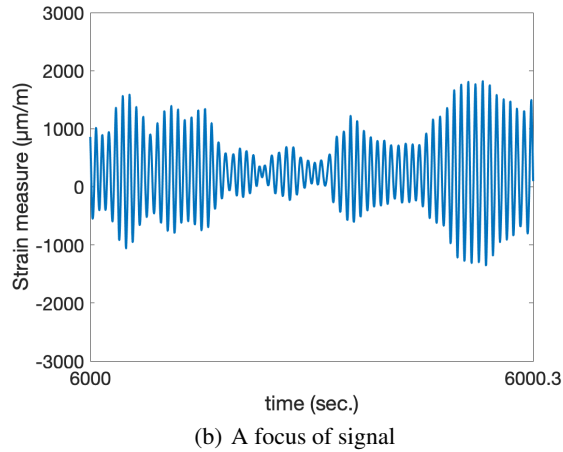


Figure 3.15: Strain measure

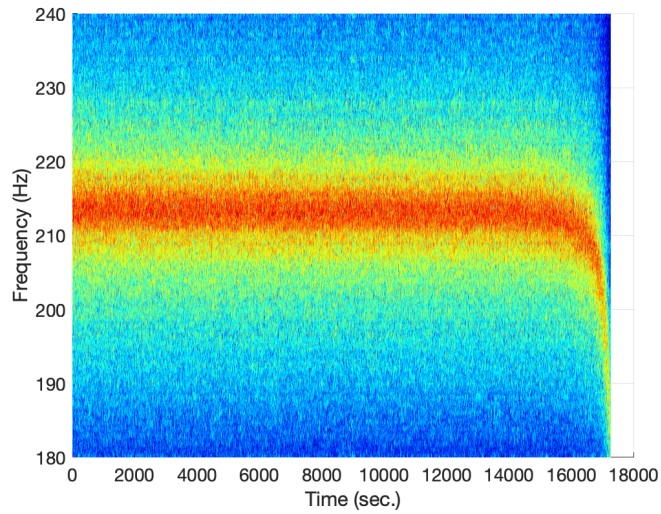


Figure 3.16: Spectrogram obtained from strain measure

Fig. 3.17 represent the RFD evolution extracted from the spectrogram. This evolution is represented versus the time and the number of cycles deduced from the frequency. When the crack has occurred, it can be observed that the RFD values increase with the crack growth. Based on the studies of Xu et al. [95] and Hu et al. [96], the fatigue lives of the specimens were determined for a RFD threshold fixed at 5%. The resulting fatigue lives obtained after the test of the three specimens are reported in Tab. 3.5. The lifetime obtained from the experimental tests are within the range obtained numerically from the values of σ_f .

Table 3.5: Results of the fatigue life $E[T_f]$ obtained from the resonant frequency deviation

| Id of specimen | Fatigue life (in hour) |
|----------------|------------------------|
| S_1 | 4:26:40 |
| S_2 | 3:30 |
| S_3 | 3:16:45 |

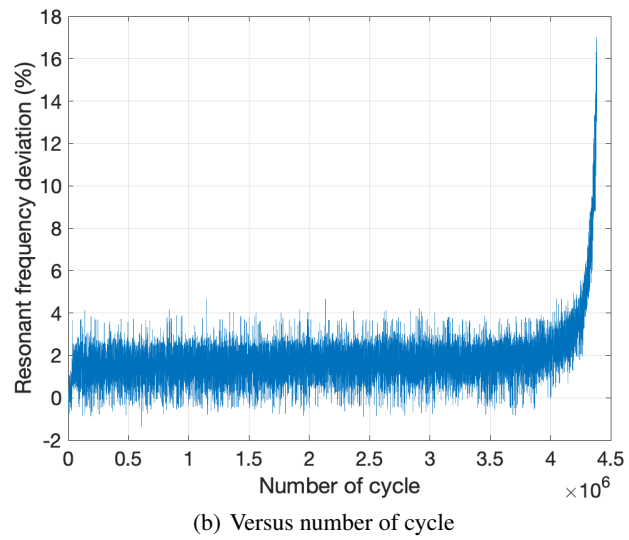
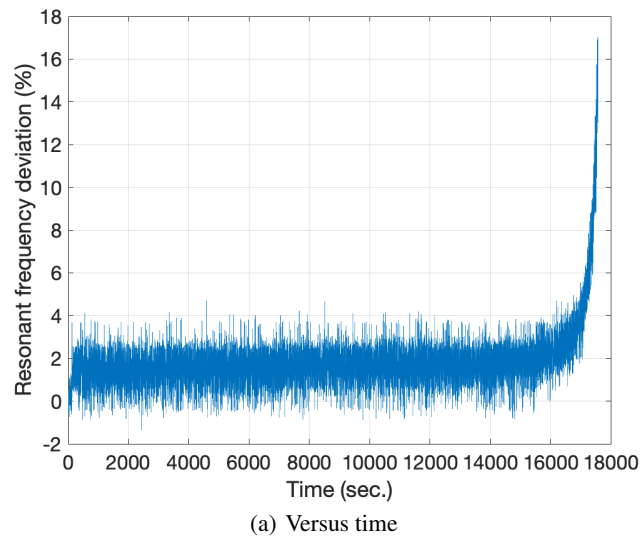


Figure 3.17: Resonant frequency deviation during fatigue test

3.2.3 Summary

In this section, isogeometric and finite element convergence and random vibration fatigue analyses were developed on the plate with notches model, in which the fatigue analysis results were validated by Matlab programming and experimental test.

In convergence analysis, the plate was clamped from the bottom side (see Fig. 3.3), and a 100 pa load was applied on top row elements to simulate the static bending problem. The results show that the IGA and FEA convergence analyses predict similar maximum stress values with the relative error of 0.75%, which are situated in similar locations; the CPU time of the IGA and FEA is respectively 231 and 462 seconds. It can be seen that IGA is more time-efficient compared with FEA.

The modal analysis results show that the obtained natural frequencies and vibration mode from IGA and FEA match well, in which the relative error of the first natural frequency from IGA and FEA is 0.9%.

In fatigue analysis, a random vibration acceleration in the vertical direction to the plate surface was applied to the clamping fixture to simulate the base acceleration. There were three kinds of comparisons in damage and fatigue life. Firstly the simulation results show that the obtained maximum effective stress RMS and cumulative damage ratio from IGA and FEA have a good agreement, with the relative errors of -0.72%, 1.2% respectively. Secondly, based on Matlab programming, the predicted isogeometric and finite element damage ratios are 1.435 and 1.481, close to the damage values calculated from Ls Dyna, 1.449 and 1.467. Thirdly, the average fatigue life obtained from the experimental test is 3:30, which agrees very well with the isogeometric and finite element fatigue life calculated from Ls Dyna under $\sigma_f = 612.3$ MPa, 3:27:02 and 3:24:30 (hours: minutes: seconds).

3.3 L-shaped specimen

3.3.1 The analysis preparation

Isogeometric and finite element convergence and random vibration fatigue analyses are developed on an L-shaped plate model [5] to compare the IGA and FEA differences in terms of mesh generation time, modal analysis, and fatigue analysis results.

- I) Geometric model

The model is featured by a hole, two notches as shown in Fig. 3.18, in which the thickness is 0.5 mm.

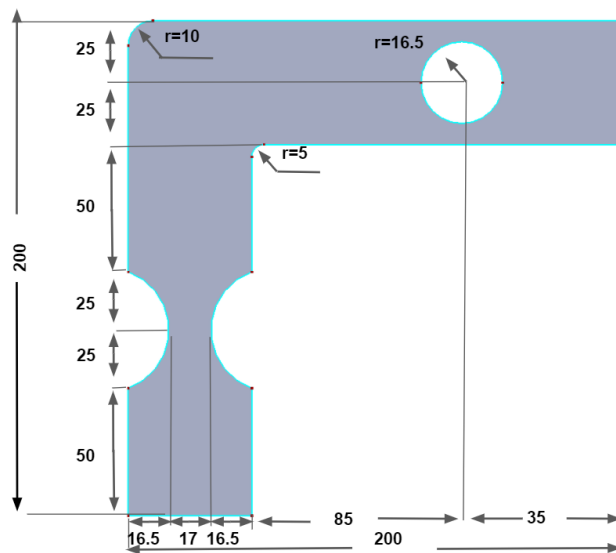


Figure 3.18: Dimensions of the plate (in mm)

- II) The material properties

The material properties of the plate model are given in Tab. 4.2. And the material constants of the S-N curve are respectively $\beta=9.82$ and $C = 4.0641 \times 10^{88}$ [5].

Table 3.6: Material properties

| Mass density | Young's modulus | poisson's ratio |
|--------------------------|----------------------|-----------------|
| $3.81e-3 \text{ g/mm}^3$ | $3.1e+11 \text{ Pa}$ | 0.33 |

- III) Mesh models and boundary conditions

Isogeometric and finite element mesh models both described by shell element formulations Huges-Liu are presented in Fig. 3.19. During the finite element mesh generation process, to obtain a finely discretized mesh model, firstly, the

geometry model is split into several parts (see Fig. 3.19 (c)); then each created mesh parts are assembled to achieve the final mesh model (see Fig. 3.19 (b)). This process is always time-consuming. During each mesh refinement process in the convergence analysis, it is necessary to communicate with the original geometry model, and the process almost occupies 80% of the whole analysis time. But for IGA, this process may take the occupation of 10%.

The boundary conditions are the same for IGA and FEA. The translational and rotational constraints in the x, y, z direction, which are represented by DOFX, DOFY, DOFZ, DOFRX, DOFRY, DOFRZ = 1 in Ls Dyna, are respectively imposed on the two edges, marked by the black bracket in Fig. 3.19.

Then isogeometric and finite element convergence analyses are developed under different mesh densities based on modal analysis. The first five natural frequencies are required to compare the results, and the first natural frequencies are used as a criterion to choose the convergence points.

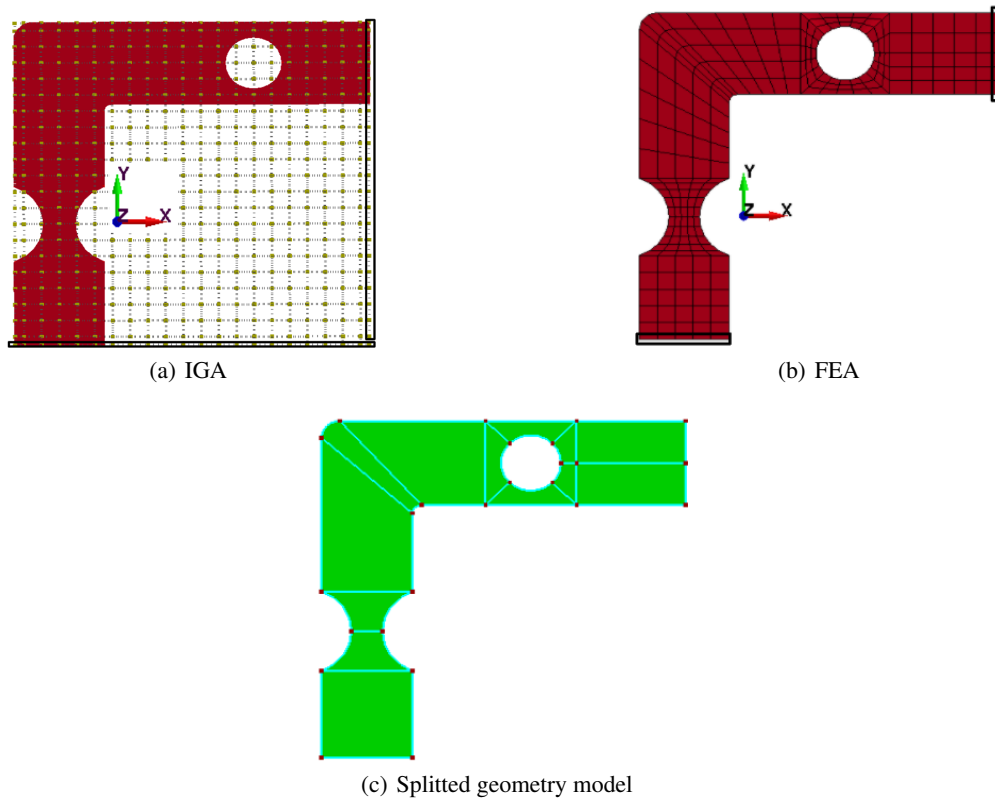


Figure 3.19: Mesh models

3.3.2 Analysis results

- I) Convergence analysis: the first five natural frequencies and mode shapes

The first five natural frequencies obtained from the X.Pitoiset et al. [5] are presented in Tab. 3.7.

Table 3.7: The first five natural frequencies from [5]

| 1 | 2 | 3 | 4 | 5 |
|------|-----|-------|-------|-------|
| 27.7 | 108 | 128.8 | 292.4 | 296.5 |

Fig. 3.20 shows the isogeometric and finite element convergence analysis results. It can be seen that with the increase of control points and node numbers, the first natural frequencies tend to converge, in which fitting curves are used to approximate the obtained natural frequencies. The computed correlation coefficients r between frequency values and fitting curves are respectively 0.99 and 1.

For IGA, the first natural frequency starts to converge from the mesh density of 738 (the number of control points); for FEA, from the mesh density of 704 (the number of element nodes). Then the natural frequencies and vibration modes decided from convergence points are obtained to compare the differences between IGA and FEA.

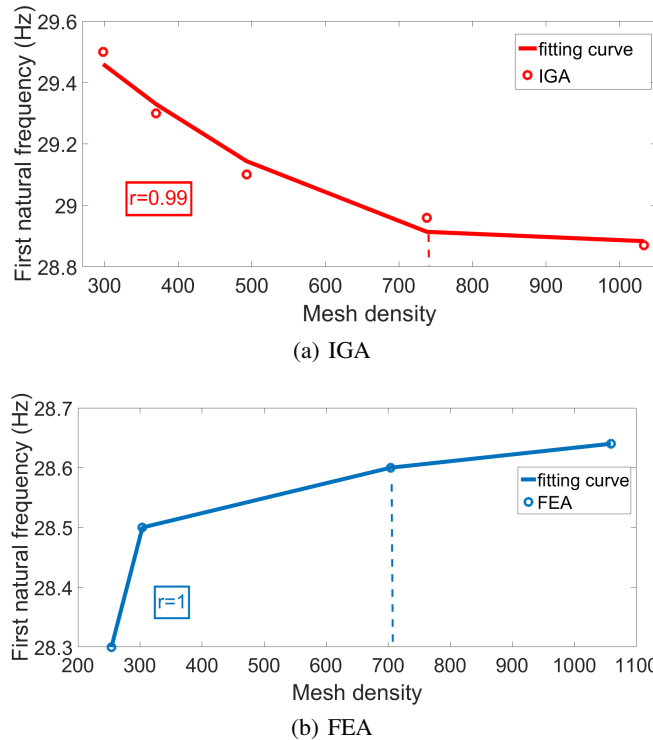


Figure 3.20: Convergence analysis

From Tab. 3.8, it can be seen that the first five natural frequencies computed from IGA and FEA have a good agreement. The first natural frequencies are 28.96 and 28.63 Hz, respectively, leading to the relative error of 1.15%, similar to the first natural frequency of 27.7 Hz obtained from Pitoiset.

Figs.3.21 and 3.22, respectively show the first five vibration modes. Through comparison, it can be observed that the mode shapes obtained from the FEA and IGA agree very well.

Table 3.8: The first five natural frequencies (Hz)

| Method | CPU | 1 | 2 | 3 | 4 | 5 |
|--------|----------|-------|--------|--------|--------|--------|
| IGA | 1 second | 28.96 | 112.28 | 132.93 | 298.10 | 304.88 |
| FEA | 1 second | 28.63 | 114.42 | 131.30 | 299.63 | 303.78 |

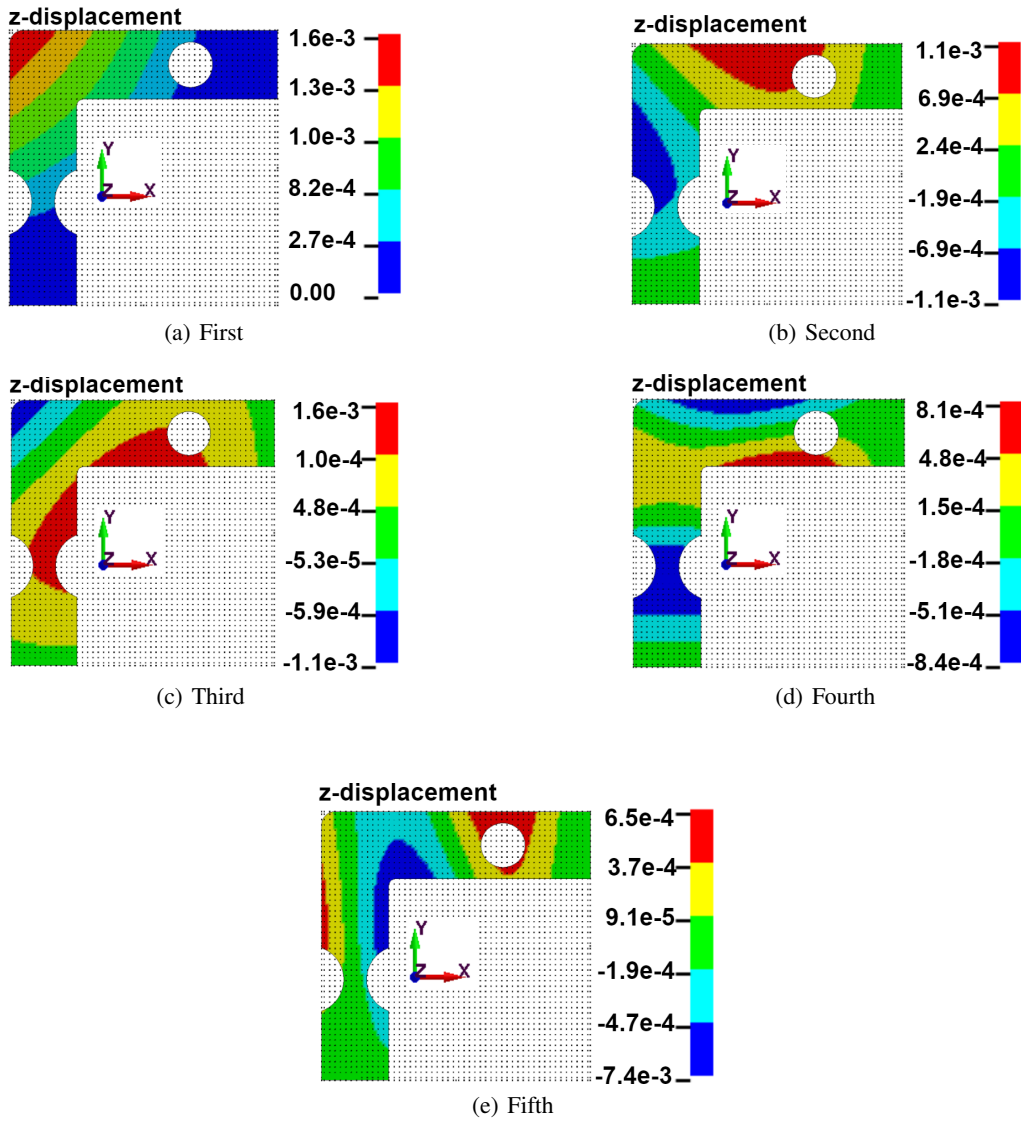


Figure 3.21: Isogeometric first five vibration modes

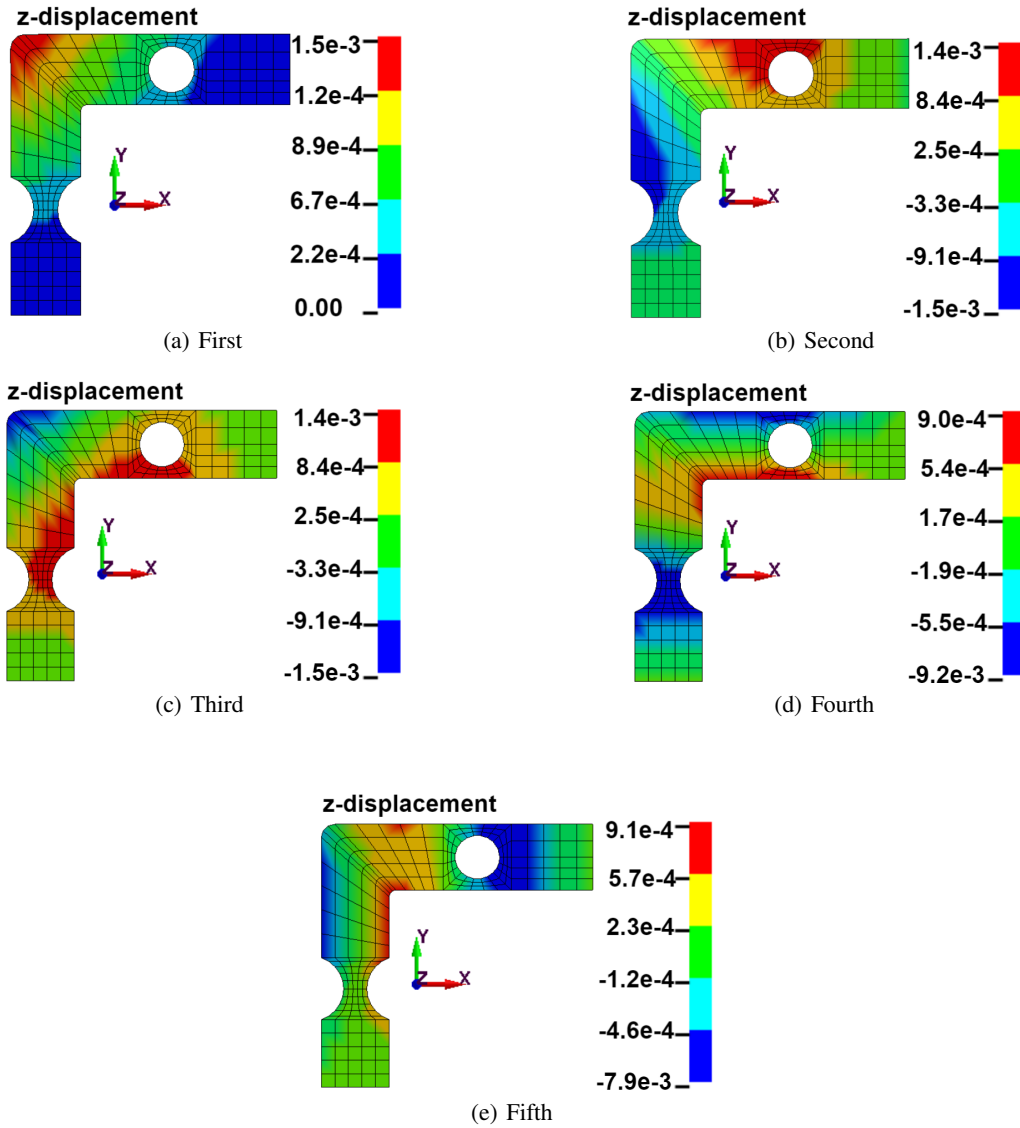


Figure 3.22: Finite element first five vibration modes

- II) Fatigue analysis results: effective stress PSD, RMS, and cumulative damage ratio

The acceleration PSD depicted in Fig. 3.23 is applied on control points in the z -direction to simulate the base acceleration. The damping ratio and exposure time are respectively set to 0.035 and 12 seconds. The random vibration fatigue analysis is developed in Ls Dyna to obtain the effective stress PSD, RMS, and cumulative damage ratio. Then based on obtained PSD, the cumulative damage ratios are validated in Matlab.

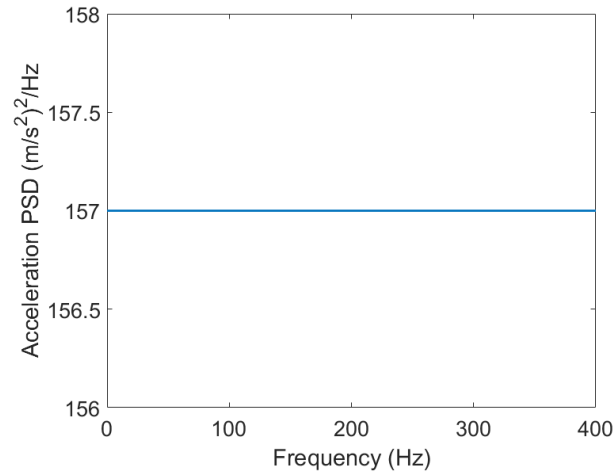


Figure 3.23: Applied load PSD

Figs. 3.24 and 3.25 show the obtained isogeometric and finite element effective stress PSD and RMS. It can be seen that only the first natural frequency is excited by the acceleration PSD. The obtained isogeometric and finite element PSD and RMS are similar. The maximum effective stress RMS obtained from IGA and FEA is $1.919\text{e}+8$ and $1.921\text{e}+8$ pa respectively, leading to the relative error of -0.10%. From Fig. 3.26, it can be seen that the obtained isogeometric and finite element cumulative damage ratios are respectively $7.571\text{e}-3$ and $7.341\text{e}-3$, leading to the relative error of 3.13%. The maximum damage ratios were located on similar elements. According to the Eq. (1.29), the expected isogeometric and finite element fatigue life $E[T_f]$ are $1.5850\text{e}+03$, and $1.6347\text{e}+03$ seconds respectively. Based on own developed Matlab programming, the isogeometric and finite element damage ratios are $7.6\text{e}-03$ and $7.4\text{e}-03$, which have a good agreement to the damage ratios obtained from Ls Dyna.

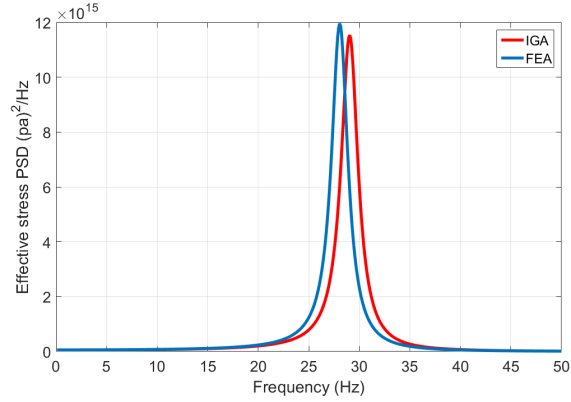


Figure 3.24: Effective stress PSD

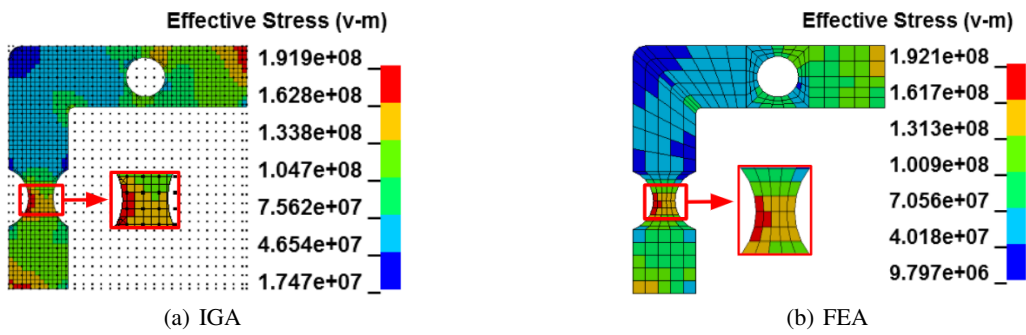


Figure 3.25: Effective stress RMS

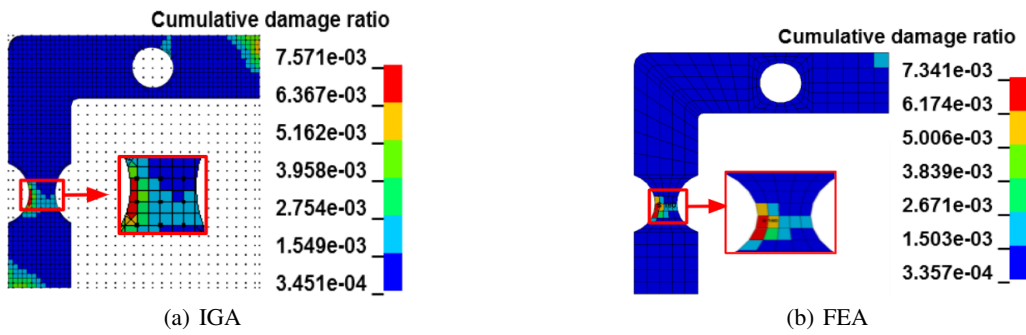


Figure 3.26: Cumulative damage ratio

3.3.3 Summary

In this part, the isogeometric and finite element convergence and random vibration fatigue analyses were developed on the L-shaped plate model, in which the obtained frequencies were compared with the ones from Pitoiset [5], and fatigue analysis results were validated by the Matlab programming.

In convergence analysis, the plate is clamped on the two edges (see Fig. 3.3), and based on obtained first natural frequency, the convergence points are decided. The results show that the IGA and FEA convergence analyses predict

similar modal analysis results. The isogeometric and finite element first natural frequency agree very well with the relative error of 1.15%. On the other hand, the obtained first natural frequencies from IGA and FEA are close to the one from Pitoiset, and the values are respectively 28.96, 28.63, and 27.7 Hz.

In fatigue analysis, a random vibration acceleration in the vertical direction to the plate surface is applied on the clamping fixture to simulate the base acceleration. The simulation results show that the obtained maximum RMS and cumulative damage ratios from IGA and FEA have a good agreement, with the relative errors of -1.03%, 3.1% respectively. Based on the Matlab program, the predicted isogeometric and finite element damage ratios are $7.6e-03$ and $7.4e-03$, which are close to the damage values calculated from Ls Dyna, $7.571e-3$ and $7.314e-3$.

3.4 Conclusion

This chapter considered the static, convergence, and random vibration fatigue analysis on the two different models based on IGA and FEA. For the specimen with reduced section model, an experimental test and Matlab program are developed to check the fatigue analysis results. For the L-shaped plate, the isogeometric and finite element damage results are validated by the Matlab program.

For the plate model with reduced section, the model is clamped from one side during simulation, and random acceleration in a vertical direction to the plate surface is applied to the clamping fixture. Numerical simulations are verified by convergence analysis on the static bending problem. It is shown that the IGA and FEA convergence analyses lead to similar maximum stress values with a relative error of 0.75%, situating at similar locations of the reduced section. The CPU time of the analysis, respectively 231 and 462 seconds, leading to the time difference of 50%, show that IGA is more time-efficient than FEA. The obtained first five natural frequencies and vibration modes have a good agreement. Fatigue analyses show that the obtained isogeometric and finite element maximum effective stress RMS are $5.24e+7$ and $5.278e+7$ pa with a relative error of -0.72%, and the cumulative damage ratios are 1.449 and 1.467 with a relative error of 1.2%. Based on the Matlab program, the isogeometric and finite element damage are respectively 1.435 and 1.481. Thus, the damage comparison between IGA and FEA, numerical simulation, and Matlab programming shows that the obtained values agree very well. On the other hand, the fatigue life from the experimental test, 3:30:00 (hours: minutes: seconds), has a good agreement with the isogeometric and finite element fatigue life from LS Dyna, 3:27:02 and 3:24:30 under $S_f = 612.3$ Mpa.

In the case of complex structures, the L-shaped plate model is clamped on two edges, and random acceleration in a vertical direction to the plate surface is applied to the clamping fixture. Based on obtained first natural frequencies, the convergence points are decided, and obtained frequencies are compared with those from Pitoiset. It can be observed that the IGA and FEA convergence analyses predict similar results, the first natural frequencies from IGA and FEA are respectively 28.96 and 28.63 Hz, leading to a relative error of 1.1%, which agree well with the first natural frequency from Pitoiset of 27.7 Hz. Fatigue analyses show that the obtained isogeometric and finite element maximum effective stress RMS are $1.919e+8$ and $1.921e+8$ pa with a relative error of -1.03%, and cumulative damage ratios are $7.571e-3$ and $7.314e-3$ with a relative error of 3.1%. Based on the Matlab program, the isogeometric and finite element damage are $7.6e-3$ and $7.4e-3$, leading to the relative error of 2.7%. Thus, the damage comparison between IGA and FEA, numerical simulation, and Matlab programming shows that the obtained values agree very well.

On the other hand, from the convergence analysis of these models, the numerical model development highlighted that for IGA during each mesh refinement step, it is not necessary to create mesh elements on the original geometry model. It is sufficient to develop mesh elements on the previous mesh model so that the mesh refinement time can be essentially saved. However, for the FEA, it is mandatory to communicate with the original geometric model for mesh refinement, and so this process was more time-consuming in LS Dyna software.

Chapter 4

Wind Turbine Tower optimization

4.1 Introduction

The aim of this chapter is to demonstrate the possibility of the developed modelling to increase the fatigue life of the realistic industrial structures through the shape optimization. The isogeometric random vibration fatigue analysis and design optimization are developed on a wind turbine tower model. The analysis results are verified by the FEA and Matlab programming. As shown in Fig. 4.1, this chapter mainly consists of three sections. In Section 4.2, a random force load is applied on the top concentrated mass node of the tower model to simulate the random vibration fatigue analysis. In Section 4.3, the isogeometric size optimization is considered with the design variables of the tower segment thicknesses, and the design objective is the direct maximization of the first natural frequency. In Section 4.4, the isogeometric shape optimization is fulfilled with the design variables of the control point position, in which the design objectives are respectively the direct maximization of the first natural frequency and direct minimization of the effective stress RMS. To obtain a regular door shape, in this case, only two control points are fixed. On the other hand, to furtherly investigate the different door shapes on the effects of effective stress, the shape optimization is also developed under the consideration of four fixed control points.

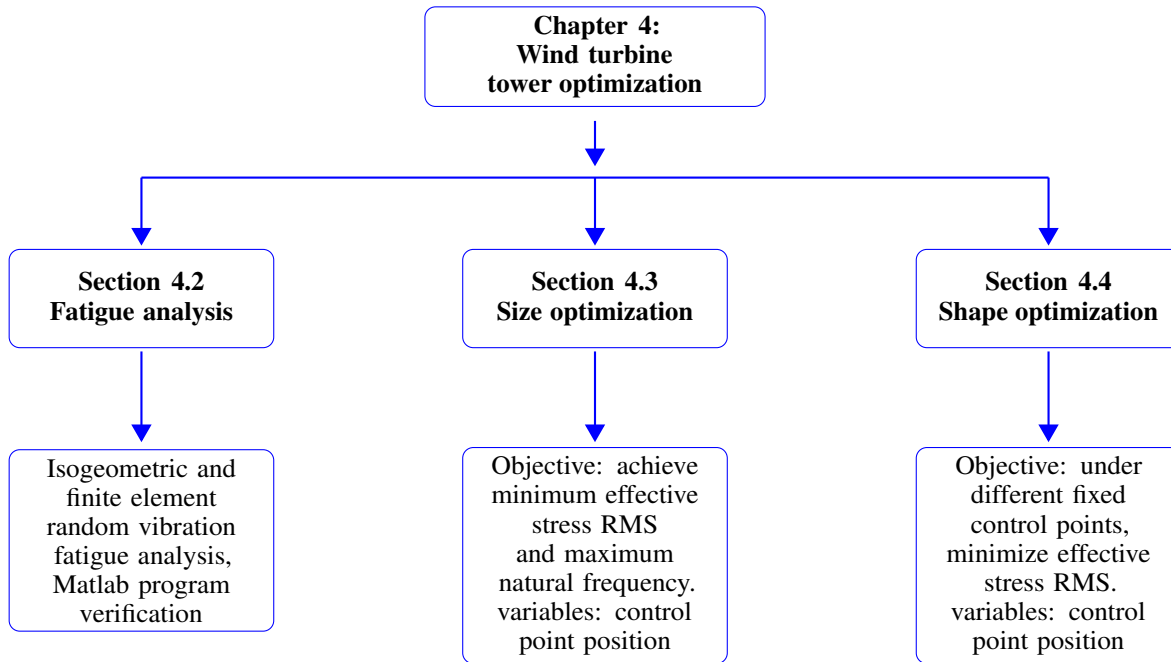


Figure 4.1: Schematic illustration of the fourth chapter

4.2 Random vibration fatigue analysis

A three-bladed wind turbine tower is chosen as a reference to develop IGA on an actual industrial model. The layout and main parameters of the tower model with the height of 38 m and power production of 450 kW are presented in Fig. 4.2 and Tab. 4.1, respectively.

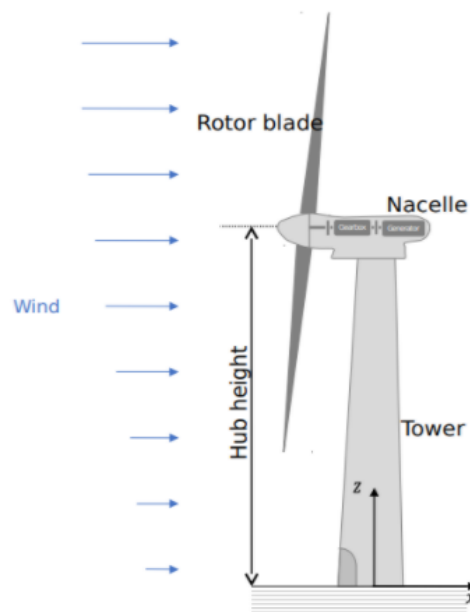


Figure 4.2: Layout of a 45 KW wind turbine tower with a height of 38 m

Table 4.1: Main parameters of the wind turbine tower

| Item | Value |
|-------------------------------------|----------|
| Rated power(KW) | 450 |
| Number of blades | 3 |
| Tower height(m) | 38 |
| Tower top diameter(m) | 1.82 |
| Tower bottom diameter(m) | 2.8 |
| Rotor and nacelle assembly mass (g) | 4.023e+7 |

- I) Analysis preparation

1) Geometric model, and material properties

The wind turbine tower model is created by a series of different thickness cylinders and conical shell sections, in which the geometry parameters such as the height, thickness, etc. are respectively displayed in the form of mm in the Fig. 4.3. The tower model is assembled by five flange connections, whose base, second, third, fourth, and top flange thicknesses are 330, 200, 200, 200, and 110 mm. At the base of the tower, a door opening is taken into account. The detailed geometrical information can be found in the reference [97].

The tower material properties are shown in Tab. 4.2. The material constants σ_f and b of the Basquin's equation are respectively 612.3 MPa and -0.105, obtained from CES EduPack™.

Table 4.2: Material properties

| Mass density | Young's modulus | poisson's ratio |
|---------------------------|-----------------|-----------------|
| 7.85e-3 g/mm ³ | 1.7e+11 Pa | 0.3 |

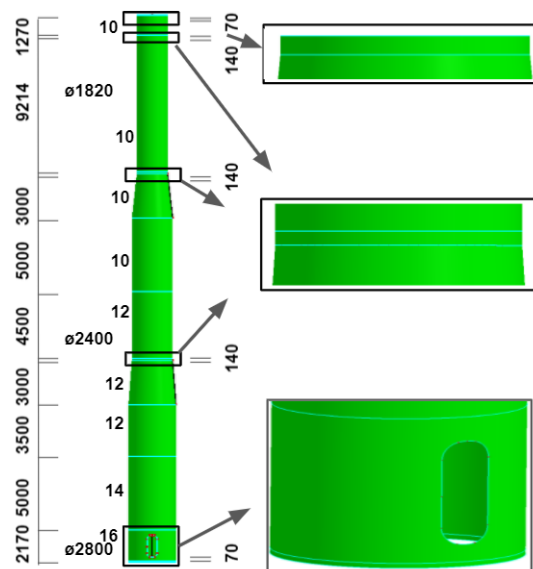


Figure 4.3: Geometric model (in mm)

2) Mesh models and boundary condition

The isogeometric and finite element mesh models are presented in Fig. 4.4 in which the number of control points and nodes are respectively 6724 and 23227. For IGA, as at present, NURBS solid elements are not implemented in Ls Dyna, we implement the isogeometric NURBS shell elements for all flange and cylinder sections (see Fig. 4.4 (c)), and adopt Hughes-Liu with rotational DOFs shell formulation; the polynomial order of univariate shape functions in s and r -directions in the parametric space is 2, and in Ls Dyna, the mesh refinement method, SUBDIVISION, is used to refine the mesh models. After mesh generation on each section, the keyword, NODE DUPLICATION, is used to merge control points (nodes for FEA) to assemble the different sections.

For FEA, the finite element mesh model is described by quadrilateral four nodes mesh elements. The shell element formulation of Hughes-Liu is chosen for the cylindrical and conical sections. The flange created by solid elements is connected with shell sections through the keyword, NODE DUPLICATION in Ls Dyna (see Fig. 4.4 (c)).

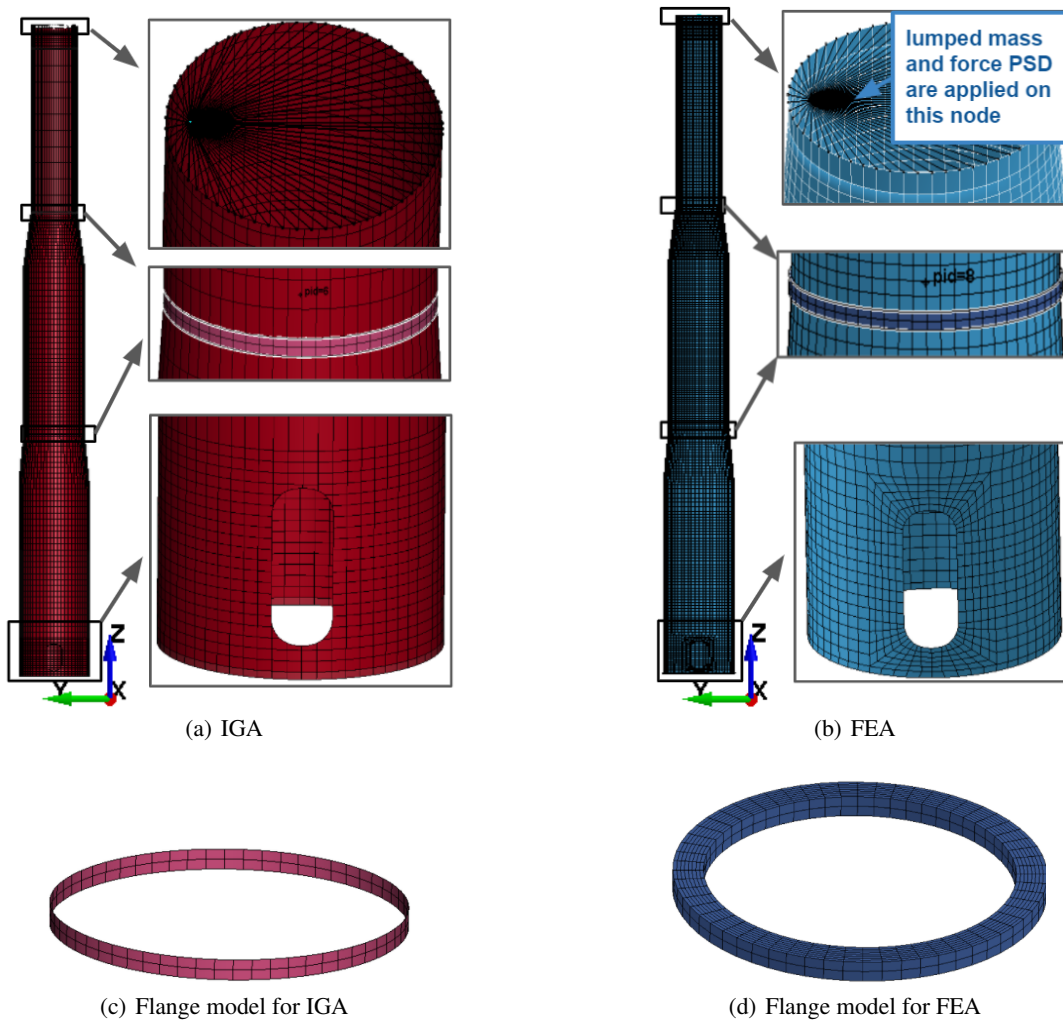


Figure 4.4: Mesh models

To simulate the weight effects, at the height of of the tower model $Z = 3.708e+04$ and $X = -750, Y = 0$ mm, a node is created to substitute the concentrated mass element, $4.023e+7$ g. Then the node is connected with all control points (or nodes for FEA) of the top flange edge, and the weight direction is set to in negative z -direction. The aerodynamic load-force PSDs, as shown in Fig. C.5 is applied on the node substituting the element concentrated mass in the x, y, z directions. The random vibration fatigue analysis of 600 seconds (10 minutes), in which the damping ratio is set to 0.01, is developed to calculate the effective stress PSD, RMS, and cumulative damage ratio in Ls Dyna. Then based on obtained PSD, the cumulative damage ratio is validated in Matlab using a self-developed program. During analysis, the base flange of the tower model is clamped in the translational and rotational local x, y, z -directions.

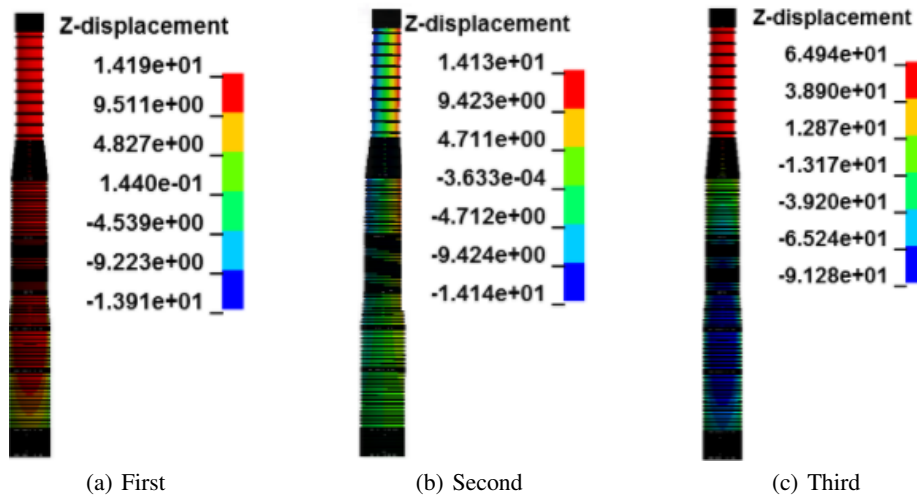
- II) Analysis results

- 1) Modal analysis results: the first five natural frequencies and vibration mode

Tab. 4.3 shows the first five natural frequencies obtained from IGA and FEA, from which it can be seen that the values have a good agreement. Figs. 4.5 and 4.6 respectively display the first five vibration modes computed from IGA and FEA. Through comparison, it can be found that the first five vibration modes are almost the same, in which the first vibration mode is bending.

Table 4.3: The first five natural frequencies (Hz)

| Method | 1 | 2 | 3 | 4 | 5 |
|--------|------|------|------|------|-------|
| IGA | 0.68 | 0.70 | 6.56 | 6.74 | 13.16 |
| FEA | 0.68 | 0.69 | 6.63 | 6.82 | 12.82 |



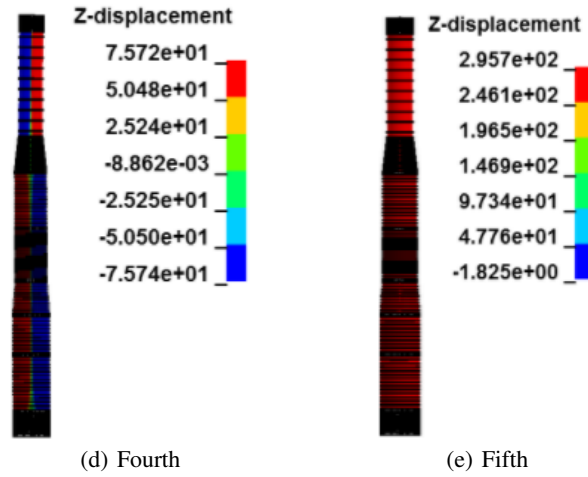


Figure 4.5: Isogeometric first five vibration modes

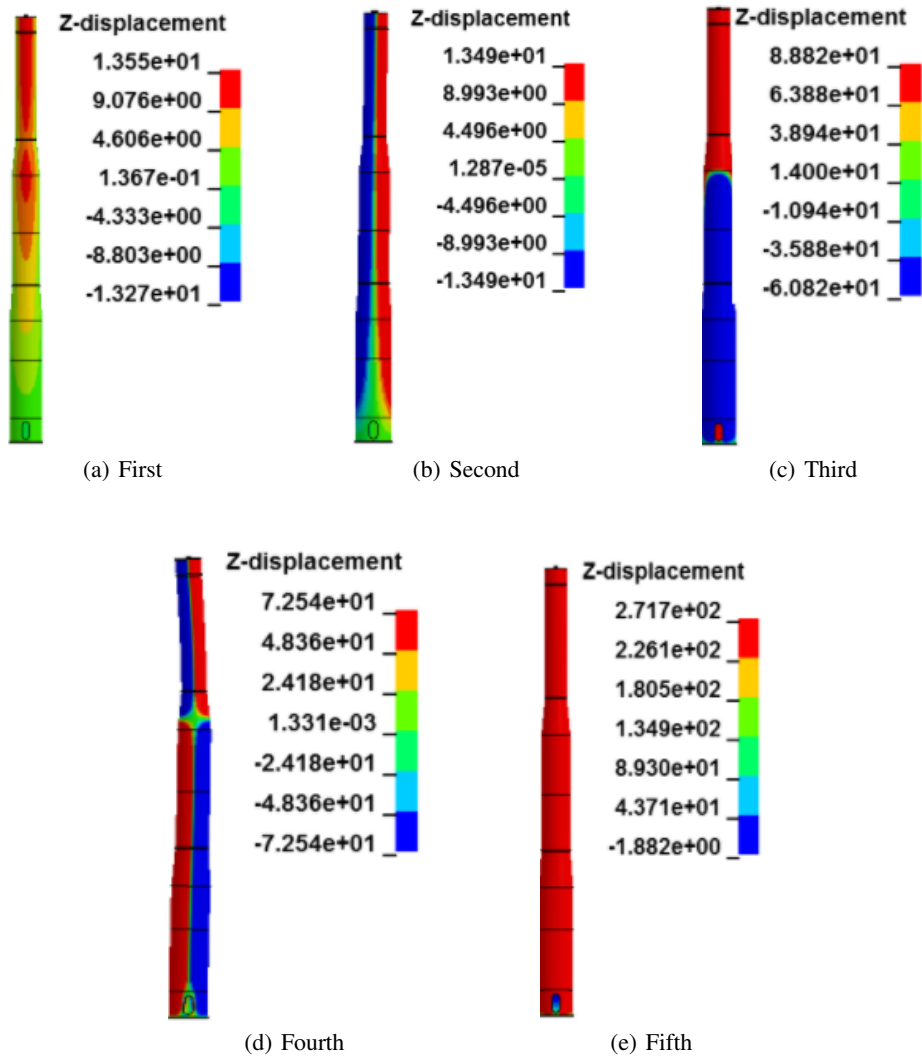


Figure 4.6: Finite element first five vibration modes

2) Fatigue analysis results: effective stress PSD, RMS and cumulative damage ratio

Figs. 4.7 and 4.8 present the calculated isogeometric and finite element effective stress PSD and RMS, in which only the first natural frequencies are excited by the applied force PSDs. It is observed that isogeometric and finite element PSD and RMS display a good agreement. The maximum effective stress RMS from IGA and FEA is 70.62 and 72.39 pa respectively, leading to the relative error of -2.45%. From Fig. 4.9, it can be seen that the obtained isogeometric and finite element cumulative damage ratios are respectively $4.178e-5$ and $4.112e-5$, with a relative error of 1.61%, and the maximum damage ratios are located on similar elements close to the door edge. According to the Eq. 1.29, the expected isogeometric and finite element fatigue life $E[T_f]$ are $1.4361e+07$ and $1.4591e+07$ seconds respectively. Based on the Matlab program, the isogeometric and finite element damage ratios are respectively $4.2e-05$, which are in good accordance with the damage ratios computed from Ls Dyna.

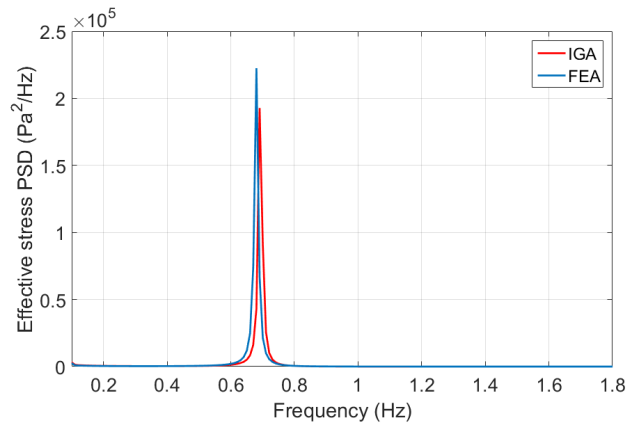


Figure 4.7: Effective stress PSD

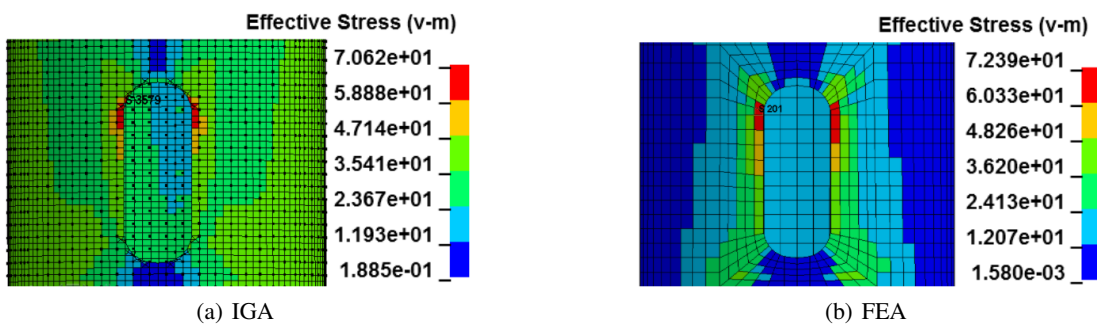


Figure 4.8: Effective stress RMS

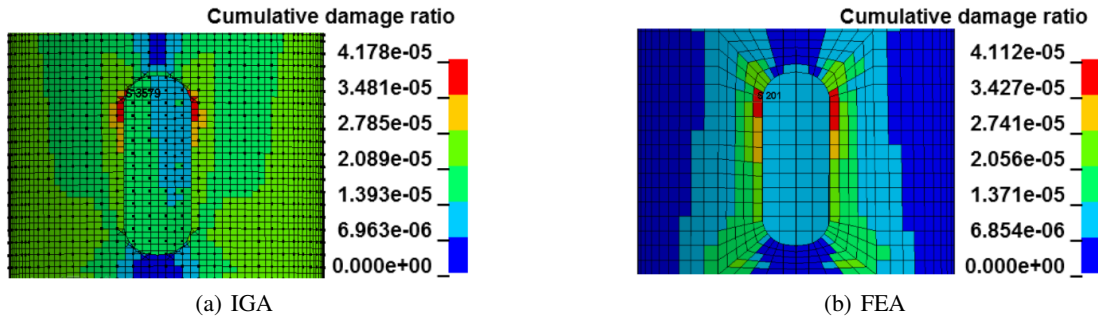


Figure 4.9: Cumulative damage ratio

- III) Summary

In this part, isogeometric and finite element random vibration fatigue analyses were developed on the tower model, in which the fatigue analysis results were validated by the Matlab programming.

During analysis, the tower was clamped on the base flange. From modal analysis results, it can be found that the isogeometric and finite element first natural frequencies are the same.

In fatigue analysis, longitudinal, lateral, and vertical random vibration force PSDs in the x, y, z directions to the tower model were applied on the concentrated mass node. The results show that firstly, the obtained maximum effective stress RMS and cumulative damage ratios have a good agreement, with the relative errors of -2.45%, and 1.61% respectively; secondly, based on the Matlab program, the predicted isogeometric and finite element damage ratios are respectively $4.2e-5$, which are close to the damage values calculated from Ls Dyna, $4.178e-5$ and $4.112e-5$. The damage is located near the door, thus providing the directions for the following shape optimization.

4.3 Sizing optimization

The mathematical formulation of a structural design optimization can be stated as [98]:

$$\begin{aligned} & \text{find} \quad \underline{\mathbf{x}} \\ & \text{minimize} \quad f(\underline{\mathbf{x}}) \\ & \text{subject to} \quad g(\underline{\mathbf{x}}) = 0 \text{ and } h(\underline{\mathbf{X}}) \geq 0 \end{aligned} \tag{4.1}$$

where $\underline{\mathbf{x}} = (x_1, x_2, \dots, x_n)$ is the design variable with a set of components, $f(\underline{\mathbf{x}})$ is the objective function, $g(\underline{\mathbf{x}})$ and $h(\underline{\mathbf{x}})$ are the constraint functions.

4.3.1 Analysis preparation

- I) Basic assumptions

The tower model assembled by a series of the cylinder and conical shell segments have different thicknesses. To reduce the dimensionality in the optimization problem, the following variables will be considered fixed:

- 1) tubular tower configuration
- 2) the height and diameter of each segment
- 3) material properties, concentrated mass, etc.
- 4) some analysis parameters like shell element formulation, integration points, boundary condition, etc.

- II) Design objectives

Several tower design objectives existed, including lightweight design, high stiffness, high (stiffness/ mass)-ratio, etc. In this studying, we choose the direct maximization of the system's first natural frequency as the tower design objective, which is beneficial for the long fatigue life, high stability, low noise, etc.

- III) Design variables

The design variables are selected to be the thickness of the segments. For the tower model, there are four kinds of segment thicknesses ($t_i, i = 1, 2, 3, 4$), that are respectively 16, 14, 12, 10 mm, in which we only considered the effects of thicknesses 16 and 14 mm on the first natural frequencies.

- IV) Design constraints

The design constraints are in terms of mass and thickness.

- 1) Mass limitations

$$M_l \leq M \leq M_u \tag{4.2}$$

where M_u and M_l are respectively allowable upper and lower limiting value of the tower mass. For the size optimization, the values are respectively $6.8605E + 07 \leq M \leq 6.9475E + 07$ (g)

2) Side constraints

$$t_{il} \leq t \leq t_{iu}, \quad i = 1, 2 \quad (4.3)$$

where t_{iu} and t_{il} are respectively allowable upper and lower limiting value of the i th thickness. In this studying, the values are respectively $15 \leq t_1 \leq 17$ and $13 \leq t_2 \leq 15$ mm.

- V) Optimization procedures

There are three main steps for wind turbine size optimization, as shown in Fig. 4.10. The first step, read the original k file created by Ls Dyna, and use Matlab to produce k files with different design variables. The second step, compute each created k file by Ls Dyna based on Matlab running and save the desired values like natural frequencies from analysis results. The third step, plot the figure of obtained natural frequencies, design variables, and design constraints, from which an optimum value can be determined.

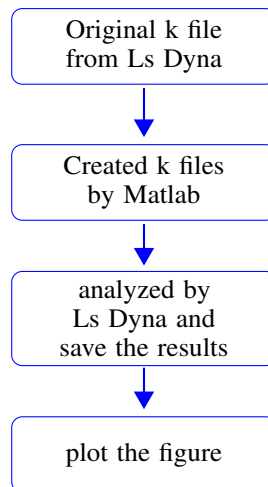


Figure 4.10: Sizing optimization procedures

4.3.2 Sizing optimization results

- I) Based on IGA

Fig. 4.11 (a) shows the variation of the first natural frequency under different segment thicknesses. With the consideration of mass constraint (see Fig. 4.11 (b)), it can be observed that the first natural frequency is maximum when the t_1 and t_2 are respectively 17 and 15 mm, and the maximum value is 0.6996 (Hz).

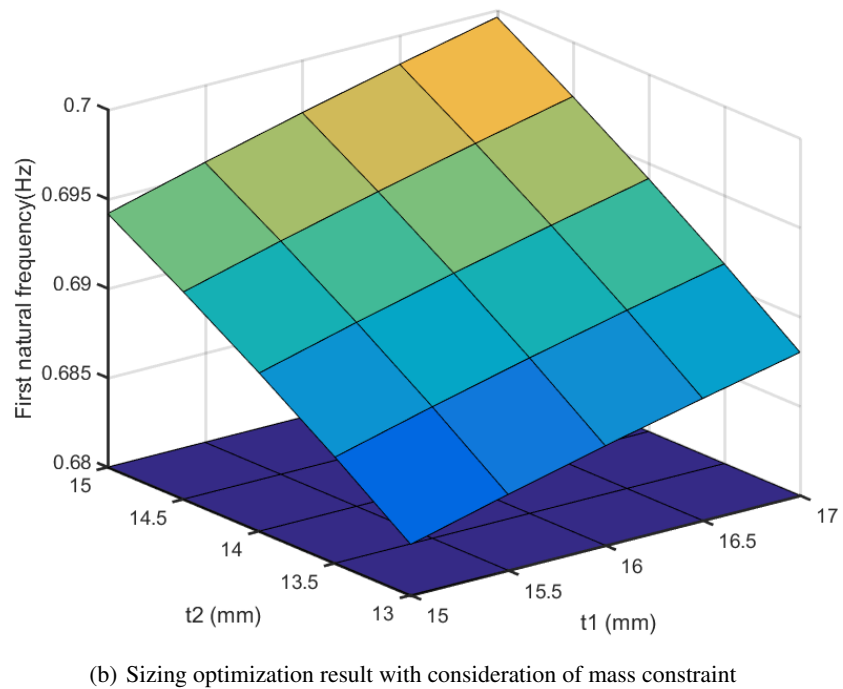
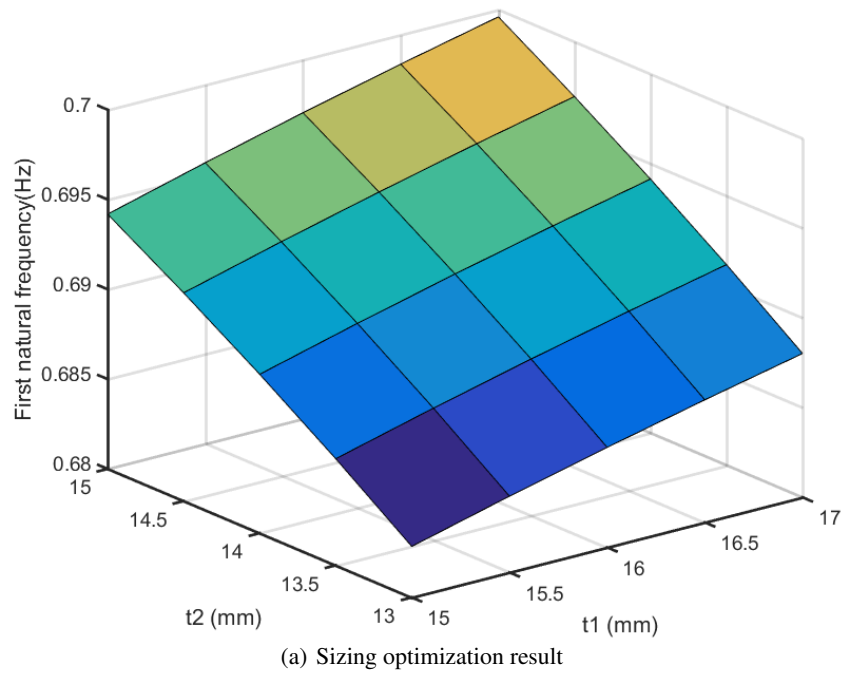
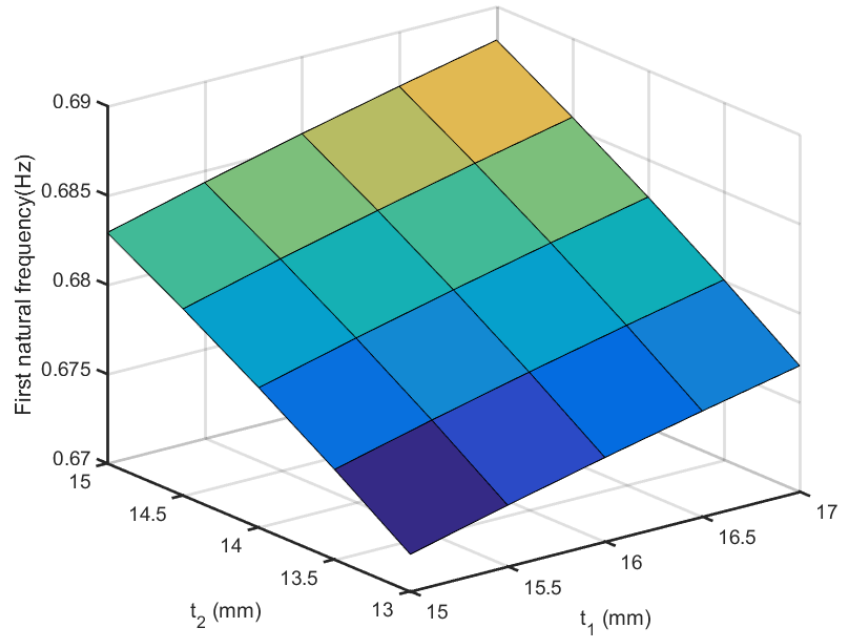


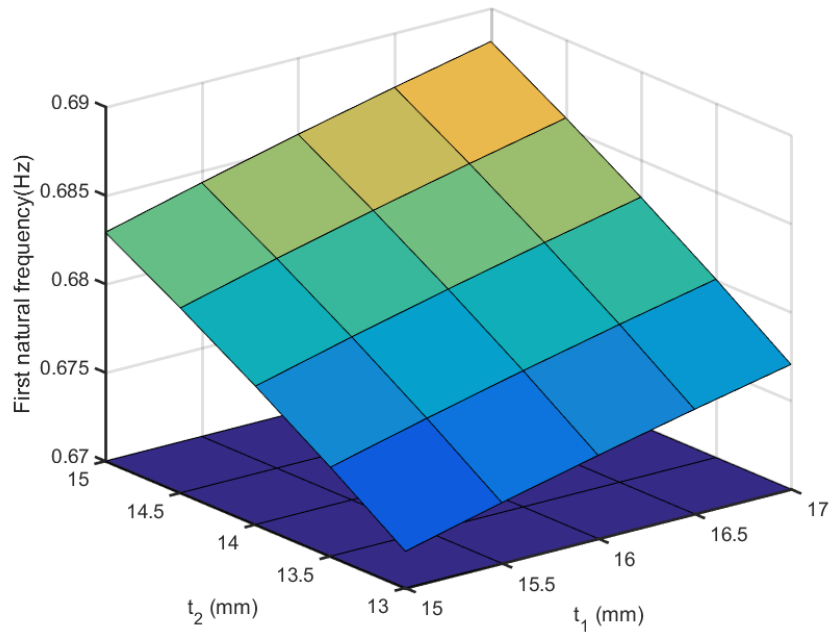
Figure 4.11: Isogeometric sizing optimization results

- II) Based on FEA

Fig. 4.12 (a) shows the variation of the first natural frequency under different segment thicknesses. Based on consideration of mass constraint (see Fig. 4.12), it can be observed that the first natural frequency is maximum when the t_1 and t_2 are respectively 17 and 15 mm, and the maximum value is 0.6881 (Hz).



(a) Sizing optimization result



(b) Sizing optimization result with consideration of mass constraint

Figure 4.12: Finite element sizing optimization results

4.4 The first shape optimization

4.4.1 Analysis preparation

The purpose is to find the optimal shape of the door, which will reduce the RMS stress and thus increase the service life of the wind tower. In IGA, the wind turbine door shape is controlled by the 10 NURBS curves (from 5 to 14), as shown in the Fig. 4.13 (a). To carry out the shape optimization, it is necessary to ensure that the control points connecting different NURBS curves should be the same. For example, for the NURBS curve 11 and 12, the curves are connected at the same control point, as shown in the Fig. 4.13 (b). During optimization, only the x coordinates of the control points are taken as variables to change the door shape, in which the central control point of the NUBRS curves 7 and 12 (see Fig. 4.13 (c)) are fixed to locate the door. The design constraint is only taken consideration on the mass values, as shown in the Eq. 4.2, in which the maximum M_u and minimum M_l mass values are respectively $6.9898E+07$ and $6.9708E+07$ (g).

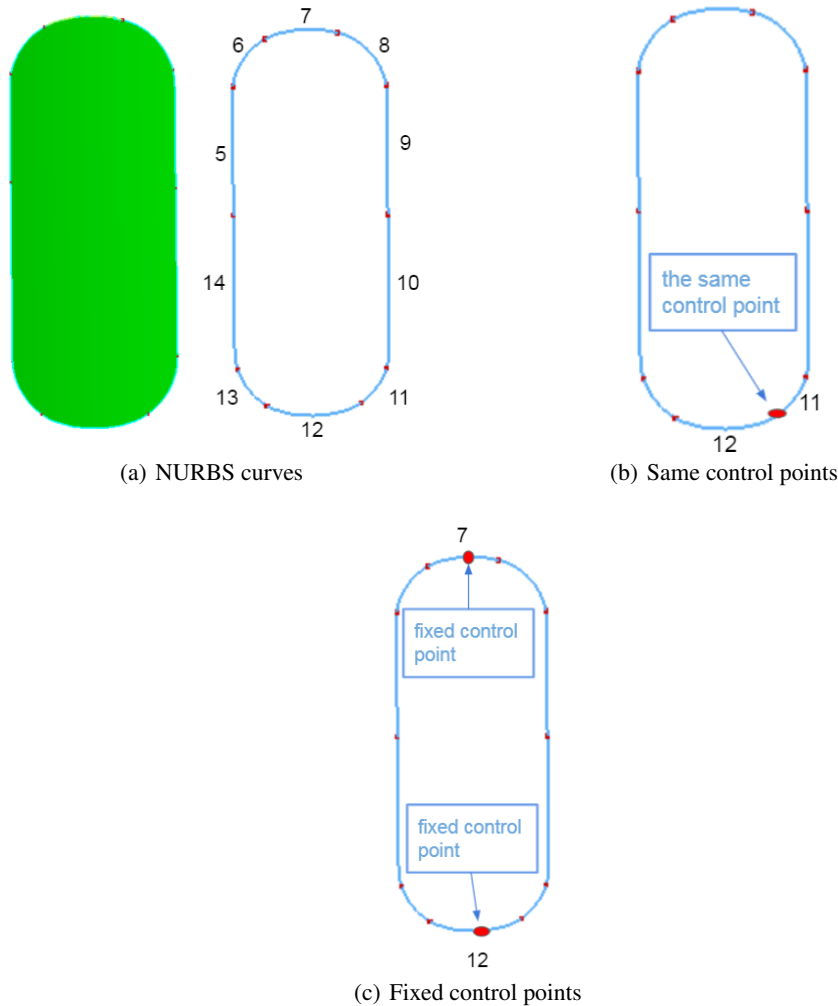


Figure 4.13: NURBS curves for the door

4.4.2 Shape optimization results

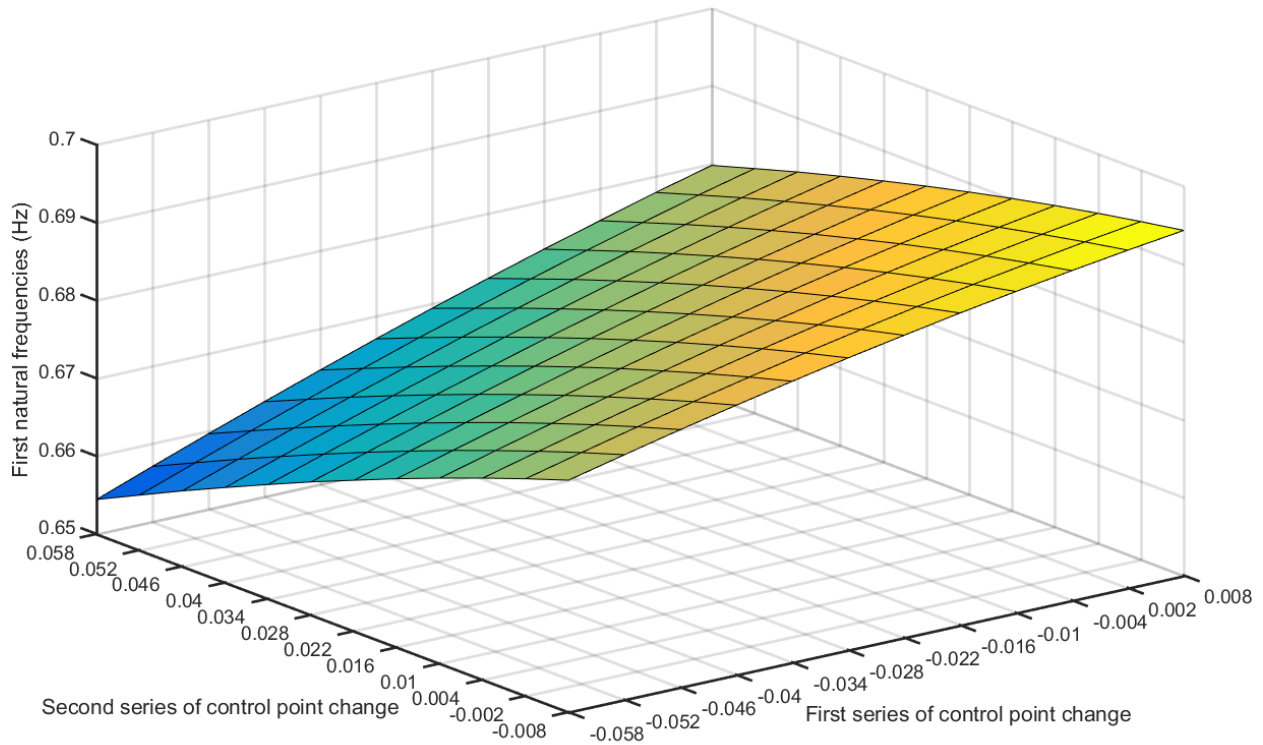
- I) With the design objective of maximum natural frequency

Fig. 4.14 (a) present the shape optimization results, in which the x, y labels respectively indicate the first and second series of control point change of NURBS curve 7, 6, 5, 14, 13, 12 and 7, 8, 9, 10, 11, 12 in parametric space; z label shows the obtained first natural frequencies under different door shapes. It can be seen that under the mass constraint (see Fig. 4.14 (b)), the maximum and minimum natural frequencies (Hz) are situated on the points (0.008, -0.002, 6.92e-1) and (-0.046, 0.058, 6.59e-1), marked by red diamonds in the Fig. 4.14 (c).

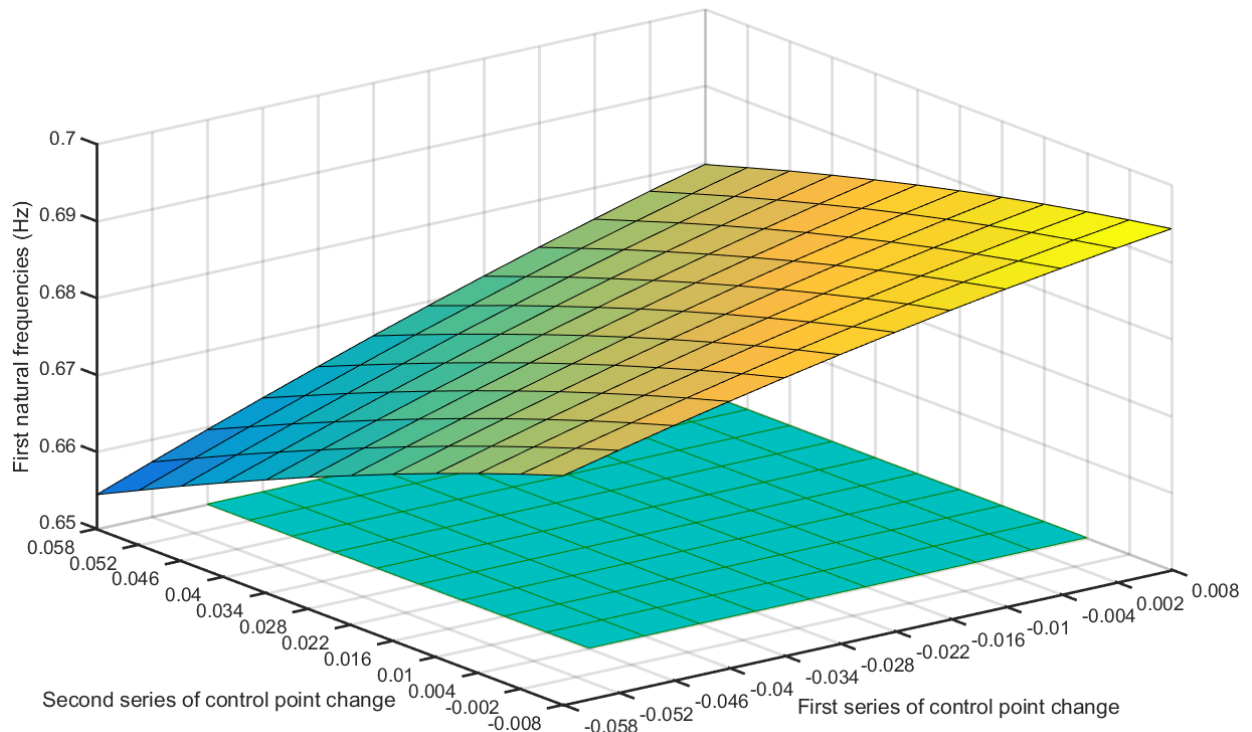
The obtained maximum, minimum, and original (no consideration of optimization) frequencies are displayed in the Tab. 4.4. When compared with the original state in terms of natural frequency, it can be found that through optimization, the natural frequency can be improved with a relative error of 1.76%.

Table 4.4: The first natural frequencies (Hz)

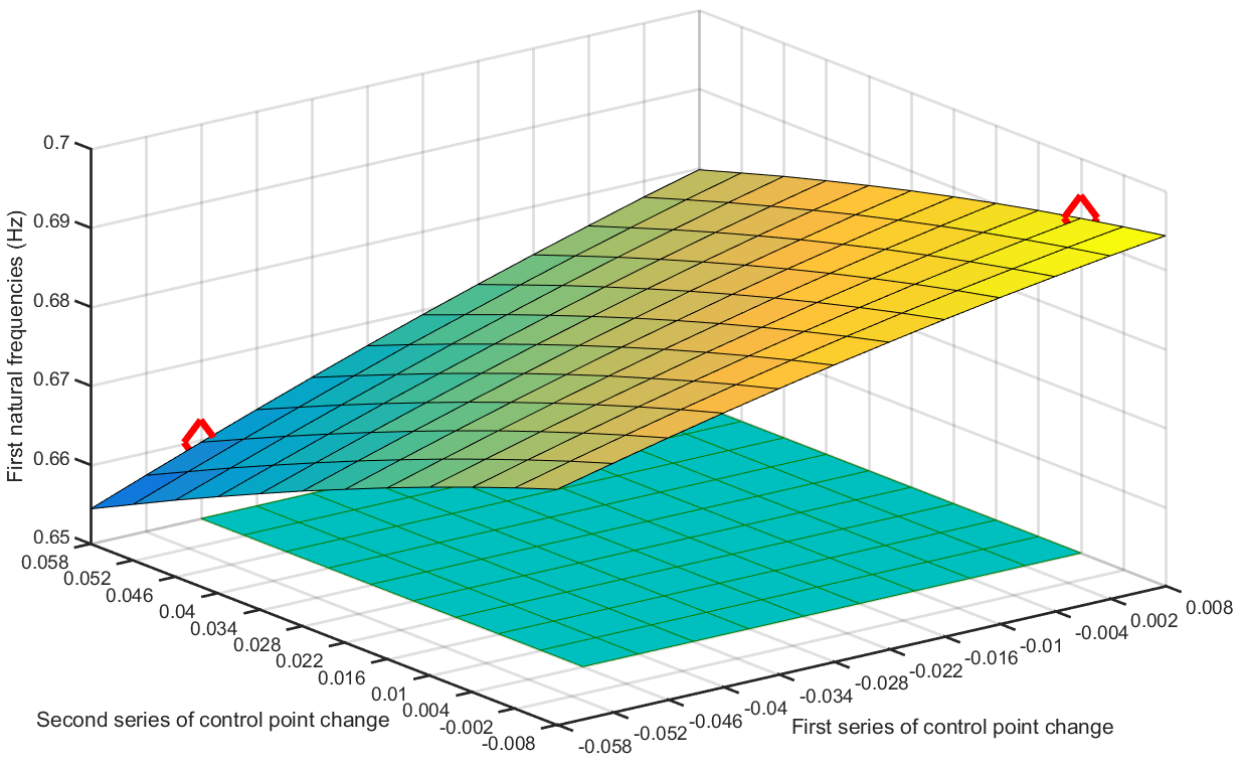
| Maximum | minimum | original |
|---------|---------|----------|
| 0.692 | 0.659 | 0.680 |



(a) Without constraint



(b) With mass constraint



(c) With mass constraint

Figure 4.14: Isogeometric shape optimization results

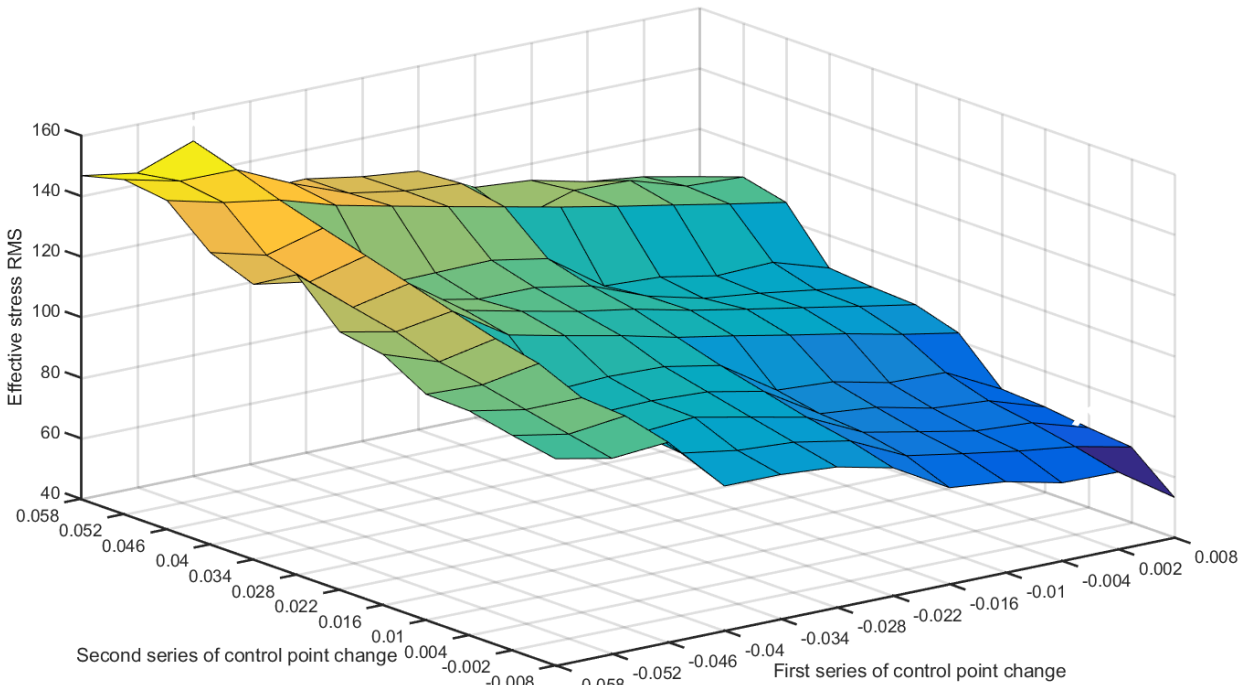
- II) With the design objective of minimum effective stress RMS

Fig. 4.15 (a) present the shape optimization results, in which z label shows the obtained effective stress RMS under different door shapes. It can be seen that under the mass constraint (see Fig. 4.16 (b)), the minimum and maximum effective stresses are situated on the points (0.008, -0.002, 6.633e+1) and (-0.046, 0.058, 1.505e+2), marked by red diamonds in the Fig. 4.15 (c).

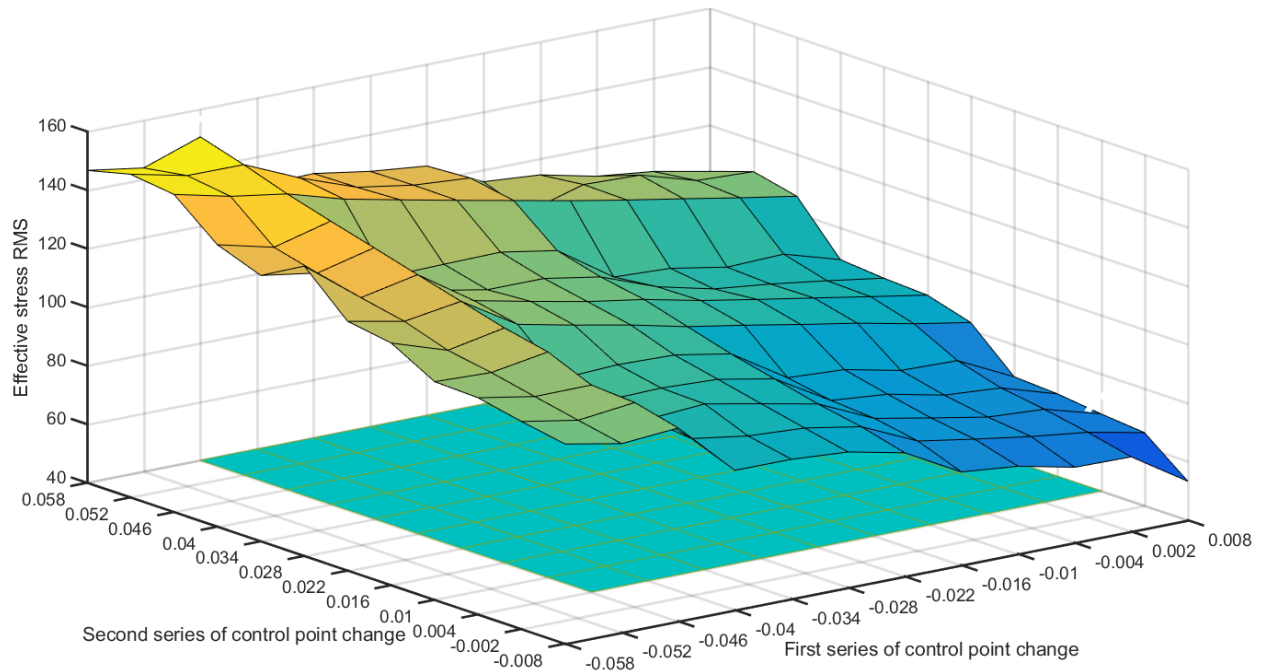
The obtained maximum, minimum, and original (no consideration of optimization) effective stress RMS are presented in Tab. 4.5. When compared with the original state in terms of natural frequency and stress values, it can be found that through optimization, the RMS can be reduced with a relative error of 6.07%, meaning that under the same applied load condition, based on material S-N curve, the optimized model have a longer fatigue life.

Table 4.5: The effective stress RMS

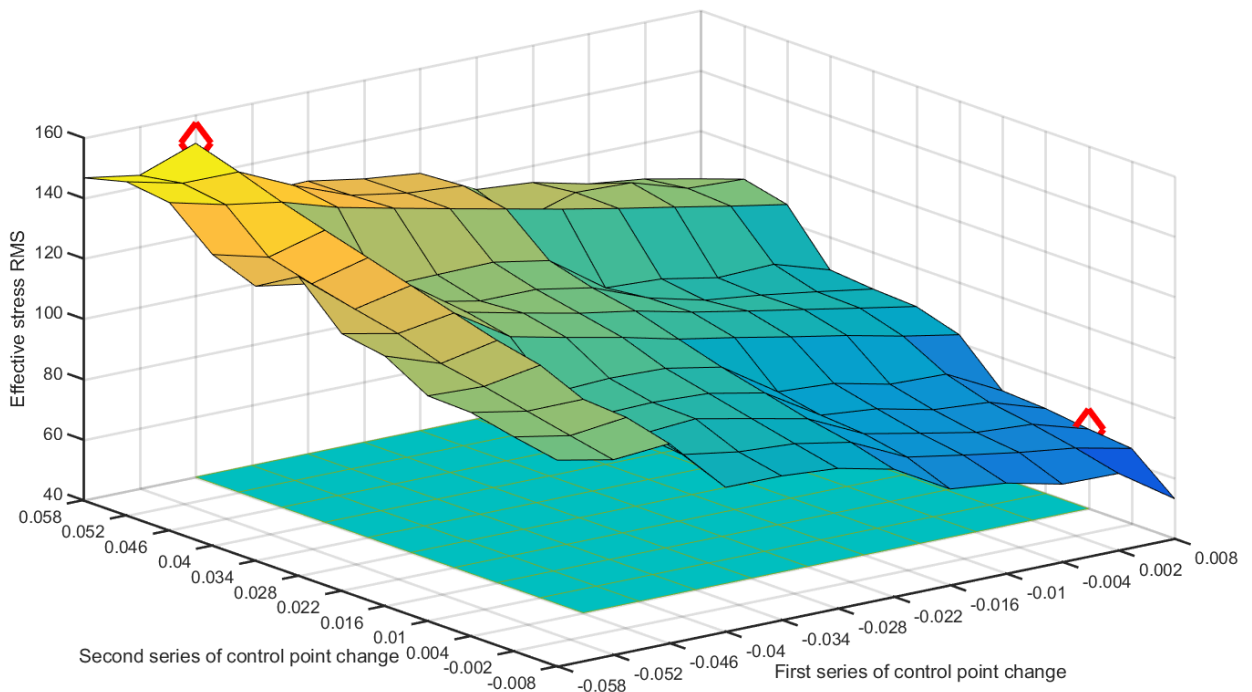
| Maximum | minimum | original |
|---------|---------|----------|
| 150.5 | 66.33 | 70.62 |



(a) Without constraint



(b) With mass constraint



(c) With mass constraint

Figure 4.15: Isogeometric shape optimization results

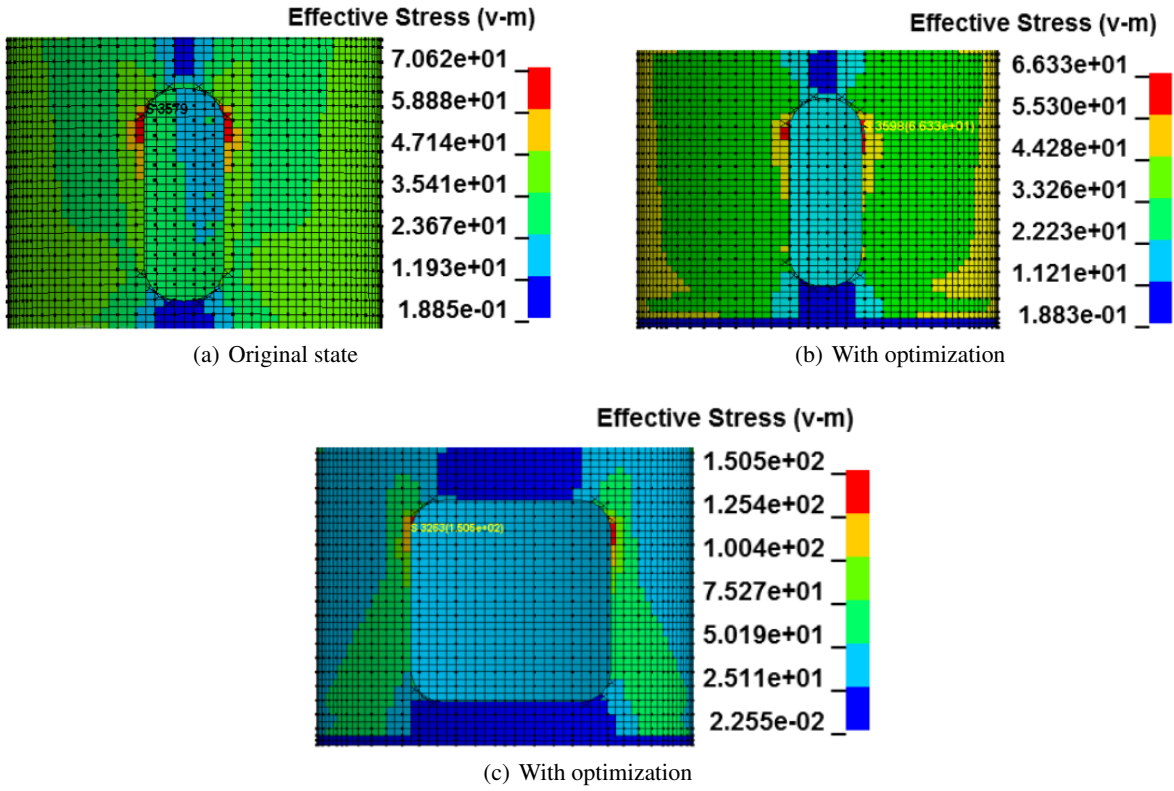


Figure 4.16: Isogeometric shape optimization results

4.5 The second shape optimization

4.5.1 Analysis preparation

The fixed four control points in optimization are shown in Fig. 4.17.

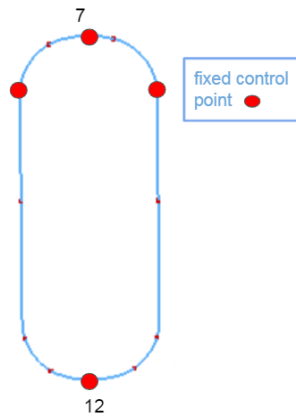


Figure 4.17: Illustration of fixed control points

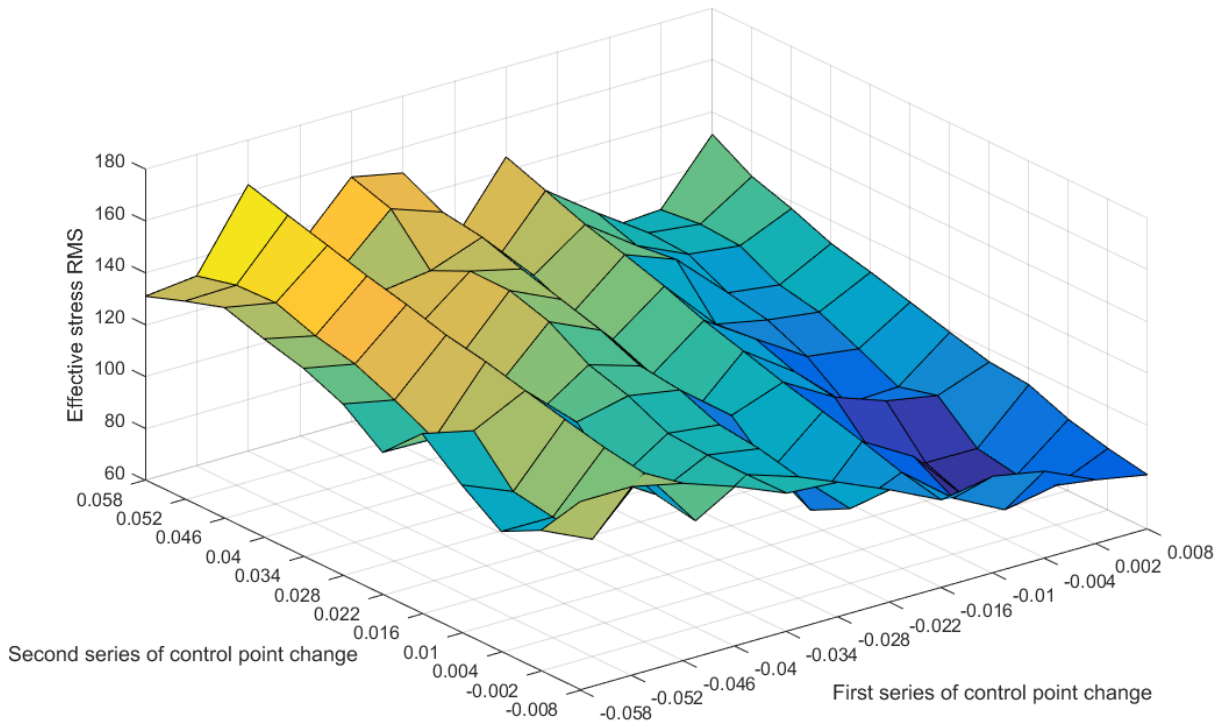
4.5.2 Analysis results

Fig. 4.18 (a) present the shape optimization results, in which z label shows the obtained effective stress RMS under different door shapes. It can be observed that under the mass constraint (see Fig. 4.18 (b)), the minimum and maximum effective stresses are situated on the points $(-0.004, 0.004, 6.884e+1)$ and $(-0.046, 0.058, 1.413e+2)$, marked by red diamonds in the Fig. 4.18 (c).

The obtained maximum, minimum and original (no consideration of optimization) effective stress RMS are presented in Tab. 4.6, and Fig. 4.19. When compared with stress values of original states, it can be found that through optimization, the RMS can be reduced with a relative error of 1.94%.

Table 4.6: The effective stress RMS

| Maximum | minimum | original |
|---------|---------|----------|
| 162.7 | 68.84 | 70.62 |



(a) Without constraint

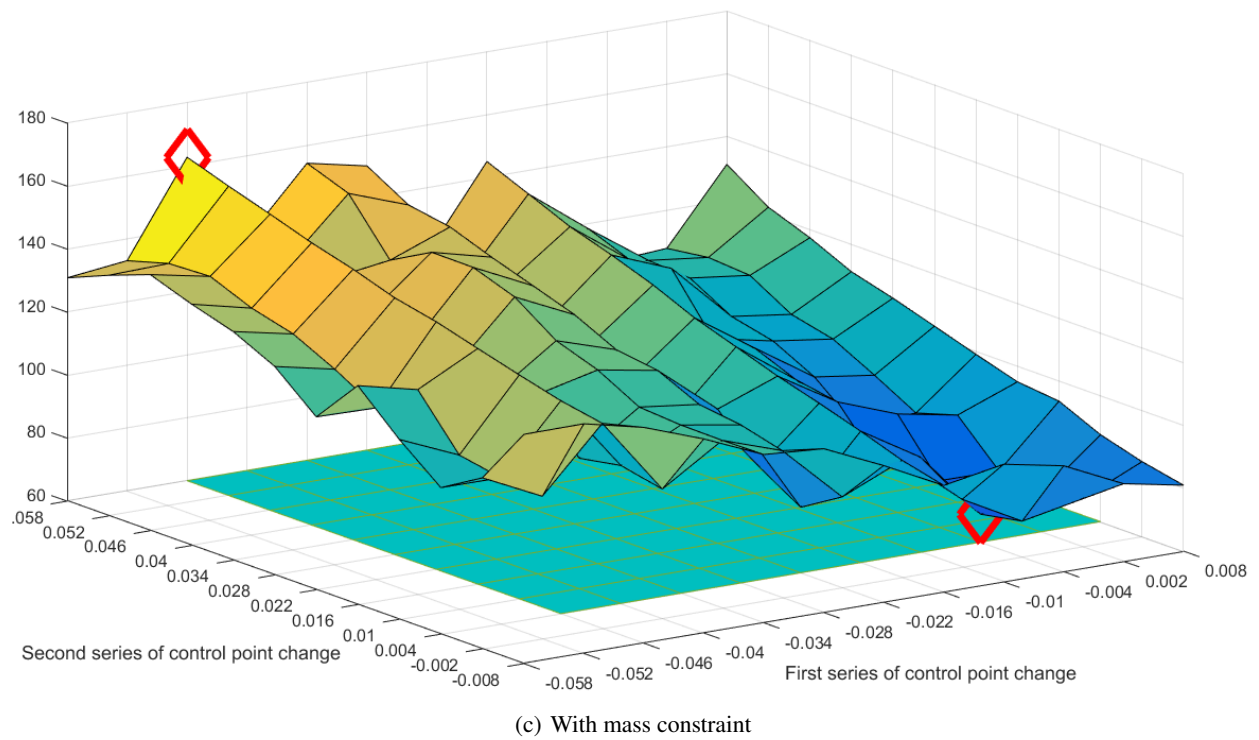
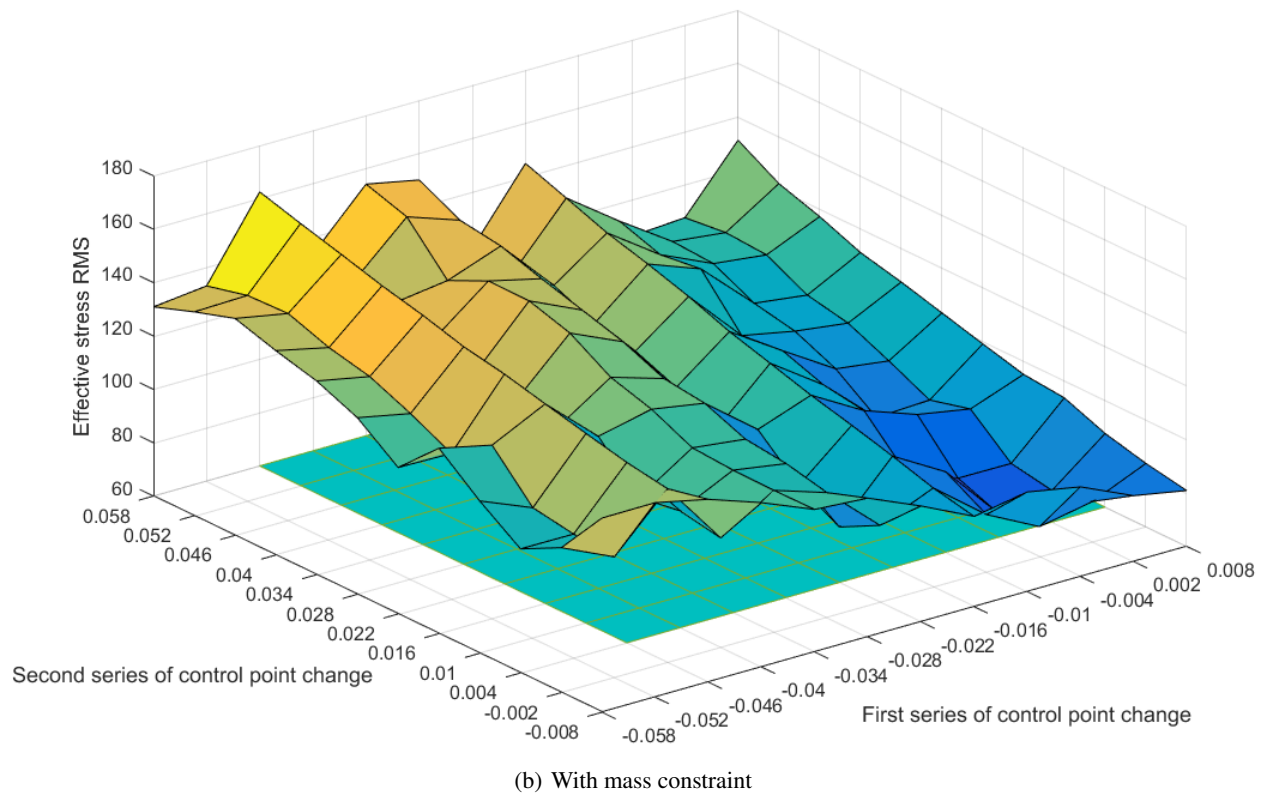


Figure 4.18: Isogeometric shape optimization results

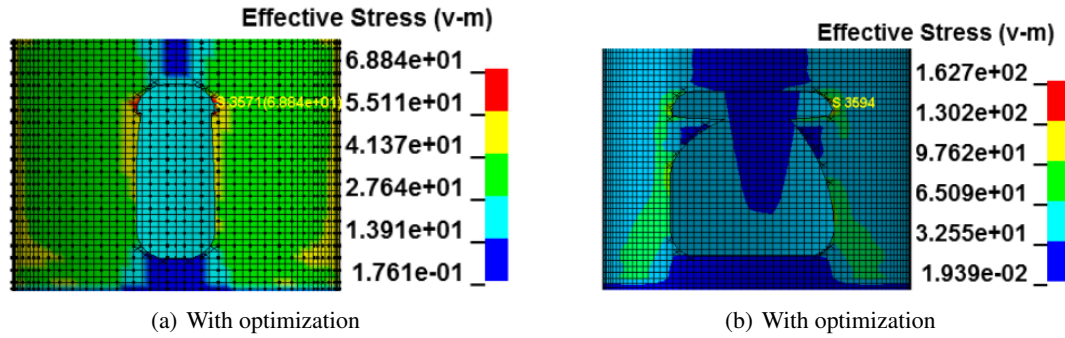


Figure 4.19: Isogeometric shape optimization results

4.6 Conclusion

In this chapter, the isogeometric random vibration fatigue analysis, size and shape optimizations were developed on the wind turbine tower model. The design objectives were the maximum first natural frequency and minimum effective stress RMS. The design variables were respectively the tower segment thicknesses and control point position of the NURBS curves.

For the fatigue analysis, the tower model was clamped on the base flange, and random force PSDs were applied on the concentrated mass element. From modal analysis, it can be found that the obtained first five natural frequencies and vibration modes from IGA and FEA have a good agreement. Fatigue analyses show that the obtained isogeometric and finite element maximum effective stress RMS are 70.62 and 72.39 pa with a relative error of -2.45%, and cumulative damage ratios are 4.178e-5 and 4.112e-5 with a relative error of 1.61%. Based on the Matlab program, the isogeometric and finite element damage are respectively 4.2e-5. Thus, the damage comparison between IGA and FEA, numerical simulation, and Matlab programming shows that the obtained values agree very well.

From the sizing and shape optimization results, it can be observed that the natural frequency can be improved to 0.6996 (isogeometric size optimization), 0.6881 (finite element size optimization), and 0.692 Hz (isogeometric first shape optimization) from the original value of 0.680 Hz. It can be seen that the design variables have fewer effects on the first natural frequency, however have significant effects the effective stress RMS, determining a structure's damage ratio. From the isogeometric shape optimization results, it can be found that under consideration of mass constraints, the effective stress RMS value can be reduced with relative errors of 6.07% and 1.94%. Furthermore, based on proper fixed control points, we can develop shape optimization considering different door shapes.

Chapter 5

Conclusions

In this studying, isogeometric static, convergence, fatigue, size and shape optimization are respectively developed, in which the static, convergence and fatigue analysis results are validated by FEA, and Matlab programming.

Firstly, from the aspect of mesh generation, it is obvious that IGA is time-efficient compared with FEA. Normally, in the FEA field, the more complex a geometry, the more time spent in mesh generation. For example, for the L-shaped and wind turbine tower model, in FEA, the mesh generation time occupies respectively 50% and 80% of whole analysis time; in IGA, almost 10%.

In terms of convergence analyses, compared with FEA, the IGA normally predict the results with the use of less elements and CPU time. For example, for the convergence analysis on the simple plate model, the CPU time are respectively 231 seconds (IGA) and 462 seconds (FEA).

From the fatigue analysis on plate and tower models, it can be found that IGA can provide similar fatigue life with FEA, normally using fewer control points (compared with the nodes of FEA) and integration points in the thickness direction of the models. For example, for the plate model, during IGA and FEA, the number of integration points through-thickness direction are respectively 2 and 4.

From the isogeometric optimization, it can be observed that firstly, thorough the change of control point position, an ideal and realistic door shape can be easily obtained, which is normally difficult with the design variables of element nodes; secondly, because of the combination of CAE and CAD models, after calculation, there is no need to post-processing steps to exchange data with the CAD systems.

In the future, it is necessary to consider the IGA in the following aspects: 1) complex geometrical modeling. As the tower flange is simplified in this work, next step, we will consider the IGA on a more realistic tower model; 2)

new basis function. We can observe some asymmetric and large area stress distribution from the analysis results on the plate model (like Fig. 3.5), which is mainly because of the less mesh density in critical areas. We will try to use the new basis functions such as T spline to support the local mesh refinement; 3) design optimization on the whole structure. In this studying, the shape optimization on the wind turbine tower model is developed only considering the control point position of the door shape. Next step, we will perform isogeometric shape optimization on the whole tower model under consideration of multi-objective and advanced optimization algorithms; 4) advance fatigue criteria. For the fatigue analysis, the Sine's or Crossland's fatigue criterion will be considered; 5) new material. In the future, we will consider IGA on new materials, especially on 3d printing materials.

Appendix A

IGA Formulation in vibration

Let's consider a body and the global Cartesian reference system $\mathbf{x} = (x, y, z)^T$ and its associated orthonormal basis $\mathbf{e} = (e_1, e_2, e_3)^T$. The body is subjected to the volume forces $\mathbf{f} = f_i \mathbf{e}_i$ and traction vector acting on the body surface $\mathbf{t} = t_i \mathbf{e}_i$. The domain of the body Ω is bounded by prescribed displacement Γ_u and traction Γ_t boundaries. We can introduce the displacement field as $\mathbf{u} = u_i \mathbf{e}_i$ and the stress $\boldsymbol{\sigma} = \sigma_{ij} \mathbf{e}_i \otimes \mathbf{e}_j$ ($i, j = 1 \dots 3$) satisfying the equation in strong form:

$$\nabla \boldsymbol{\sigma} + \mathbf{f} = \rho \frac{\partial^2 \mathbf{u}}{\partial t^2} \quad \text{in } \Omega \quad (\text{A.1})$$

$$\boldsymbol{\sigma} \cdot \mathbf{n} = \mathbf{t} \quad \text{in } \Gamma_t \quad (\text{A.2})$$

where ∇ represents the divergence operator, ρ is the density assumed constant and \mathbf{n} is the outward normal vector. $\frac{\partial^2 \mathbf{u}}{\partial t^2} = \ddot{\mathbf{u}}$ is the acceleration vector of the body. This term stands for the inertial effect, which is considered negligible for a static problem.

The displacement field is approximated using NURBS basis functions to construct the CAD geometry of the structure. The discretization of the domain Ω into a number of sub-domains $\Omega^e = [\xi_i, \xi_{i+1}] \otimes [\lambda_j, \lambda_{j+1}]$ is carried out by using the B-spline and NURBS formulations described in Section 2.1, which transform the parametric coordinates to physical coordinates. A mapping is introduced to perform the analysis on each control point cp of any element e :

$$\mathbf{x}^e(\boldsymbol{\eta}) = \sum_{cp=1}^{n_{cp}^e} R_{cp}^e(\boldsymbol{\eta}) \mathbf{P}_{cp}^e \quad (\text{A.3})$$

where $\boldsymbol{\eta}$ contains the parametric coordinates given by ξ in one dimension and (ξ, λ) in two dimensions. n_{cp}^e is the number of control points over element e . Using the Galerkin method, the displacement and virtual displacement fields

can be deduced as follows:

$$\mathbf{u}^e(\mathbf{x}) = \sum_{cp=1}^{n_{cp}^e} R_{cp}^e(\boldsymbol{\eta}) \mathbf{u}_{cp}^e \quad (\text{A.4})$$

$$\delta \mathbf{u}^e(\mathbf{x}) = \sum_{cp=1}^{n_{cp}^e} R_{cp}^e(\boldsymbol{\eta}) \delta \mathbf{u}_{cp}^e \quad (\text{A.5})$$

where \mathbf{u}_{cp} and $\delta \mathbf{u}_{cp}$ correspond to the values of the displacement and virtual displacement fields at the control point \mathbf{P}_{cp} . The momentum equation of Eq.(A.1) can be used in a weak form based on the virtual work principle which can be built for each element e to obtain the governing dynamic equilibrium of motion for a structure:

$$\mathbf{M}^e \ddot{\mathbf{u}}^e + \mathbf{C}^e \dot{\mathbf{u}}^e + \mathbf{K}^e \mathbf{u}^e = \mathbf{F}^e \quad (\text{A.6})$$

\mathbf{u}^e is the control point displacement and \mathbf{F}^e is external force vector that represents the contribution of the total body forces. \mathbf{M}^e , \mathbf{C}^e and \mathbf{K}^e are, respectively, the isogeometric element mass, damping using the damping property of an element e denoted by κ , and stiffness matrices given by:

$$\mathbf{M}^e = \int_{\Omega} \rho \mathbf{R}^{eT} \mathbf{R}^e d\Omega^e \quad (\text{A.7})$$

$$\mathbf{C}^e = \int_{\Omega} \kappa \mathbf{R}^{eT} \mathbf{R}^e d\Omega^e \quad (\text{A.8})$$

$$\mathbf{K}^e = \int_{\Omega^e} \mathbf{B}^{eT} \mathbb{C} \mathbf{B}^e d\Omega^e \quad (\text{A.9})$$

where $\mathbb{C} = \mathbb{C}_{ijkl} \mathbf{e}_i \otimes \mathbf{e}_j \otimes \mathbf{e}_k \otimes \mathbf{e}_l$ and $\boldsymbol{\varepsilon} = \varepsilon_{ij} \mathbf{e}_i \otimes \mathbf{e}_j$ are, respectively, the fourth order material elastic and the strain tensors. The components of strain tensor can also be formulated from displacement as follows:

$$\varepsilon_{ij} = \frac{1}{2} [u_{i,j} + u_{j,i}] \quad (\text{A.10})$$

\mathbf{R} is the matrix of NURBS basis function and \mathbf{B} is the strain displacement matrix. It can be obtained by computing the derivatives of the basis functions $R_{cp}(\boldsymbol{\eta})$ for any element e . In bidimensional problem, the matrix has the following form:

$$\mathbf{B} = \begin{bmatrix} R_{1,x} & 0 & \dots & R_{i,x} & 0 & \dots & R_{n_{cp},x} & 0 \\ 0 & R_{1,y} & \dots & 0 & R_{i,y} & \dots & 0 & R_{n_{cp},y} \\ R_{1,y} & R_{1,x} & \dots & R_{i,y} & R_{i,x} & \dots & R_{n_{cp},y} & R_{n_{cp},x} \end{bmatrix} \quad (\text{A.11})$$

The global matrices can be assembled by their corresponding elemental matrices as follows:

$$\mathbf{M} = \sum_{e=1}^{n^e} \mathbf{M}^e, \quad \mathbf{C} = \sum_{e=1}^{n^e} \mathbf{C}^e, \quad \mathbf{K} = \sum_{e=1}^{n^e} \mathbf{K}^e \quad \text{and} \quad \mathbf{F} = \sum_{e=1}^{n^e} \mathbf{F}^e \quad (\text{A.12})$$

The equations for 3D static calculations are given by Agrawal and Gautam [49].

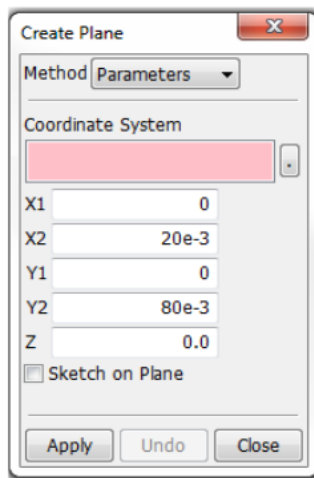
Appendix B

IGA in Ls Dyna

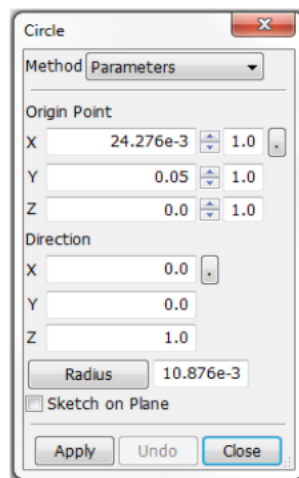
In this part, I will present the isogeometric static and dynamic analysis processes in Ls Dyna.

- I) Geometric model construction

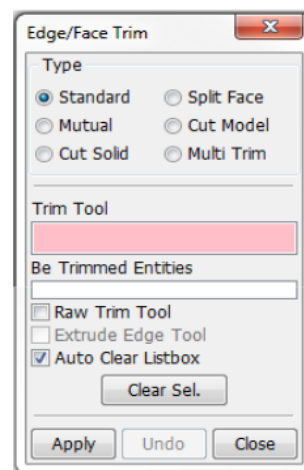
Using the keywords, PLANE and CIRCLE (Fig. B.1 (a) and (b)), a plate and two circles with the length, width and radius of 0.08, 0.02 and 0.010876 (m) can be constructed, as shown in Fig. B.1 (d). Then, based on the keyword, TRIMMING (Fig. B.1 (c)), the final plate model can be obtained, as the model in Fig. B.1 (e).



(a) Plate construction



(b) Circle construction



(c) Geometry trimming

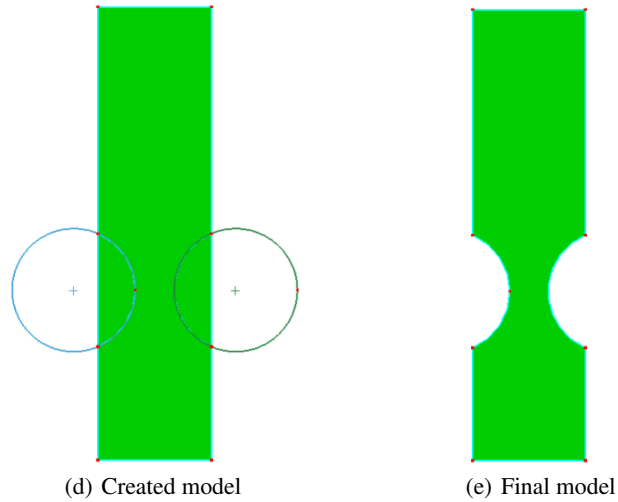


Figure B.1: The geometry construction

- II) Mesh model creation

Using the keyword, NURBS EDITOR, in the first step, the rough NURBS model can be created, which consists of 9 control points, and polynomial order of univariate NURBS basis functions in x and y -directions are 2 (Fig. B.2 (a)). In the second step, using the keyword, REFINE and SUBDIVIDE Fig. B.2 (b), the rough mesh model obtained from the first step is refined, in which the segment is equal to the NURBS element, and in $r(x)$ and $s(y)$ -direction, the segment numbers are respectively set 5 and 20. The final mesh model is shown in Fig. B.2 (c), it's comprised of 154 control points in this case, and polynomial order of NURBS basis functions in both directions are respectively 2. The detail information related to the mesh model can be observed from the Fig. B.3, for example, it can be seen that the number of control points in $r(x)$ and $s(y)$ are 7 and 22, corresponding polynomial orders are 2, and the knot vector in r direction is $\{0, 0, 0, 0.2, 0.4, 0.6, 0.8, 1, 1, 1\}$.

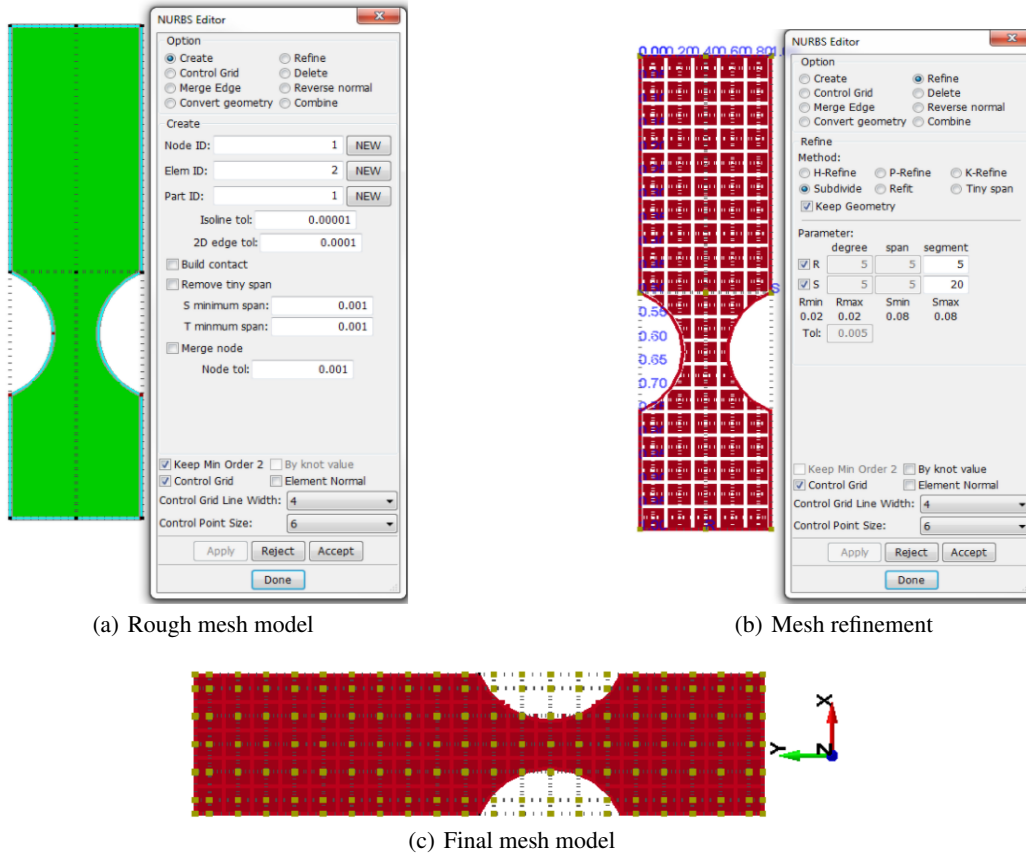


Figure B.2: The mesh model construction

- III) Material, section properties and boundary condition

The elastic material properties can be defined, based on the keywords, Material_Elastic (Fig. B.4 (a)), in which the Young's modulus, Poisson's ratio, and Mass density can be added. The section properties can be developed in the keyword, SECTION_SHELL (Fig. B.4 (b)), in which the element formulation, the number of integration points through thickness direction, the shell thickness can be defined. Based on the keyword, BOUNDARY_SPC (Fig. B.4 (c)), the boundary condition can be created on control points, in which each control point has 6 degree of freedoms that are respectively in translational and rotational constraints in local x, y, z directions.

*ELEMENT_SHELL_NURBS_PATCH_TRIMMED_(TITLE) (1)

TITLE

NPID PID NPR PR NPS PS PERIR PERIS

4 1 7 2 22 2 0 0

WFL FORM INT NISR NISS IMASS IDFNE

0 0 0 0 0 0 0 0

Repeated Data by Button and List

| RK1 | RK2 | RK3 | RK4 | RK5 | RK6 | RK7 | RK8 |
|-----|-----|-----|-----------|-----------|-----------|-----------|-----|
| 0.0 | 0.0 | 0.0 | 0.2010417 | 0.4020833 | 0.6020833 | 0.8020833 | 1.0 |

1 0.0 0.0 0.0 0.2010417 0.4020833 0.6020833 0.8020833 1.0

2 1.0 1.0 0.0 0.0 0.0 0.0 0.0 0.0

Data Pt. 1

Replace Insert

Delete Help

Repeated Data by Button and List

| SK1 | SK2 | SK3 | SK4 | SK5 | SK6 | SK7 | SK8 |
|-----|-----|-----|------|-----|-----------|-----------|-----------|
| 0.0 | 0.0 | 0.0 | 0.05 | 0.1 | 0.1501701 | 0.2003401 | 0.2503401 |

1 0.0 0.0 0.0 0.05 0.1 0.1501701 0.2003401 0.2503401

2 0.3003401 0.3505102 0.4006803 0.4508503 0.5008503 0.5508503 0.6008503 0.6508503

3 0.7010204 0.7511905 0.8011905 0.8511904 0.9011905 0.9513605 1.0 1.0

Data Pt. 1

Replace Insert

Figure B.3: Element shell NURBS patch

- IV) Static analysis

During isogeometric static analysis, a load can be applied directly on control points, and also on NURBS elements. The two cases would be explained in the following respectively.

- 1) case 1: load applied on control points

In the first step, the control points that would be carried on loads can be selected by the keyword, SET DATE SET_NODE(Fig. B.5 (a)). In the second step, the applied load value can be defined using the keyword, DEFINE_CURVE, in which the first column *A1* and second column *O1* respectively represent the time and load amplitude(Fig. B.5 (b)). In the final step, the defined load can be applied on the selected control points though the keyword, LOAD (Fig. B.5 (c)), in which the load can be applied in different directions through the selection of Degree of Freedom (DOF).

- 2) case 2: load applied on NURBS elements

A load can also be applied on NURBS elements, using the keyword, Load NURBS-SHELL (Fig. B.6), in which the NURBS element that would receive loads can be selected using the different knot values of the knot vectors, based

TITLE

| MID | RO | E | PR | DA | DB | NOT USED |
|-----|-----------|-----------|-----------|-----|-----|----------|
| 1 | 7850.0000 | 1.700e+11 | 0.3000000 | 0.0 | 0.0 | 0.0 |

(a) Material properties

TITLE

| SECID | ELFORM | SHRF | NIP | PROPT | QR/IRID | ICOMP | SETYP |
|-------|--------|------|------|-------|---------|-------|--------|
| | 2 | 1.0 | 2 | 1 | 0 | 0 | 1 |
| T1 | T2 | T3 | T4 | NLOC | MAREA | IDOF | EDGSET |
| 0.05 | 0.05 | 0.05 | 0.05 | 0.0 | 0.0 | 0.0 | 0 |

(b) Section properties

- [-] Airbag
 - ShellRefGM
- [+] Application
- [-] Boundary
 - Spc**
 - Prescribed Motion(BPM)
 - Spc Symmetry Plane
- [+] Constrained
- [+] Contact
- [+] Damping
- [+] Database
- [+] Define
- [+] Element
- [+] Initial
- [+] Integration
- [+] Load
- [+] Rigidwall
- [+] Section
- [+] Set Data

Show
 Cre
 Mod
 Del

Label:

Set
 Node

Cylindrical CS

Sym plane

| | | | | | |
|-------------------------------------|-------------------------------------|-------------------------------------|-------------------------------------|-------------------------------------|-------------------------------------|
| X | Y | Z | RX | RY | RZ |
| <input checked="" type="checkbox"/> | <input checked="" type="checkbox"/> | <input checked="" type="checkbox"/> | <input checked="" type="checkbox"/> | <input checked="" type="checkbox"/> | <input checked="" type="checkbox"/> |

Birth

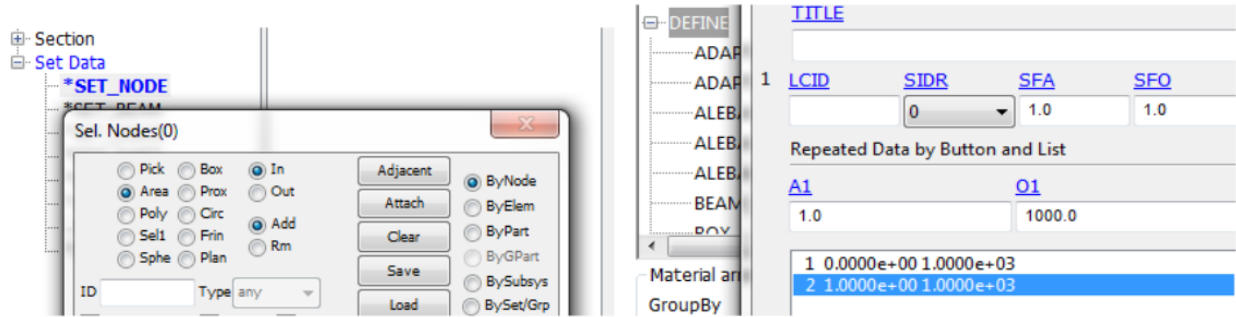
Death

CID

NSID

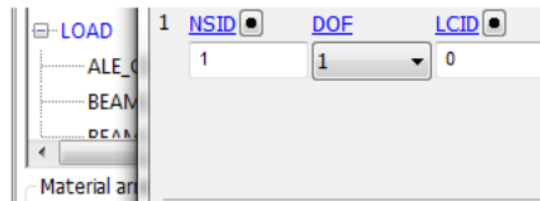
(c) Boundary condition

Figure B.4: Material, section properties and boundary condition setting



(a) Material properties

(b) Section properties



(c) Boundary condition

Figure B.5: The setting procedures of load application on control points

on the element shell NURBS patch information (Fig. B.3). The applied load type can be set based on the keyword, LTYPE, and the definition of applied load though the setting of the curve is the same as previous part.

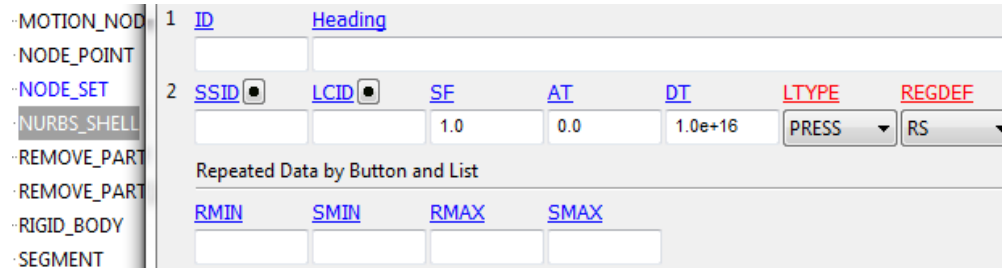


Figure B.6: load applied on NURBS elements

- V) Dynamic analysis

The setting process in modal analysis and fatigue analysis will be presented.

1) Modal analysis

In the first step, the number of eigenvalues to extract can be set, based on the keyword, IMPLICIT_EIGENVALUE (Fig. B.7 (a)), which would be used to activate eigenvalue analysis to compute eigen modes, which would be saved in a binary database "d3eigv"; the analysis method can be selected, using the keyword IMPLICIT_GENERAL(Fig. B.7 (b)), in which the time step for implicit analysis can also be defined; the analysis solution for implicit analysis can be chosen by the keyword, IMPLICIT_SOLUTION, (Fig. B.7 (c)).

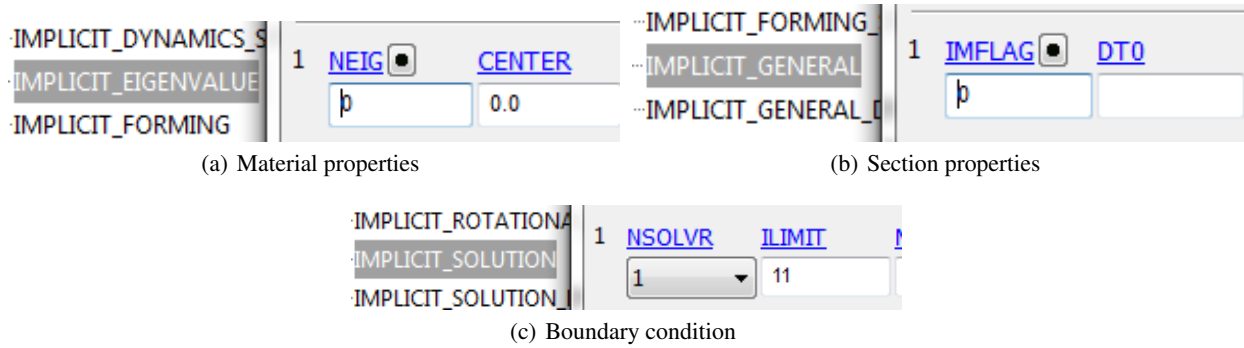


Figure B.7: Modal analysis procedures

2) Random vibration fatigue analysis

The definition of random vibration fatigue analysis in Ls Dyna can be broadly divided into two main steps. In the first step, using the keyword, FREQUENCY_DOMAIN RANDOM VIBRATION FATIGUE (Fig. B.8 (a)), some parameters which are related to random vibration fatigue analysis, including damping ratio, the excitation load type and exposure time, method for modal response analysis and random fatigue analysis can be respectively defined, also the S-N and excitation load curve, which are defined before by the keyword, DEFINE_CURVE, can be respectively selected based on the keywords, LDPSD and LCID (Fig. B.8 (b)). In the second step, the post-processing keywords such as FREQUENCY_BINARY D3FTG, D3PSD, D3RMS can be defined, and the minimum, maximum response frequencies, and the output PSD number can be defined in the keyword, FREQUENCY_BINARY D3PSD, (Fig. B.8 (c)).

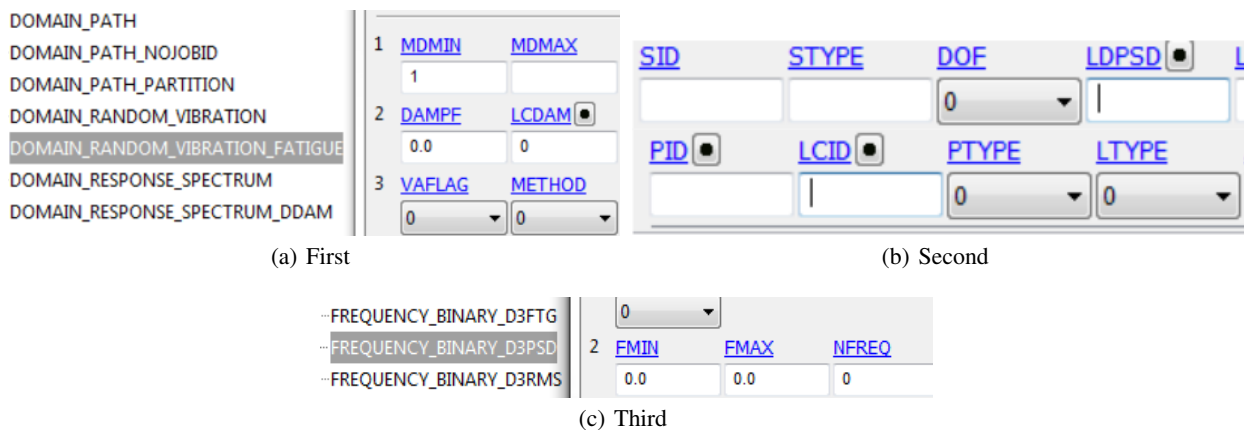


Figure B.8: Fatigue analysis procedures

Appendix C

Wind load calculation

The wind load applied in this work is calculated based on the reference [99]. A wind turbine is subjected to various loads from different sources such as aerodynamic loads. These loads depend on the environment of wind turbine systems. Indeed, there are many different climatic regions depending on the geography (mountain/plains, land/sea, type of vegetation) leading to a large variability of climatic conditions. The cyclic part of the load caused by wind shear is important to consider because it can lead to fatigue damage. The wind velocity depends on the time and the position of the calculation point. In the Cartesian space with parallel to the wind direction, the wind velocity $V_{ent}(t, P)$ at the time t , point P decomposed by the longitudinal component $\vec{U}(t)$, the lateral component $\vec{v}(t)$ and the vertical component $\vec{w}(t)$ is given by the equation following:

$$V_{ent}(t, P) = \vec{U}(t) + \vec{v}(t) + \vec{w}(t) = \begin{vmatrix} \bar{U} \\ 0 \\ 0 \end{vmatrix} + \begin{vmatrix} u(t) \\ v(t) \\ w(t) \end{vmatrix} \quad (\text{C.1})$$

Where \bar{U} is the longitudinal mean velocity which can be calculated, using the Eq. (C.2) or (C.3) for a height z denoted by $\bar{U}(z)$, and the corresponding wind-induced force $F(z)$ can be calculated with the method of static equivalent, as shown in Eq. (C.4).

Mean velocity $\bar{U}(z)$ is extrapolated (in the hypothesis of atmosphere neutral stability) from measurements at lower heights to a height z according to following logarithmic law:

$$\frac{\bar{U}(z)}{\bar{U}(z_r)} = \frac{\ln(\frac{z}{z_0})}{\ln(\frac{z_r}{z_0})} \quad (\text{C.2})$$

where z_0 is the roughness parameter (here $z_0 = 0.05$ m), $\bar{U}(z_r)$ is the average longitudinal wind speed at the reference height above the ground, normally given as $z_r = 10$ m. The following power law can also be used after identification of α :

$$\frac{\bar{U}(z)}{\bar{U}(z_r)} = \left(\frac{z}{z_r}\right)^\alpha \quad (\text{C.3})$$

Where α is the power exponent depending on the surface roughness.

Based on the Eq. (C.2), the wind velocity at different height can be obtained, as shown in Fig. C.1, in which the reference speed value is set to $\bar{U}(z_r) = 24$ m/s based on the region in Normandy, France.

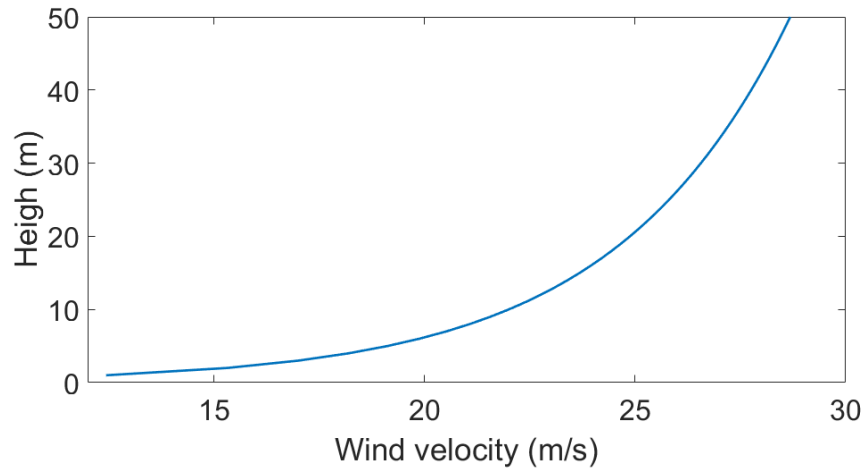


Figure C.1: Wind velocity against the height in Normandy region

The wind-induced average load $F(z)$ is given by:

$$F(z) = \frac{1}{2} \rho C_d S \bar{U}(z)^2 \quad (\text{C.4})$$

Where ρ is the air density, C_d is the coefficient of the wind resistance, S is the cross-sectional area of a structure perpendicular to the wind direction.

$u(t)$, $v(t)$ and $w(t)$ are considered as zero-mean Gaussian stationary processes. These processes are characterized by their standard deviations σ_u , σ_v and σ_w , as shown in the equations following. And the effects of wind turbulence $\{u(t), v(t), w(t)\}^T$ are described by the corresponding wind speed PSD $S_v(f)$ and wind force PSD $S_F(f)$.

$$\sigma_u = k_r \cdot \bar{U}(z_r) \cdot k_1 \quad (\text{C.5})$$

$$\sigma_v = 0.8\sigma_u \quad (\text{C.6})$$

$$\sigma_w = 0.5\sigma_u \quad (\text{C.7})$$

Where k_1 is the turbulence coefficient defined by the Eq. (C.9), k_r is the field factor, determined by the Eq. (C.8).

$$K_r = 0.19\left(\frac{z_0}{z_{0,11}}\right)^{0.07} \quad (\text{C.8})$$

$$k_1 = 1 - 2.10^{-4}(\log_{10}(z_0) + 3)^6 \quad (\text{C.9})$$

The turbulent intensities are given by $I_u(z) = \frac{\sigma_u}{\bar{U}(z)}$, $I_v(z) = \frac{\sigma_v}{\bar{U}(z)}$ and $I_w(z) = \frac{\sigma_w}{\bar{U}(z)}$. The turbulence scales L_c^r with $c = u, v, w$ and $r = x, y, z$ represent the average dimension of the natural wind gusts, which are obtained from the cross-correlation functions between two distinct points of the structure. The index of each symbol indicates the turbulent speed component considered. And the exponents indicate the axis measuring the distance between two points. For Eurocode 1, for heights z less than 200 m, the expression is shown as:

$$L_u^x = 300\left(\frac{z_r}{200}\right)^\beta \quad (\text{C.10})$$

where $\beta = 0.67 + 0.05\ln(z_0)$. Approximation of these parameters are often used such as $L_u^y = 0.3L_u^x$, $L_u^z = 0.5L_u^x$.

Under the assumption of isotropic turbulence, the following Eq. can be given:

$$L_v^x = 0.5 \cdot 0.8^3 \cdot L_u^x \quad (\text{C.11})$$

$$L_v^y = 2 \cdot 0.8^3 \cdot L_u^y \quad (\text{C.12})$$

$$L_v^z = 0.8^3 \cdot L_u^z \quad (\text{C.13})$$

$$L_w^x = 0.5^4 \cdot L_u^x \quad (\text{C.14})$$

$$L_w^y = 0.5^3 \cdot L_u^y \quad (\text{C.15})$$

$$L_w^z = 2 \cdot 0.5^3 \cdot L_u^z \quad (\text{C.16})$$

The longitudinal component of the wind is often decomposed into 3 zones. The low frequencies related to a large anisotropic vortex and leading to the energy generation. The mean frequencies leading to the energy transferred to small vortices. The high frequencies where the turbulent kinetic energy gets converted into heat by viscous dissipation due to viscous shear stresses.

The power spectral density (PSD) represents the energy distribution of the turbulence in different frequency ranges. Numerous studies adopt the Kaimal spectrum or Von Karman spectrum recommended in various standards. The normalized wind PSDs $\frac{f S_u(n)}{\sigma_u^2}$ are expressed by the normalized frequency which can simulate wind with or without turbulence. The wind applied in this work is considered with turbulence, the normalized frequency given by $\frac{f L_u^x}{\bar{U}(z)}$ include the turbulence scales.

For $0.007 \text{ Hz} \leq f \leq 1 \text{ Hz}$, the unilateral von Karman's PSD of the longitudinal velocity is given by:

$$S_u(f) = \frac{4 \frac{L_u^x}{\bar{U}(z_r)} \sigma_u^2}{(1 + 70.8 (\frac{f L_u^x}{\bar{U}(z_r)})^2)^{5/6}} \quad (\text{C.17})$$

For the mean and high frequencies, the following Kaimal PSD is used:

$$S_u(f) = \frac{4 \frac{L_{u,k}^x}{\bar{U}(z_r)} \sigma_u^2}{(1 + 6 (\frac{f L_{u,k}^x}{\bar{U}(z_r)})^2)^{5/3}} \quad (\text{C.18})$$

With $L_{u,k}^x = 2.329 L_u^x$.

For the Davenport:

$$S_u(f) = \frac{2/3 \frac{L_{u,d}^x}{\bar{U}(z_r)} \sigma_u^2}{(1 + (\frac{f L_{u,d}^x}{\bar{U}(z_r)})^2)^{4/3}} \quad (\text{C.19})$$

Where $L_{u,d}^x = 1200$.

For the Eurocode 1:

$$S_u(f) = \frac{6.8 \frac{L_u^x}{\bar{U}(z_r)} \sigma_u^2}{(1 + 10.2 (\frac{f L_u^x}{\bar{U}(z_r)})^2)^{5/3}} \quad (\text{C.20})$$

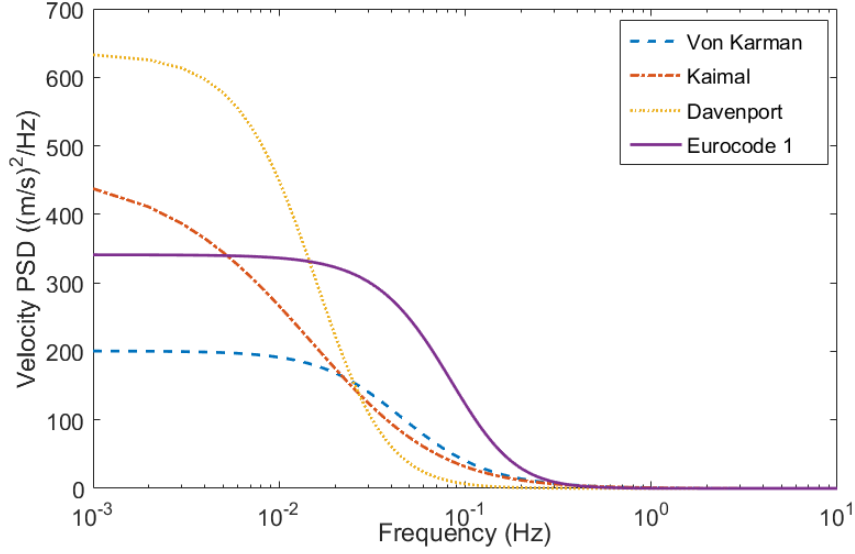


Figure C.2: The wind speed PSDs

Under the consideration of normalization, the normalized unilateral PSD of Von Karmen, Kaimel, Davenport and Eurocode 1, $\frac{fS_u(f)}{\overline{U}(z_r)^2}$ can be respectively given by:

For the Von Karmen:

$$\frac{fS_u(f)}{\overline{U}(z_r)^2} = \frac{4L_u^x \sigma_u^2 f}{\overline{U}(z_r)^3 (1 + 70.8 (\frac{fL_u^x}{\overline{U}(z_r)})^2)^{5/6}} \quad (C.21)$$

For the Kaimal:

$$\frac{fS_u(f)}{\overline{U}(z_r)^2} = \frac{4L_{u,k}^x \sigma_u^2 f}{\overline{U}(z_r)^3 (1 + 6 (\frac{fL_{u,k}^x}{\overline{U}(z_r)})^2)^{5/3}} \quad (C.22)$$

For the Davenport:

$$\frac{fS_u(f)}{\overline{U}(z_r)^2} = \frac{2/3 L_{u,d}^x \sigma_u^2 f}{\overline{U}(z_r)^3 (1 + (\frac{fL_{u,d}^x}{\overline{U}(z_r)})^2)^{4/3}} \quad (C.23)$$

For the Eurocode 1:

$$\frac{fS_u(f)}{\overline{U}(z_r)^2} = \frac{6.8 L_u^x \sigma_u^2 f}{\overline{U}(z_r)^3 (1 + 10.2 (\frac{fL_u^x}{\overline{U}(z_r)})^2)^{5/3}} \quad (C.24)$$

Based on the equations above, the normalized wind velocity PSD in x direction can be obtained, as shown in the Fig. C.3.

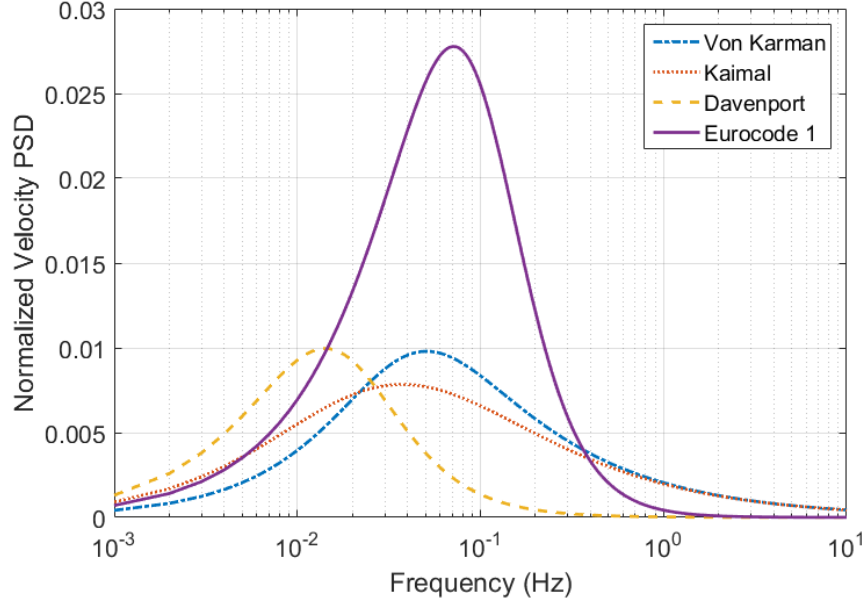


Figure C.3: The normalized wind speed PSDs

The wind-induced turbulent force $f(t, z)$ can be given as:

$$f(t, z) \approx \rho C_d S \bar{U}(z) u(t) \quad (C.25)$$

where C_d is the dynamic coefficient.

The PSD of the wind-induced turbulent force at a point P can be described by:

$$S_F(P, f) = (\rho C_d S)^2 \bar{U}(z)^2 S_u(P, f) \quad (C.26)$$

Where $S_u(P, f)$ is the wind speed PSD at the point P .

Meanwhile, the normalized wind force PSD $\frac{f S_F(P, f)}{\bar{U}(z_r)^2}$ can be given as:

$$\frac{f S_F(P, f)}{\bar{U}(z_r)^2} = \frac{(\rho C_d S)^2 \bar{U}(z)^2 S_u(P, f) f}{\bar{U}(z_r)^2} \quad (C.27)$$

Based on the different wind speed PSDs mentioned above, the corresponding turbulent force PSDs and normalized PSDs of longitudinal wind velocity can be obtained, as shown in Fig. C.4, in which the air density $\rho = 1.225 \text{ Kg/m}^3$, dynamic coefficient $C_d = 1.5$, surface area of the tower model $S = 95 \text{ m}^2$. The normalized wind force PSDs describes a fair image of the energy contained in the area of every frequency. It can be observed that the normalized force PSD of Eurocode 1 is most significant, compared with other counterparts. Thus, in this studying, we applied Eurocode 1 longitudinal, lateral and vertical force PSDs in x, y, z directions as respectively shown in the Fig. C.5, on the top of the tower model to develop random vibration fatigue analysis. From the Fig. C.5 (a), (b), (c), it can be seen that the

longitudinal, lateral and vertical force PSDs in z -directions are much more smaller than the ones of x and y directions, and thus they are displayed separately in Fig. C.5 (d).

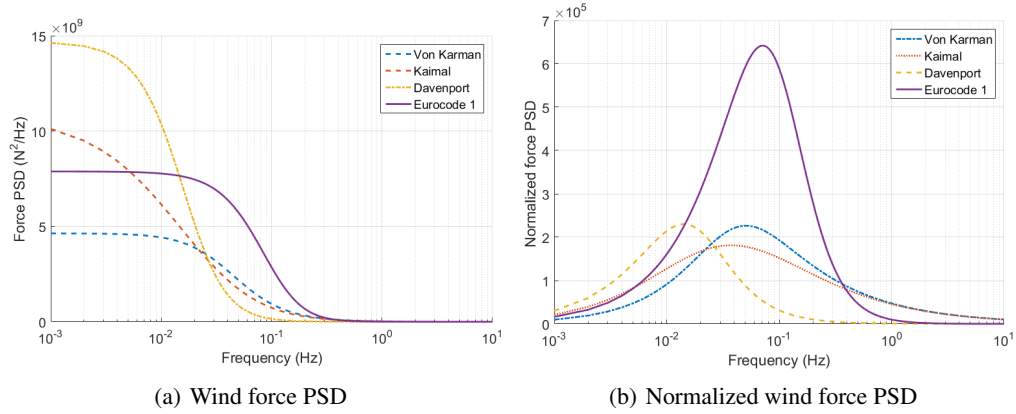


Figure C.4: The force PSD

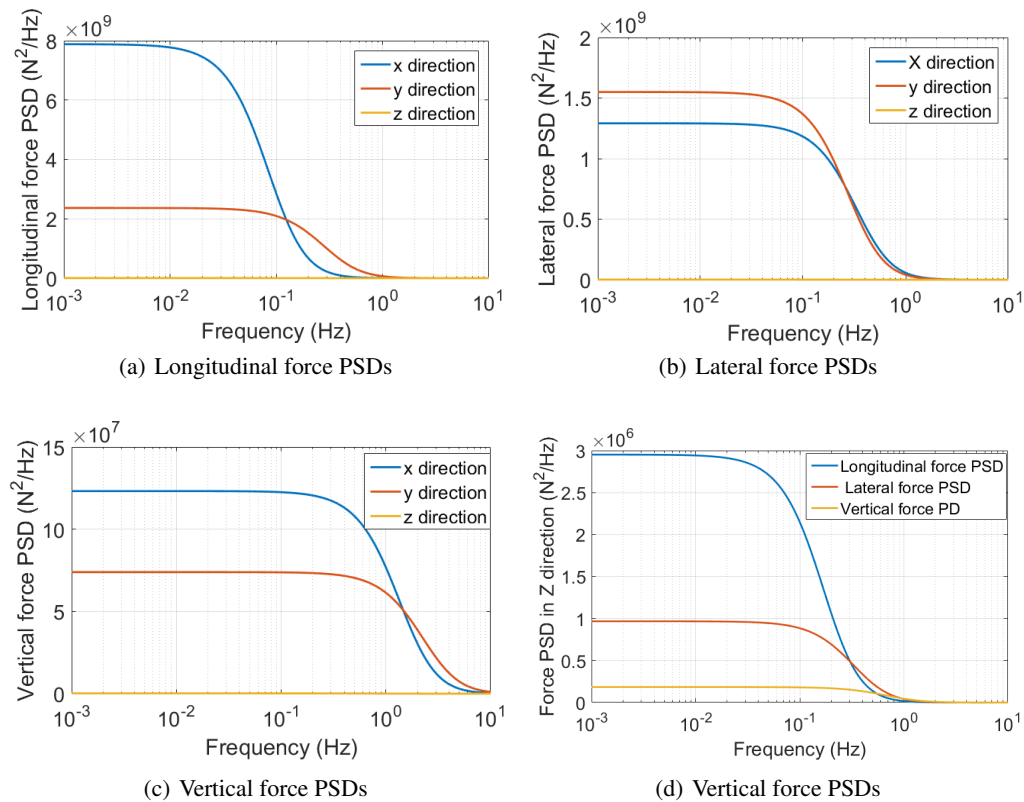


Figure C.5: Eurocode 1 force PSDs

Appendix D

General analysis procedure

- I) The overall analysis procedure

As the density of mesh elements in IGA and FEA has significant effects on analysis results, it is necessary to develop convergence analysis to obtain a more idealistic mesh model to compare the results from IGA and FEA. As shown in Fig. D.1, in the first step, the static and dynamic convergence analysis was developed to obtain isogeometric and finite element convergence points with the criteria of maximum stress or first natural frequency; In the second step; based on the previous convergence analysis, the mesh model would be chosen, and the damage would be calculated; In the third step, the fatigue results are validated with the ones from the experimental test or Matlab Programming.

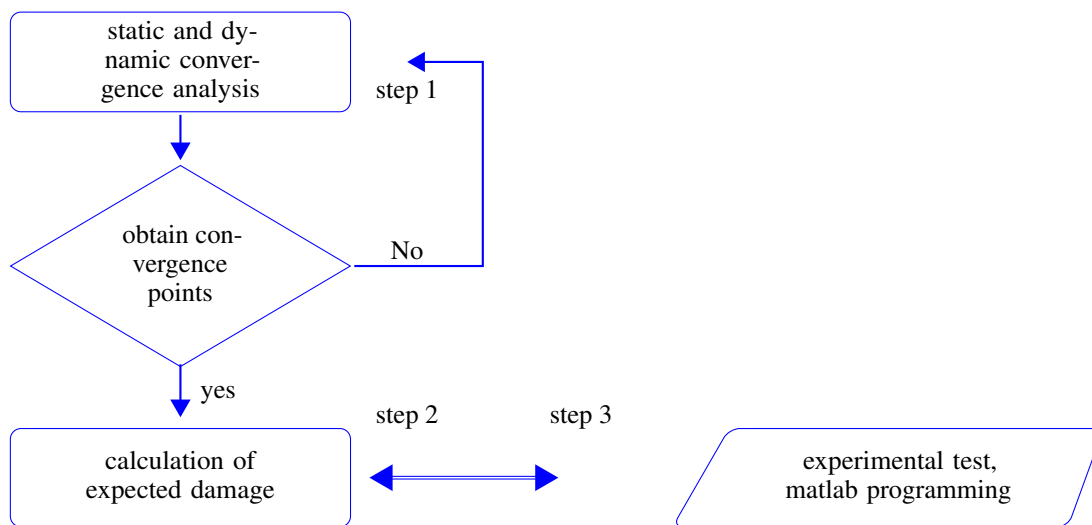


Figure D.1: Schematic illustration of the overall analysis procedures

- II) The fatigue analysis procedure

As shown in Fig. D.2, in the first step, the fatigue analysis is developed in Ls Dyna with the method of IGA and FEA, from which the cumulative damage ratio can be calculated, and also Power Spectrum density (PSD) can be obtained; In the second step, based on obtained cumulative damage ratio, the isogeometric and finite element fatigue life can be computed, respectively. In the third step, based on obtained PSD, the cumulative damage ratio can be calculated in Matlab to verify the damage results from Ls Dyna.

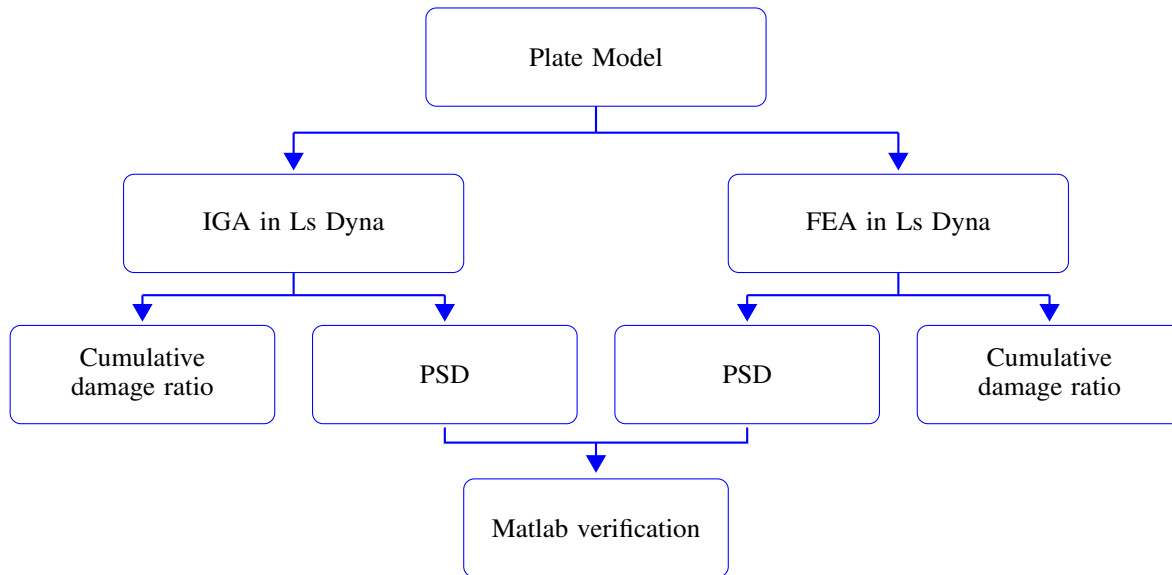


Figure D.2: Schematic illustration of the fatigue analysis procedure

Bibliography

- [1] A. Ringeval and Y. Huang, “Random vibration fatigue analysis with ls dyna,” 2012.
- [2] S. J. Owen, B. W. Clark, D. J. Melander, M. Brewer, J. F. Shepherd, K. Merkley, C. Ernst, and R. Morris, “An immersive topology environment for meshing,” in *Proceedings of the 16th International Meshing Roundtable* (M. L. Brewer and D. Marcum, eds.), (Berlin, Heidelberg), pp. 553–577, Springer Berlin Heidelberg, 2008.
- [3] T. Hughes, J. Cottrell, and Y. Bazilevs, “Isogeometric analysis: Cad, finite elements, nurbs, exact geometry and mesh refinement,” *Computer Methods in Applied Mechanics and Engineering*, vol. 194, no. 39, pp. 4135–4195, 2005.
- [4] X. Pitoiset and A. Preumont, “Tools for a multiaxial fatigue analysis of structures submitted to random vibrations,” 01 1998.
- [5] X. Pitoiset and A. Preumont, “Spectral methods for multiaxial random fatigue analysis of metallic structures,” *International Journal of Fatigue*, vol. 22, pp. 541–550, 2000.
- [6] N. E. Dowling, “Mean stress effects in stress-life and strain-life fatigue,” 2004.
- [7] S.-I. Moon, I.-J. Cho, and D. Yoon, “Fatigue life evaluation of mechanical components using vibration fatigue analysis technique,” *Journal of Mechanical Science and Technology*, vol. 25, pp. 631–637, 03 2011.
- [8] D. Sarkar, A. Khan, and R. Ahmar, “Random vibration analysis and fatigue life evaluation of auxiliary heater bracket,” 07 2011.
- [9] A. Niesłony and M. Böhm, “Mean stress value in spectral method for the determination of fatigue life,” *Acta Mechanica et Automatica*, vol. 6, pp. 71–74, 2012.
- [10] A. Essam and E. Hisham, “Nvh and random vibration fatigue analysis of a landing gear ’ s leg for an unmanned aerial vehicle using ls-dyna ®,” 2013.
- [11] Y. Eldoğan and E. Cigeroglu, “Vibration fatigue analysis of a cantilever beam using different fatigue theories,” pp. 471–478, 06 2014.
- [12] G. Teixeira, “Random vibration fatigue analysis of a notched aluminum beam,” *Int. J. Mech. Eng. Autom.*, vol. 2, pp. 425–441, 10 2015.

- [13] Y. Huang and Z. Cui, “Recent updates in fatigue analysis with ls-dyna,” 2018.
- [14] G. I. Demirel and A. Kayran, “Implementation of dirlik’s damage model for the vibration fatigue analysis,” *Procedia Structural Integrity*, 2019.
- [15] M. Böhm and K. Głowacka, “Fatigue life estimation with mean stress effect compensation for lightweight structures—the case of glare 2 composite,” *Polymers*, vol. 12, 2020.
- [16] T. W. Sederberg, J. Zheng, A. Bakenov, and A. H. Nasri, “T-splines and t-nurccs,” *ACM SIGGRAPH 2003 Papers*, 2003.
- [17] Y. Bazilevs, V. M. Calo, J. A. Cottrell, J. A. Evans, T. J. R. Hughes, S. Lipton, M. A. Scott, and T. W. Sederberg, “Isogeometric analysis using t-splines,” *Computer Methods in Applied Mechanics and Engineering*, vol. 199, pp. 229–263, 2010.
- [18] S. Hartmann, D. J. Benson, and D. Lorenz, “About isogeometric analysis and the new nurbs-based finite elements in ls-dyna,”
- [19] X. Qian, “Full analytical sensitivities in nurbs based isogeometric shape optimization,” *Computer Methods in Applied Mechanics and Engineering*, vol. 199, pp. 2059–2071, 2010.
- [20] Q. Yao and J. Yao, “Vibration fatigue in engineering structures,” vol. 23, pp. 12–15, 03 2006.
- [21] S. H. CRANDALL and W. D. MARK, “1 - characterization of random vibration,” in *Random Vibration in Mechanical Systems (Second Edition)* (S. H. CRANDALL and W. D. MARK, eds.), pp. 1–54, Academic Press, second edition ed., 1963.
- [22] Z. Azhou and Y. Qihang, *Vibration Environment Engineering*. Beijing: Aviation Industry Press, 1986.
- [23] Q. Yao and J. Yao, “The characteristics and analysis methods of structural vibration fatigue problems,” *Journal of Mechanical Science and Technology*, vol. 19, pp. 56–58, 2000.
- [24] Q. Yao and J. Yao, “Simplified analysis of structural random vibration response,” *Chinese Journal of Applied Mechanics*, vol. 19, pp. 103–105, 2002.
- [25] Q. Yao and J. Yao, “Structural vibration fatigue problems and airplane vibration assessment,” *Chinese Journal of Applied Mechanics*, pp. 16–20, 2000.
- [26] J. Schijve, “Four lectures on fatigue crack growth,” *Engineering Fracture Mechanics*, vol. 11, pp. 169–181, 1979.
- [27] M. Miner, “Cumulative damage in fatigue,” *Journal of Applied Mechanics*, vol. 12, pp. 159–164, 1945.
- [28] A. Palmgren, “Die lebensdauer von kugellagern (life length of roller bearings or durability of ball bearings),” *Zeitschrift des Vereines Deutscher Ingenieure (ZVDI)*, vol. 14, pp. 339–341, 1924.
- [29] B. Krasnowski, *Application of damage tolerance to increase safety of helicopters in service*. Defense technical information Center, 1999.

- [30] A. Strauss, D. M. Frangopol, and K. Bergmeister, "Life-cycle and sustainability of civil infrastructure systems," in *Proceedings of the Third International Symposium on Life-Cycle Civil Engineering* (A. Strauss, D. M. Frangopol, and K. Bergmeister, eds.), (Vienna, Austria, October 3-6, 2012), CRC press, 2012.
- [31] G. Risitano, D. Corallo, D. Corallo, and A. Risitano, "Cumulative damage by miner's rule and by energetic analysis," *Structural Durability Health Monitoring*, vol. 8, pp. 91–109, 2012.
- [32] Y.-L. Lee and D. Taylor, "Cycle counting techniques," in *Fatigue Testing and Analysis* (Y.-L. Lee, J. Pan, R. B. Hathaway, and M. E. Barkey, eds.), vol. 3, pp. 77–102, Burlington: Butterworth-Heinemann, 2005.
- [33] I. Milne, R. O. Ritchie, and B. L. Karihaloo, "Cyclic loading and fatigue," in *Comprehensive Structural Integrity: Cyclic loading and fatigue*, vol. 4, Elsevier, 2003.
- [34] M. Matsuichi and T. Endo, "Fatigue of metals subjected to varying stress," 1968.
- [35] J. O. Smith, "The effect of range of stress on the fatigue strength of metals," 1942.
- [36] E. Al-Bahkali, H. Elkenani, and Y. Soulie, "Fatigue life estimate of landing gear's leg using modal analysis," *The International Journal of Multiphysics*, vol. 8, pp. 231–244, 06 2014.
- [37] T. Dirlik, "Application of computers in fatigue analysis," 1985.
- [38] H. Ding, "Wideband audio over narrowband low-resolution media," in *2004 IEEE International Conference on Acoustics, Speech, and Signal Processing*, vol. 1, pp. I–489, 2004.
- [39] J. S. Bendat, "Probability functions for random responses: Prediction of peaks, fatigue damage, and catastrophic failures," 1964.
- [40] P. H. Wirsching and M. C. Light, "Fatigue under wide band random stresses," *Journal of the Structural Division*, vol. 106, pp. 1593–1607, 1980.
- [41] J. M. Tunna, "Fatigue life prediction for gaussian random loads at the design stage," *Fatigue & Fracture of Engineering Materials & Structures*, vol. 9, pp. 169–184, 1986.
- [42] J. C. P. Kam and W. D. Dover, "Fast fatigue assessment procedure for offshore structures under random stress history," 1988.
- [43] G. Chaudhury and W. D. Dover, "Fatigue analysis of offshore platforms subject to sea wave loadings," *International Journal of Fatigue*, vol. 7, pp. 13–19, 1985.
- [44] D. S. Steinberg, "Vibration analysis for electronic equipment," 1973.
- [45] A. Merigaud and J. Ringwood, "Free-surface time-series generation for wave energy applications," *IEEE Journal of Oceanic Engineering*, vol. PP, pp. 1–17, 04 2017.
- [46] B.-R. You and S.-B. Lee, "A critical review on multiaxial fatigue assessments of metals," *International Journal of Fatigue*, vol. 18, no. 4, pp. 235–244, 1996.

- [47] J. wung Choi, R. E. Curry, and G. H. Elkaim, "Path planning based on bézier curve for autonomous ground vehicles," *Advances in Electrical and Electronics Engineering - IAENG Special Edition of the World Congress on Engineering and Computer Science 2008*, pp. 158–166, 2008.
- [48] M. Elhoseny, A. Tharwat, and A. E. Hassanien, "Bezier curve based path planning in a dynamic field using modified genetic algorithm," *J. Comput. Sci.*, vol. 25, pp. 339–350, 2018.
- [49] V. Agrawal and S. S. Gautam, "Iga: A simplified introduction and implementation details for finite element users," *Journal of The Institution of Engineers (India): Series C*, vol. 100, pp. 561–585, 2019.
- [50] A. Buffa, G. Sangalli, and R. Vázquez, "Isogeometric analysis in electromagnetics: B-splines approximation," *Computer Methods in Applied Mechanics and Engineering*, vol. 199, pp. 1143–1152, 2010.
- [51] M. R. Dörfel, B. Jüttler, and B. Simeon, "Adaptive isogeometric analysis by local h-refinement with t-splines," *Computer Methods in Applied Mechanics and Engineering*, vol. 199, pp. 264–275, 2010.
- [52] W. Wang, Y. J. Zhang, M. A. Scott, and T. J. R. Hughes, "Converting an unstructured quadrilateral mesh to a standard t-spline surface," *Computational Mechanics*, vol. 48, pp. 477–498, 2011.
- [53] N. Nguyen-Thanh, H. Nguyen-Xuan, S. P. A. Bordas, and T. Rabczuk, "Isogeometric analysis using polynomial splines over hierarchical t-meshes for two-dimensional elastic solids," *Computer Methods in Applied Mechanics and Engineering*, vol. 200, pp. 1892–1908, 2011.
- [54] M. Campen and D. Zorin, "Similarity maps and field-guided t-splines: a perfect couple," *ACM Transactions on Graphics*, vol. 36, pp. 1–16, 07 2017.
- [55] N. El-Abbasi, S. A. Meguid, and A. Czekanski, "On the modelling of smooth contact surfaces using cubic splines," *International Journal for Numerical Methods in Engineering*, vol. 50, pp. 953–967, 2001.
- [56] G. Jianli, Y. Guolai, and L. Jia, "Advances in isogeometric analysis," *Advances in Mechanics*, vol. 42, pp. 771–784, 2012.
- [57] J. Lu, "Isogeometric contact analysis: Geometric basis and formulation for frictionless contact," *Computer Methods in Applied Mechanics and Engineering*, vol. 200, pp. 726–741, 2011.
- [58] İlker Temizer, P. Wriggers, and T. J. R. Hughes, "Contact treatment in isogeometric analysis with nurbs," *Computer Methods in Applied Mechanics and Engineering*, vol. 200, pp. 1100–1112, 2011.
- [59] İlker Temizer, P. Wriggers, and T. J. R. Hughes, "Three-dimensional mortar-based frictional contact treatment in isogeometric analysis with nurbs," *Computer Methods in Applied Mechanics and Engineering*, vol. 209, pp. 115–128, 2012.
- [60] Y. Bazilevs and T. J. R. Hughes, "Nurbs-based isogeometric analysis for the computation of flows about rotating components," *Computational Mechanics*, vol. 43, pp. 143–150, 2008.
- [61] Y. Bazilevs, V. M. Calo, Y. Zhang, and T. J. R. Hughes, "Isogeometric fluid–structure interaction analysis with applications to arterial blood flow," *Computational Mechanics*, vol. 38, pp. 310–322, 2006.

- [62] Y. Bazilevs, V. M. Calo, T. J. R. Hughes, and Y. J. Zhang, “Isogeometric fluid-structure interaction: theory, algorithms, and computations,” *Computational Mechanics*, vol. 43, pp. 3–37, 2008.
- [63] B. Hassani, S. M. Tavakkoli, and N. Z. Moghadam, “Application of isogeometric analysis in structural shape optimization,” *Scientia Iranica*, vol. 18, pp. 846–852, 2011.
- [64] S. Shojaee, N. Valizadeh, and M. Arjomand, “Isogeometric structural shape optimization using particle swarm algorithm,” *Iran University of Science & Technology*, vol. 1, pp. 633–645, 2011.
- [65] W. A. Wall, M. A. Frenzel, and C. J. Cyron, “Isogeometric structural shape optimization,” *Computer Methods in Applied Mechanics and Engineering*, vol. 197, pp. 2976–2988, 2008.
- [66] S. Cho and S.-H. Ha, “Isogeometric shape design optimization: exact geometry and enhanced sensitivity,” *Structural and Multidisciplinary Optimization*, vol. 38, pp. 53–70, 2008.
- [67] H. S. H, “Isogeometric shape design optimization using nurbs basis functions,” 2010.
- [68] S.-H. Ha, K. K. Choi, and S. Cho, “Numerical method for shape optimization using t-spline based isogeometric method,” *Structural and Multidisciplinary Optimization*, vol. 42, pp. 417–428, 2010.
- [69] A. P. Nagy, M. Abdalla, and Z. Gürdal, “Isogeometric sizing and shape optimisation of beam structures,” *Computer Methods in Applied Mechanics and Engineering*, vol. 199, pp. 1216–1230, 2010.
- [70] A. P. Nagy, M. Abdalla, and Z. Gürdal, “Isogeometric design of elastic arches for maximum fundamental frequency,” *Structural and Multidisciplinary Optimization*, vol. 43, pp. 135–149, 2011.
- [71] Y.-D. Seo, H.-J. Kim, and S.-K. Youn, “Shape optimization and its extension to topological design based on isogeometric analysis,” *International Journal of Solids and Structures*, vol. 47, pp. 1618–1640, 2010.
- [72] Y.-D. Seo, H.-J. Kim, and S.-K. Youn, “Isogeometric topology optimization using trimmed spline surfaces,” *Computer Methods in Applied Mechanics and Engineering*, vol. 199, pp. 3270–3296, 2010.
- [73] N. D. Manh, A. Evgrafov, A. R. Gersborg, and J. Gravesen, “Isogeometric shape optimization of vibrating membranes,” *Computer Methods in Applied Mechanics and Engineering*, vol. 200, pp. 1343–1353, 2010.
- [74] X. Qian, “Full analytical sensitivities in nurbs based isogeometric shape optimization,” *Computer Methods in Applied Mechanics and Engineering*, vol. 199, pp. 2059–2071, 2010.
- [75] J. Kiendl, K.-U. Bletzinger, J. Linhard, and R. Wüchner, “Isogeometric shell analysis with kirchhoff–love elements,” *Computer Methods in Applied Mechanics and Engineering*, vol. 198, pp. 3902–3914, 2009.
- [76] D. J. Benson, Y. Bazilevs, M.-C. Hsu, and T. J. R. Hughes, “Isogeometric shell analysis: The reissner-mindlin shell,” *Computer Methods in Applied Mechanics and Engineering*, vol. 199, pp. 276–289, 2010.
- [77] D. J. Benson, Y. Bazilevs, M.-C. Hsu, and T. J. R. Hughes, “A large deformation, rotation-free, isogeometric shell,” *Computer Methods in Applied Mechanics and Engineering*, vol. 200, pp. 1367–1378, 2011.
- [78] T.-K. Uhm and S.-K. Youn, “T-spline finite element method for the analysis of shell structures,” *International Journal for Numerical Methods in Engineering*, vol. 80, pp. 507–536, 2009.

- [79] J. Kiendl, Y. Bazilevs, M.-C. Hsu, R. Wüchner, and K.-U. Bletzinger, “The bending strip method for isogeometric analysis of kirchhoff–love shell structures comprised of multiple patches,” *Computer Methods in Applied Mechanics and Engineering*, vol. 199, pp. 2403–2416, 2010.
- [80] X. Peng, E. Atroshchenko, P. Kerfriden, and S. P. A. Bordas, “Isogeometric boundary element methods for three dimensional static fracture and fatigue crack growth,” *Computer Methods in Applied Mechanics and Engineering*, vol. 316, pp. 151–185, 2017.
- [81] J. A. Cottrell, A. Reali, Y. Bazilevs, and T. J. R. Hughes, “Isogeometric analysis of structural vibrations,” *Computer Methods in Applied Mechanics and Engineering*, vol. 195, pp. 5257–5296, 2006.
- [82] X. Zhang, Y. Xia, Q. Hu, and P. Hu, “Efficient isogeometric formulation for vibration analysis of complex spatial beam structures,” *European Journal of Mechanics A-solids*, vol. 66, pp. 212–231, 2017.
- [83] D. Wang, W. Liu, and H. Zhang, “Novel higher order mass matrices for isogeometric structural vibration analysis,” *Computer Methods in Applied Mechanics and Engineering*, vol. 260, pp. 92–108, 2013.
- [84] S. Shojaei, E. Izadpanah, N. Valizadeh, and J. Kiendl, “Free vibration analysis of thin plates by using a nurbs-based isogeometric approach,” *Finite Elements in Analysis and Design*, vol. 61, pp. 23–34, 2012.
- [85] S. Gondegaon and H. K. Voruganti, “Static structural and modal analysis using isogeometric analysis,” *Journal of Theoretical and Applied Mechanics*, vol. 46, pp. 36 – 75, 2016.
- [86] T. D. Hien and H.-C. Noh, “Stochastic isogeometric analysis of free vibration of functionally graded plates considering material randomness,” *Computer Methods in Applied Mechanics and Engineering*, vol. 318, pp. 845–863, 2017.
- [87] S. L. A., “Structural design by systematic synthesis,” *In: Proceedings of the second ASCE conference on electronic computation*, pp. 105–122, 1960.
- [88] V. Braibant and C. Fleury, “Shape optimal design using b-splines,” *Computer Methods in Applied Mechanics and Engineering*, vol. 44, pp. 247–267, 1984.
- [89] A. Jamshid, “A survey of shape parameterization techniques,” 1999.
- [90] O. C. Zienkiewicz, R. L. Taylor, and J. Z. Zhu, “The finite element method: Its basis and fundamentals,” 2005.
- [91] P. Milić and D. Marinković, “Isogeometric structural analysis based on nurbs shape functions,” vol. 11, pp. 193 – 202, 2014.
- [92] G. Kirsch, “Die theorie der elastizität und die bedürfnisse der festigkeitslehre,” *Zentralblatt Verlin Deutscher Ingenieure*, vol. 42, 1898.
- [93] A. Appert, C. Gautrelet, L. Khalij, and R. Troian, “Development of a test bench for vibratory fatigue experiments of a cantilever beam with an electrodynamic shaker,” vol. 165, 2018.
- [94] L. Khalij, C. Gautrelet, and A. Guillet, “Fatigue curves of a low carbon steel obtained from vibration experiments with an electrodynamic shaker,” *Materials & Design*, vol. 86, pp. 640–648, 2015.

- [95] W. Xu, Y. Xianfeng, B. Zhong, H. Yuhuai, and C. hu Tao, "Failure criterion of titanium alloy irregular sheet specimens for vibration-based bending fatigue testing," *Engineering Fracture Mechanics*, vol. 195, pp. 44–56, 2018.
- [96] H. T. Hu, Y. Li, T. Suo, F. Zhao, Y. Miao, P. Xue, and Q. Deng, "Fatigue behavior of aluminum stiffened plate subjected to random vibration loading," *Transactions of Nonferrous Metals Society of China*, vol. 24, pp. 1331–1336, 2014.
- [97] N. Bazeos, G. Hatzigeorgiou, I. D. Hondros, H. E. Karamaneas, D. L. Karabalis, and D. E. Beskos, "Static, seismic and stability analyses of a prototype wind turbine steel tower," *Engineering Structures*, vol. 24, pp. 1015–1025, 2002.
- [98] A. V. Fiacco and G. P. McCormick, "Nonlinear programming: Sequential unconstrained minimization techniques," New York: John Wiley and Sons, 1968.
- [99] Nguyen and Quang-Huy, "Réponse des lignes de transport au vent turbulent par la méthode spectrale stochastique," 2006.